Phil. Trans. R. Soc. Lond. A **321**, 361–401 (1987) [361]
Printed in Great Britain

ON VOIDITES: A HIGH-RESOLUTION TRANSMISSION ELECTRON MICROSCOPIC STUDY OF FACETED VOID-LIKE DEFECTS IN NATURAL DIAMONDS

By J. C. BARRY[1, 2]†, L. A. BURSILL[1], J. L. HUTCHISON[2], A. R. LANG[3], F.R.S., G. M. RACKHAM[3]‡ and N. SUMIDA[3]§

[1] *School of Physics, University of Melbourne, Parkville, Victoria* 3052, *Australia*
[2] *Department of Metallurgy and Science of Materials, University of Oxford, Parks Road, Oxford OX*1 3*PH, U.K.*
[3] *H. H. Wills Physics Laboratory, University of Bristol, Tyndall Avenue, Bristol BS*8 1*TL, U.K.*

(*Received* 10 *January* 1986)

[Plates 1–14]

CONTENTS

		PAGE
1.	Introduction	363
2.	Experimental background: the platelets on {100}	364
	(*a*) X-ray diffraction evidence	364
	(*b*) Optical properties associated with platelets	365
	(*c*) Electron microscopic observations and platelet structure models	367
3.	Studies of voidites	368
	(*a*) Early observations, specimen selection and techniques	368
	(*b*) Voidites and partial platelets	373
	(*c*) Voidites and dislocations	376
	(*d*) Particular observations concerning voidite contrast and distributions	379
	(*e*) Edge-on images of voidite sheets	383
	(*f*) Summary of representative micrographs of voidite phenomena	385
4.	Discussion	386
	(*a*) The environment of voidites	386
	(*b*) The volumes of voidites	393
	(*c*) The formation of voidites	396
	References	401

† Present address: Center for Solid State Science, Arizona State University, Tempe, Arizona 85287, U.S.A.
‡ Present address: Sharveshill Farm, Little Testwood, Totton, Southampton SO4 2RW, U.K.
§ Present address: Department of Materials Science and Engineering, Faculty of Engineering, Osaka University, 2-1 Yamadaoka, Suita, Osaka 565, Japan.

In natural diamonds of optical classification type I a, nitrogen is the major identified impurity and is distributed mainly in point defects known as A defects (probably a pair of nitrogen atoms substituting for a pair of adjacent carbon atoms) and B defects (probably four substituted nitrogen atoms tetrahedrally surrounding a carbon vacancy), and also in the electron-microscopically visible platelet precipitates on {100}. This paper is concerned with other electron-microscopically detectable defects, discovered by R. F. Stephenson (Ph.D. thesis, University of Reading (1977)), that lie in {100} planes in circumstances strongly suggesting that they result from the decomposition of platelets. High-resolution electron microscopy shows these defects to be {111}-faceted cavities. They behave as pure phase-contrast objects whose interior density does not exceed about one-third that of the diamond matrix: we call them 'voidites'.

The experimental background to voidite observation is reviewed, including electron-microscopic measurements on normal {100} platelets and models of their structure, and the optical, X-ray diffraction and cathodoluminescence evidence for unusually large platelets whose presence, together with a relative richness in B defects, indicates an environment in which voidites are likely to be discovered.

Almost all observed voidites are confined to sheets strictly parallel to {100}. Some voidite sheets occur in 'partial platelets', where they replace part of the original area of normal platelet. Other voidite sheets occur within dislocation loops whose size and shape are similar to those of the peripheries of normal platelets in the specimen. Voidites occur in a wide range of sizes. The largest equiaxed voidites observed measure about 10 nm between opposite {111} facets, and the smallest resolved about 0.5 nm. Many voidites are elongated in one of the ⟨110⟩ directions in the plane of the voidite sheet: the most highly elongated voidites seen approach 100 nm in length, with diameters of a few nanometres. Variations in size, shape and number density of voidites, together with many other characteristics relevant to the microscopic processes of voidite formation, are discussed in detailed descriptions of about 40 voidite sheets occurring in partial platelets and dislocation loops in two diamond specimens. One specimen was free from both grown-in dislocations and dislocations associated with plastic deformation. It contained zones of highly elongated platelets and it appeared that transformation of a platelet into a voidite sheet surrounded by a dislocation loop was triggered by the mutual very close approach of platelets. The second voidite-containing specimen had suffered plastic deformation at some stage in its history, but did not exhibit direct evidence that glide dislocations had triggered the transformation. The Burgers vectors of 24 dislocation loops enclosing voidite sheets in the second specimen were determined. Twelve were of normal $\frac{1}{2}\langle 110\rangle$ type having a component $\frac{1}{2}a_0$ normal to the voidite sheet, and twelve were non-primitive, the Burgers vector being a_0 normal to the voidite sheet (a_0 is the diamond face-centred cubic (FCC) unit cell edge).

The volumes of over 2000 individual voidites, representing all or major parts of 12 voidite sheets, have been measured. Values found for the ratio $\sum V/Aa_0$ (where $\sum V$ is the aggregate voidite volume in a sheet area A) averaged about unity for 9 sheets of generally similar, voidite-rich appearance. Other sheets are poorer in voidites of measurable dimensions: the ratios for two such sheets averaged 0.25.

In the concluding analysis, a reaction involving A and B point defects is proposed for the production of platelets. Other reactions including voidites (but no dislocations) are suggested in which both platelet production and elimination might occur. For the dominating reaction, when a platelet is replaced by a voidite sheet surrounded by an interstitial dislocation loop, models are developed for the cases when the Burgers vector component perpendicular to the loop is either a_0 or $\frac{1}{2}a_0$, with the assumption that the platelet nitrogen is dispersed partly into B defects and partly into the voidites. The predicted values of $\sum V/Aa_0$ come out as about unity and as 0.25 (or lower) for the larger and smaller Burgers vectors, respectively.

1. Introduction

The majority of natural diamonds contain 'platelet' defects lying in the {100} planes of the diamond structure. The platelets are of oligo-atomic thickness. Their diameters fall most frequently in the range 10–100 nm: both size and number density vary widely from specimen to specimen, and very often show large zonal variations within specimens. Platelets are only found in diamonds in which nitrogen is the major identified impurity, and it is now accepted that the platelets contain nitrogen. But whereas negligible nitrogen content (less than a few parts per million) ensures that platelets are absent (or too few to be readily detected by transmission electron microscopy) there is no simple proportionality between nitrogen impurity content and the total platelet area per unit volume. Strong zonal variations of both total nitrogen content and the relative proportions of the several known states of aggregation of the nitrogen are a common occurrence in natural diamonds, and they bedevil studies of nitrogen impurity in diamond.

The first evidence for the presence of platelets on {100} planes in diamond came with the discovery of the 'spike' diffuse X-ray reflections exhibited by diamonds which absorbed ultraviolet radiation in the wavelength range 225 to *ca.* 330 nm (Raman & Nilakantan 1940), but some time elapsed before it was generally recognized that the only reasonable explanation of the 'spike' reflections was the presence of platelet defects on {100}. Evans & Phaal (1962) were the first to observe the platelets directly, by transmission electron microscopy. In the years following, until the middle 1970s, various ideas were floated concerning the structure and composition of platelets, but the fact of their existence was beyond question, and indeed there was no reason to doubt that platelets once formed at some stage in the history of the diamond remained unaltered within it thereafter, under natural conditions. Then, first at Reading and later at Bristol, new contrast-producing objects were discovered in transmission electron micrographs of diamonds. They lay in {100} planes in circumstances strongly suggesting that they resulted from the decomposition of platelets. We named these objects 'voidites', for reasons explained below. Within a few years after the first detection of voidites, the power of transmission electron microscopic methods applied to defects in diamonds had gained substantial enhancement, in part through improved control in specimen preparation but principally through access to high-voltage, high-resolution microscopes. The consequence has been paradoxical: with instrumentation at last adequate for precise measurements of size, shape and diffraction-contrast characteristics of those most firmly established of all microscopic defects in diamond, the platelets, it has been phenomena related to platelet disappearance that have yielded the most striking new observational material. The new area of experimental investigation opened up, concerned with reactions between platelets and dislocations, and with the decomposition of platelets, bids fair to embrace problems of greater complexity than those involved in the original formation of platelets in natural diamonds.

This paper presents an account of experiments on voidites carried out in Bristol and Oxford between 1977 and 1981, concentrating particularly on the high-resolution electron micrographs taken at Oxford in the last year of that period. The report begins with a summary of experimental evidence concerning 'normal' platelets and of the suggestions current regarding their structure. The principal section (§3) attempts to put on record all the characteristics of voidites that have been observed in our experiments: such a compilation of voidite properties contains the factual background against which theories of voidite formation can be judged.

The discussion, §4, contains statistics on voidite occurrences together with data on voidite sizes and volumes, and it concludes with some ideas concerning the processes of formation of platelets and voidites in diamonds under natural conditions.

2. Experimental background: the platelets on {100}

(*a*) *X-ray diffraction evidence*

The temperature-independent 'spike' diffuse X-ray reflections from platelet-containing diamonds correspond to spike-like, ⟨100⟩-oriented extensions of reflecting power from the diamond reciprocal-lattice points. Some of the properties of platelets first inferred from spike X-ray reflections can now be derived directly from electron micrographs, but spike reflections are important not only because they demonstrate that sheet-like defects parallel to {100} must be present within most natural diamonds, but also because they provide the clearest evidence that the platelets on {100} have a well-defined structure. The basis for the latter conclusion is the existence of a definite 'form factor' describing the intensity variation in reciprocal space of spikes oriented in a given cube direction at each reciprocal-lattice point. This was firmly established by the experiments of Hoerni & Wooster (1955), who showed that for the [001] spikes (due to platelets parallel to (001)) there was a nodal plane close to the *hk*3 reciprocal-lattice layer, and corresponding nodal planes for spikes parallel to [100] and [010]. In the 'spike topograph' method of Takagi & Lang (1964) scattered X-ray intensity is measured as a function of position in two spaces: in real space as a function of location of the scattering volume within the specimen crystal, and in reciprocal space as a function of position of the scattering vector relative to a reciprocal-lattice point of the perfect crystal. Combination of the real-space and reciprocal-space measurements provides, non-destructively, information on the concentration and average size of the platelets point-by-point within the specimen, the size estimates being derived from the sharpness of spike topograph images (Moore & Lang 1972, 1977).

The near-vanishing of spikes at the third order carries ambiguities in its interpretation (Frank 1964; Lang 1964; Takagi & Lang 1964). They are relevant also in electron microscopy and diffraction, so will now be summarized. There exists a relative displacement of the diamond matrix on either side of a platelet: this displacement, $\boldsymbol{u}_{\mathrm{m}}$, is definable by a Burgers circuit passing through the platelet, with positive $\boldsymbol{u}_{\mathrm{m}}$ signifying a parting of the matrix by the platelet. From the variation of spike intensity with order of reflection in the diamond diffraction pattern a certain minimum displacement $\boldsymbol{u}_{\mathrm{s}}$ may be derived. The spike intensity depends upon the value of $\sin^2 \pi \boldsymbol{g} \cdot \boldsymbol{u}_{\mathrm{s}}$, $\boldsymbol{g}$ being a diamond reciprocal-lattice vector (in magnitude g is the reciprocal of the interplanar spacing). For platelets parallel to (001), say, the nodal plane close to the *hk*3 reciprocal-lattice layer shows that $\boldsymbol{u}_{\mathrm{s}}$ is close to $\frac{1}{3}$ [**001**], the magnitude of [**001**] being 0.3567 nm, the edge length a_0 of the Bravais cell. The sign of $\boldsymbol{u}_{\mathrm{s}}$ is undetermined. The relation between $\boldsymbol{u}_{\mathrm{m}}$ and $\boldsymbol{u}_{\mathrm{s}}$ is $\boldsymbol{u}_{\mathrm{m}} = \boldsymbol{u}_{\mathrm{s}} + \boldsymbol{L}_1$, where $\boldsymbol{L}_1$ can be any lattice vector in the primitive diamond lattice. To derive a model of the platelet structure one needs to know $\boldsymbol{u}_{\mathrm{p}}$, the difference between the cell edge of the structure comprising a unit layer of platelet parallel to (001), say, and the corresponding edge vector [**001**] of a normal diamond cell. Since there may be perfect dislocations around the platelet periphery to minimize misfit with the matrix, $\boldsymbol{u}_{\mathrm{m}}$ and $\boldsymbol{u}_{\mathrm{p}}$ are related by $\boldsymbol{u}_{\mathrm{m}} = \boldsymbol{u}_{\mathrm{p}} + \boldsymbol{L}_2$, where $\boldsymbol{L}_2$ is the sum of the perfect dislocation Burgers vectors and is another lattice vector in the primitive diamond lattice. Thus we have the general relation

$$\boldsymbol{u}_{\mathrm{p}} = \boldsymbol{u}_{\mathrm{s}} + \boldsymbol{L}_1 - \boldsymbol{L}_2. \qquad (1)$$

From single spike-intensity measurements, neither L_1 nor L_2 is determinable. In addition to this general ambiguity, note also a special ambiguity arising from u_s/a_0 being close to $\frac{1}{3}$: low integral multiples of this fraction give either the same spike intensity at reciprocal lattice points or no spike at all.

Hoerni & Wooster's measurements were made on diamonds producing sharp spikes and hence containing relatively large platelets. It is not surprising to find that the more diffuse spike patterns given by small platelets (such as those with mean diameter *ca.* 15 nm, say) indicate a smaller u_s than in the case of larger platelets (Suzuki & Lang 1975). This does not imply that small platelets differ in structure from larger ones, but only that their surrounding matrix displacement fields are more poorly represented by a one-dimensional model of homogeneous lattice displacements produced by platelets of infinite lateral extent. At the other end of the size scale there can occasionally be found 'giant' platelets, which exceed 1 μm in at least one direction in the platelet plane. With platelet diameters of 1 μm or more, and interplatelet distances of *ca.* 5 μm or more, the X-ray diffraction contrast images of platelets can be individually resolved. At this size they can also be individually resolved by cathodoluminescence topography (see §2*b* below). Giant platelets are of interest in the context of this report because prospecting for them involved studies of platelets that were unusually large and sparsely distributed, and it was among these platelets that voidites were discovered.

X-ray diffraction provides information bearing on the states of aggregation of diamond other than that derivable from spike reflections. Kaiser & Bond (1959) showed that the lattice parameter of diamond increases linearly with its nitrogen content, but that the density of the diamond remains constant. Structures proposed for nitrogen aggregates in diamond (at least of the dominant species of aggregate) must not conflict with these findings.

(*b*) *Optical properties associated with platelets*

Platelet-containing diamonds belong to the optical classification type Ia, in which nitrogen impurity is present in non-paramagnetic aggregates (for reviews of the optical properties of diamonds, see Davies (1977) and Walker (1979)). The total nitrogen content, and its partitioning among several distinguishable states of aggregation, are assessed from the one-phonon infrared absorption bands in the 7–11 μm range. In type Ia diamonds, the most conspicuous nitrogen-dependent absorptions in this wavelength range are two overlapping features with complex profiles, the A feature with principal peak at 1282 cm^{-1}, 7.8 μm, and the B feature with principal peak at 1176 cm^{-1}, 8.5 μm. These are now ascribed respectively to the 'A-defect' and 'B-defect' types of nitrogen aggregate. A third absorption maximum, not overlapping the A and B features above mentioned, with a peak at about 1370 cm^{-1}, 7.3 μm, is now accepted as being due to platelets. The peak at 7.3 μm (usually called the B′ peak in English literature) is rather variable in width and shape. How, or indeed whether, these B′ peak characteristics depend upon size and shape of platelets is not yet known, nor has there yet been established a reliable factor to convert integrated absorption in the B′ peak into a figure for total platelet area per unit volume of specimens. Knowledge regarding the A absorption feature is better: there is an accepted conversion rule, expressible as

$$\mu_A(7.8)/\mathrm{mm}^{-1} = (30 \pm 2)\, N_A, \qquad (2)$$

which relates N_A, the atomic percentage nitrogen in the specimen aggregated in A defects, with μ_A, the absorption coefficient in units of mm^{-1} at 7.8 μm (Davies 1980). Considerable uncertainty attaches to a corresponding relation for assessing the amount of nitrogen in B defect

form from the strength of the B absorption feature measured at the same wavelength, 7.8 μm, and the situation has recently been complicated by the claim of Clark & Davey (1984) that another absorption feature overlapping the A and B components of the absorption profile may be present. The new feature, which they term the D component, occurs in association with the B component, tending to be strong when the B component is strong, but the relative concentration of B defects and of the D defects assumed responsible for the D component varies considerably. Clark & Davey assume that the D defect is an aggregated form of nitrogen different from the A, B and platelet forms, and on this basis propose equations analogous to (2).

$$\mu_{\mathrm{B}}(7.8)/\mathrm{mm}^{-1} = 12\,N_{\mathrm{B}} \tag{3a}$$

and

$$\mu_{\mathrm{D}}(7.8)/\mathrm{mm}^{-1} = 5\,N_{\mathrm{D}}, \tag{3b}$$

where $\mu_{\mathrm{B}}(7.8)$ and $\mu_{\mathrm{D}}(7.8)$ are the contributions (in units of mm^{-1}) to the total absorption at 7.8 μm, derived by decomposing the observed absorption profile into A, B and D components, and N_{B} and N_{D} are the numbers of nitrogen atoms (expressed as percentage of the total number of atoms in the crystal) that are aggregated into B defects and D defects, respectively. If, on the other hand, the absorption profile is decomposed into A and B components only, the conversion factor for B defects suggested as then applicable (Davies 1980) is

$$\mu_{\mathrm{B}}(7.8)/\mathrm{mm}^{-1} = 8.5\,N_{\mathrm{B}}. \tag{3c}$$

In connection with A and B defects it should be noted that of these two defects it is only A defects that produce strong absorption in the 225–330 nm range in the ultraviolet (Davies & Summersgill 1973), and it is this ultraviolet absorption that traditionally has been the criterion for separating type Ia diamonds from types IIa and IIb, which have negligible nitrogen content. This topic will be returned to in connection with specimen-selection procedure discussed below (§3*a*). Recent practice (but antedating the intrusion of D defects upon the scene) adopts the designation IaA and IaB to denote end members of the series of type Ia diamonds containing both A defects and B defects: thus type IaA denotes a diamond with an 'A only' infrared absorption spectrum, no B feature being detectable. Current notions concerning the structure of A and B defects will be considered in §4*c*.

There are two vibronic absorption and emission systems in the visible spectrum that are of interest in connection with presence of platelets unusually large, and of voidites. These are the H3 system, with zero-phonon line at 2.463 eV, 503 nm, and the H4 system with zero-phonon line at 2.498 eV, 496 nm. It is well established that in type Ia diamonds that have been electron irradiated and annealed at temperatures of 600–800 °C, the ratio of the strengths of the H3 and H4 systems equals, within experimental error, the ratio of A defect to B defect concentrations determined from infrared absorption (Davies 1972). In natural diamonds, not laboratory irradiated, the H3 and H4 systems may be observed together in cathodoluminescence from the α-radiation-damaged rinds of specimens (Hanley *et al.* 1977), and in such regions the H3:H4 ratio also probably correctly represents the A:B ratio. However, in non-irradiated diamond the observed H3:H4 ratio bears little resemblance to the A:B ratio (Collins 1982). This is particularly true in the case of the H3 emission from dislocation-rich slip planes recorded by cathodoluminescence (Hanley *et al.* 1977). No H4 emission accompanied this H3 emission, although it is likely that the B:A ratio in the diamond matrix was high. Diamond matrices sufficiently low in nitrogen content for H3-system dislocation cathodolumi-

nescence to be observed are also those in which there is the best chance of discovering visible cathodoluminescence from individual 'giant' platelets, i.e. platelets of area greater than 1 μm^2, optically individually resolvable. Hanley *et al.* (1977) advanced reasons for believing that the principal visible component of this platelet emission was also the H3 system, although the identification was qualified by the caveat that they had not succeeded in recording the H3 zero-phonon line in the platelet emission. Their investigation covered eight specimens that gave an H3-like emission from platelets. Subsequently, platelets have been encountered that produce a noticeably redder emission than that from sources of H3 emission in the same specimen. Possibly it was a specimen of this latter type whose visible platelet emission spectrum was recorded by Collins & Woods (1982) and was found to peak at longer wavelengths (about 580 nm) than the H3 vibronic band recorded at the same temperature (160 °C). Although uncertainty surrounds the nature of the optical centres producing platelet cathodoluminescence at visible wavelengths, the existence of this emission is a useful sensitive detector of giant platelets, and there is a high probability of finding unusually large platelets (i.e. exceeding several tenths of a micrometre in one dimension at least) in zones adjacent to those containing giants.

(*c*) *Electron microscopic observations and platelet structure models*

Transmission electron microscopic techniques provide information on both composition and structure of platelets. Electron energy-loss spectroscopy has shown that the platelets contain nitrogen (Berger & Pennycook 1982), but the platelet disruption that occurs during probing prevents reliable data on the number of nitrogen atoms per unit area of platelet being obtained. As regards structure, several of the quantities in (1) can be found. In the electron case, it is more appropriate to try to determine $\boldsymbol{u}_s$ from the variation with reflection order of the area contrast of individual platelet images, under two-beam diffraction conditions, than from spike diffuse reflection intensities in the electron diffraction pattern, although the latter are strong in platelet-rich diamonds (Sumida & Lang 1982). Analysis of the diffraction contrast due to the strain field of the matrix at the platelet periphery gives $\boldsymbol{u}_m$, and when lattice resolution is achieved $\boldsymbol{u}_p$ may be found directly. Major steps on the road towards finding $\boldsymbol{u}_s$, $\boldsymbol{u}_m$ and $\boldsymbol{u}_p$ have been as follows. James & Evans (1965) established that $\boldsymbol{u}_m$ was positive, a finding confirmed by all later work. Humble (1982) matched observed and computed images of both area contrast and peripheral contrast of platelets and concluded that $\boldsymbol{u}_s = \boldsymbol{u}_m$, the direction being normal to the platelet plane and magnitude equal to $0.4a_0$. Humble was handicapped by a specimen with very unsmooth surfaces, and we believe that the last part of his finding should be restated as 'the magnitude of $u_s = u_m$ lies between $0.35a_0$ and $0.4a_0$'. By using a more favourable specimen, Sumida & Lang (1987) have confirmed that $\boldsymbol{u}_s = \boldsymbol{u}_m$, that $\boldsymbol{u}_m$ is precisely normal to the platelet plane, and that the non-vanishing of area contrast in the third order shows that u_s must differ from $\frac{1}{3}a_0$ by at least several per cent. The most precise determination of the sign and magnitude of $\boldsymbol{u}_m$ to date comes from an overlap moiré pattern between platelet-containing and platelet-free thin foils, and gives $0.350 < u_m/a_0 < 0.362$ (Bursill *et al.* 1981). A direct determination of $\boldsymbol{u}_m$ has been achieved by measuring the positions of resolved lattice fringes in an edge-on view of a platelet and its surrounding matrix (Barry *et al.* 1983), and produced the value $u_m = (0.33 \pm 0.05)\, a_0$. Another, recent, determination of u_m from such measurements of resolved lattice fringes gave $u_m = (0.39 \pm 0.04)\, a_0$ (Humble *et al.* 1985*a*).

The platelet structure of Lang (1964) was proposed in the days when it was believed that most, if not substantially all, the nitrogen in type I*a* diamonds was precipitated in platelet form,

rather than being distributed among A defects, B defects and platelets (with A defects accounting for most of the nitrogen in the majority of type I a specimens) as is now the accepted view. Consequently, the structure model was designed to have a density equal to that of the diamond matrix, to agree with the constant-density finding of Kaiser & Bond (1959), as well as to make $u_s = \frac{1}{3}a_0$ to agree with Hoerni & Wooster (1955), with $u_s = u_m$ being positive to agree with James & Evans (1964), it being assumed that $L_1 = L_2 = 0$. The model is simply described. Consider a platelet parallel to (001). All carbon atoms at a particular height, say those with fractional coordinates $\frac{1}{4}, \frac{1}{4}, \frac{1}{4}$ and $\frac{3}{4}, \frac{3}{4}, \frac{1}{4}$ in a given (001) layer of face-centred cubic (FCC) cells of diamond structure, are replaced by a pair of nitrogen atoms singly bonded to each other with the N–N bond parallel to [001]. Thus a unit cell with the platelet structure contains six carbon and four nitrogen atoms compared with eight carbons in the normal diamond FCC cell, and u_p is expected to be exactly $\frac{1}{3}a_0$. A very different platelet model has been proposed by Humble (1982). It contains no nitrogen, but consists of an interstitial layer of carbon atoms pentagonally bonded, and would produce a value of u_p that could lie between $0.35\,a_0$ and $0.45\,a_0$. Humble's structure is very open: with his chosen value $u_p = 0.4\,a_0$ his platelet unit cell has only 0.8 times the density of normal diamond. Comparisons of experimentally resolved two-dimensional lattice images of edge-on views of platelets with computer simulations of images of various platelet models calculated for a range of specimen thickness and defocus conditions (Hutchison *et al.* 1982; Bursill 1983; Barry *et al.* 1984) offer no support for the 1982 Humble platelet model, but do give some support to a new model, the 'zig-zag' structure that the above authors propose. The 'zig-zag' and 'Lang' platelet structures are closely related. Whereas in the latter the sheet of carbons replaced by dinitrogens all lie at the same height in the structure (say on the β sublattice sites at fractional height $z = \frac{1}{4}$ in the normal diamond cell), alternate rows of α-site carbons ($z = 0$) and β-site carbons ($z = \frac{1}{4}$) are replaced by dinitrogens in the 'zig-zag' model. Thus, choosing sublattice rows parallel to [110], the coordinates of replaced carbon atoms in a pair of adjacent rows are (referred to the normal diamond cell) $\frac{1}{4}, \frac{1}{4}, \frac{1}{4} \pm \frac{1}{2}m\,[\mathbf{110}]$, and $1, 0, \pm\frac{1}{2}n\,[\mathbf{110}]$, m and n being 0 or integers. The [110] and [$\bar{1}$10] directions are not equivalent in the zig-zag platelet structure, whereas they are in the Lang platelet structure. However, the density and expected value of u_p are the same for both models. Recently Humble *et al.* (1985*b*) have proposed a nitrogen-containing platelet structure with half the nitrogen content of the Lang and 'zig-zag' models, giving a $1.40\,a_0$ platelet cell height and density 0.92 times that of normal diamond.

3. Studies of voidites

(*a*) *Early observations, specimen selection and techniques*

Voidites were discovered by Stephenson and Evans (Stephenson 1977; Evans 1978) in an electron microscopic study of a type I a B diamond that contained zones filled with a high density of dislocation loops. Objects with apparent diameters in the 5–10 nm range, referred to by these workers as 'dots' and 'precipitates', occurred strung along the loop dislocations and also within the interiors of the loops. The observations reported in the present paper commenced on a specimen that was relatively rich in B defects, as judged by fluorescence and cathodoluminescence, but that was also too inhomogeneous for meaningful assessment by infrared absorption measurements. It was one of the specimens selected for an investigation of giant platelets (Woods 1976). That investigation pursued the following strategy. Out of a few thousand diamonds,

36 were selected on the basis of birefringence indications of strong impurity zoning without a high dislocation density. Further selection by X-ray topography, and by cathodoluminescence topography after cutting and polishing, located intercalations of platelet-rich and platelet-poor zones and (in 6 out of the 36 diamonds) giant platelets. In the subsequent electron microscopy, a key feature was the preparation of specimen foils parallel to (110) instead of the (001) orientation conventionally employed before then. The (110) specimen orientation, also used throughout the present work, readily shows the sizes and shapes of platelets, and greatly facilitates distinction between platelets and dislocation loops (figure 1). As it turned out, a remarkable juxtaposition of platelets and loops of similar size and shape was found by Woods in the two specimens that he examined by electron microscopy. We now believe that Woods's loops contained voidites, probably in a smaller size range than the relatively large 'dots' seen by Stephenson. The smaller voidites are extremely hard to detect unless the specimen foil surfaces are free from ripples and other artefacts of the specimen-thinning process. Woods's specimens did not have smooth surfaces. Fortunately, another of his specimens (A4) was successfully thinned by one of the authors (G.M.R.) and its platelet population was subjected to close study in a Philips EM 400 electron microscope operating at 120 kV. Now, a further advantage of the (110) orientation of specimen foils is its perpendicular intersection with four out of the eight surfaces of the normal faceted octahedral growth habit. Variations of platelet size and concentration normal to growth surfaces over a distance scale as fine as one platelet diameter can be revealed with this specimen orientation. Such short-range variations were prominent in specimen A4. One zone a few micrometres wide that contained platelets larger and sparser than those in its surrounding regions attracted attention and was surveyed over

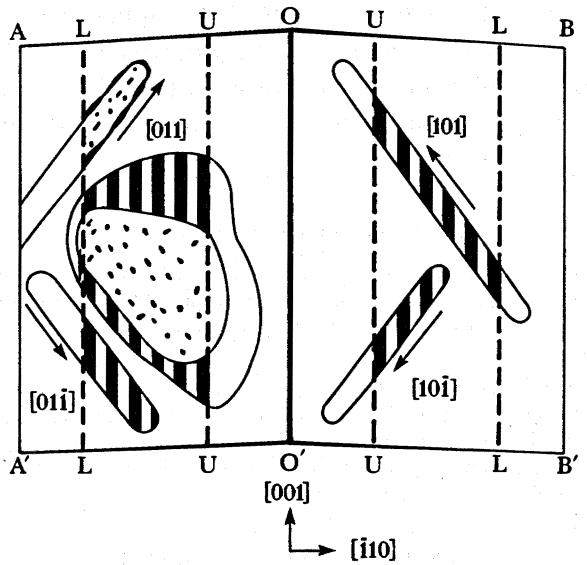

FIGURE 1. The appearance of defects lying on (100) and (010) in a specimen slice cut parallel to (110) with [110] pointing towards the observer. Heavy broken lines show traces of intersections of (100) and (010) by the upper (U) and lower (L) specimen surfaces, which also truncate the defects. The defects on the (100) plane, OAA′O′, are a voidite-filled dipole loop parallel to [011] truncated by L, an annular partial platelet truncated by both U and L, and a lath-like platelet elongated parallel to [01$\bar{1}$] and truncated by L. On the (010) plane, OBB′O′, can be seen a highly elongated platelet parallel to [101] cut by both U and L, and a platelet lath parallel to [10$\bar{1}$] cut by U. Note that the length of the projection on (001) of the image of the lath truncated by both U and L equals the specimen thickness. (Defects on (001) appear as lines parallel to [$\bar{1}$10], laths parallel to [110] appearing as short lines.)

a distance of many tens of micrometres parallel to an octahedral growth facet. The fields of figure 2, plate 1 and figure 4, plate 2 are located in this zone. Both platelets and dislocation loops lying in (100) and (010) can be seen. The concentration of loops in (100) and (010) in figures 2 and 4 is about one-tenth that of platelets on those planes. The majority of loops lie exactly in cube planes, within the accuracy of orientation determination, and have their long sides parallel to the ⟨110⟩ directions in these planes, just as do the lath-like platelets that they also resemble in width. Within all loops in figures 2 and 4 we can detect 'dots', and in some cases short 'streaks' parallel to one or both ⟨110⟩ directions in the loop plane. Every loop seen entire in figure 4 appears to be joined with another loop or platelet.

This electron microscopic survey also yielded the first clear images of the defects that we call 'partial platelets'. Indications of the existence of a defect of this type had been gleaned from Woods's electron microscopy of giant platelets with electrons of 1 MeV energy. He reported a defect of rare occurrence (only four were noted) that consisted of dislocation loops in cube planes that showed fringe contrast over parts of the loop area (Woods 1976). A further study of Woods's micrographs, involving about 300 large platelet and platelet-like defects in four fields, yielded a residue of 14 objects of uncertain nature of which one or two did appear to be defects showing fault-surface-type diffraction contrast from only parts of their area (Lang 1977). A partial platelet is prominent in figure 2. It is located at the position (0.67, 0.60). (In all the micrographs, the locations of particular features will be indicated by their fractional Cartesian coordinates in the field, with origin at the bottom left corner of the field and x-direction horizontal. The prints reproduce the view looking down on the fluorescent screen: [110] points towards the observer and the direction of the electron beam is $[\bar{1}\bar{1}0]$. The original micrograph identifying number and magnification are given in parentheses at the end of each figure legend.) Another partial platelet is at (0.60, 0.35) in figure 4, and is of the type we call 'annular'. The specimen thickness in figure 4 is 0.5 μm, which has led to some resolution loss, but has enabled this annular platelet to be captured entire. The partial platelet in figure 2 is also of annular type. Both partial platelets contain 'dots' and 'streaks' in that part of their

Description of plate 1

Figure 2. A zone in specimen A4 containing large platelets and voidite-containing dislocation loops. One annular partial platelet also appears. Specimen thickness in centre of field is 0.3 μm. Electron accelerating voltage 120 kV. In this figure and in figures 4 and 8, [001] points towards top of field and the field width is 4 μm (8071, original magnification × 10500).

Figure 3. Detail in the large voidite-containing loop at the centre of the field of figure 2. The image is rotated about 17° clockwise relative to figure 2 (magnification × 160000). (*a*) Enlargement from the low-magnification micrograph, figure 2. (*b*) High magnification and resolution, electron accelerating voltage 200 kV, close to optimum focus. Longest voidite image is about 3 × 80 nm in projection. (4709, original magnification × 10^5.) (*c*) As (*b*), but underfocused by about 1 μm (4716).

Description of plate 2

Figure 4. A field in the same zone of specimen A4 as that shown in figure 2, but in a region where specimen thickness is 0.5 μm. The longest dimension of the annular platelet at (0.60, 0.35) is 0.6 μm. The longest platelet lath entirely contained within the specimen is 0.83 μm long. Electron accelerating voltage 120 kV. Field width 4 μm (8045, original magnification × 10500).

Figure 5. Detail of the platelet combination seen at (0.67, 0.60) in figure 2. The local specimen thickness is 0.22 μm (magnification × 160000). (*a*) Enlargement from figure 2; (*b*) higher resolution, electron accelerating voltage 200 kV. Focus chosen to maximize visibility of voidites at depths that produce light contrast on print (4686, original magnification × 10^5).

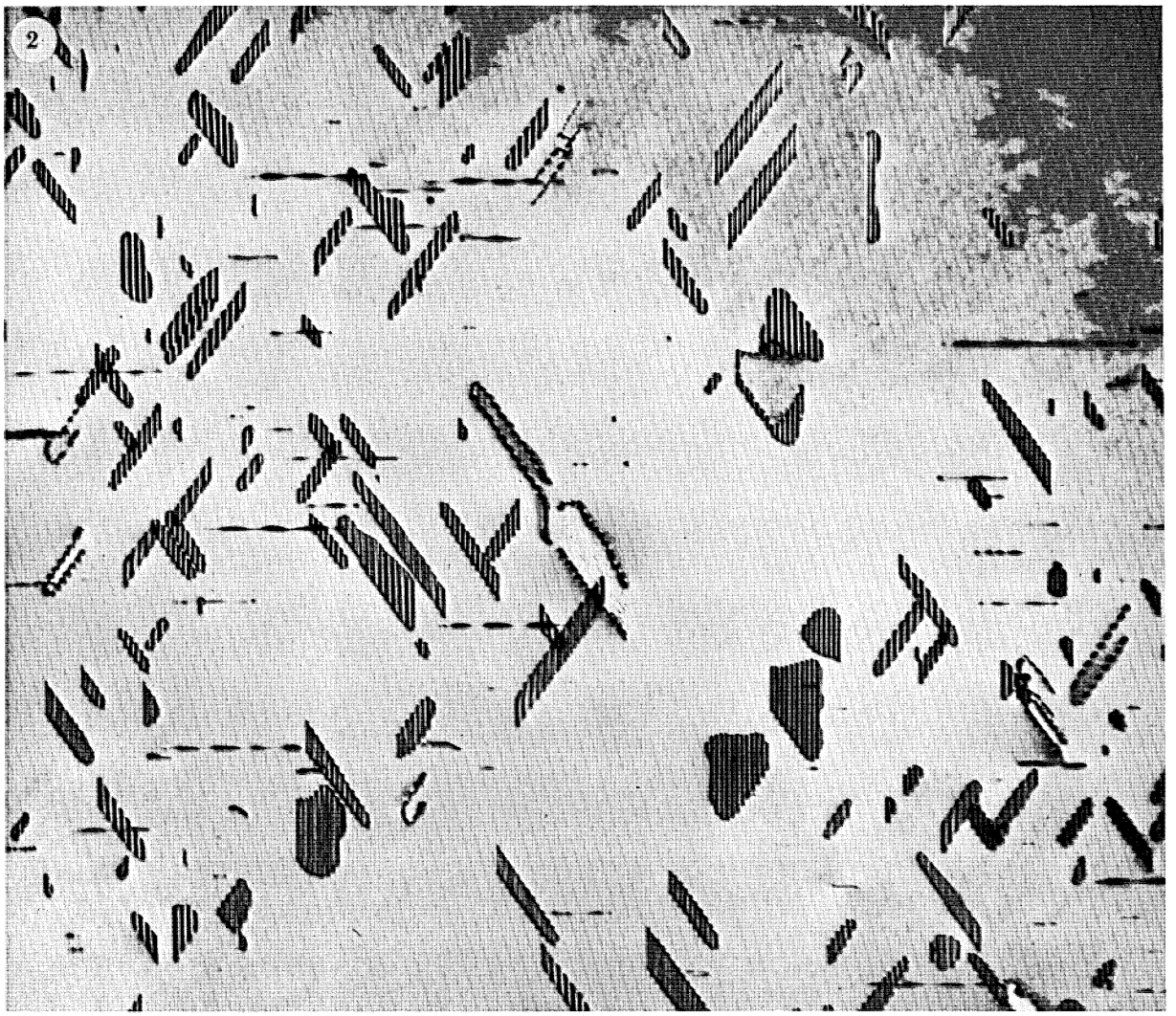

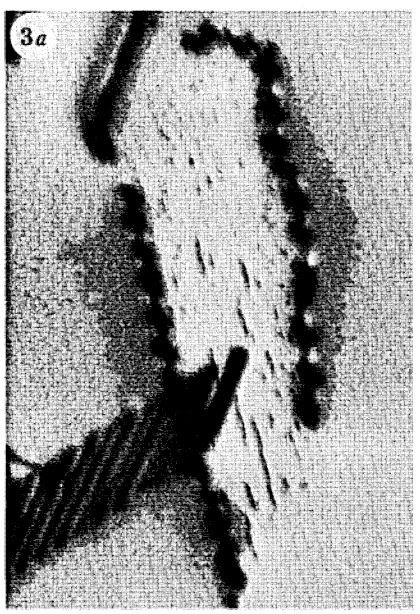

FIGURES 2 AND 3. For description see opposite.

(*Facing p.* 370)

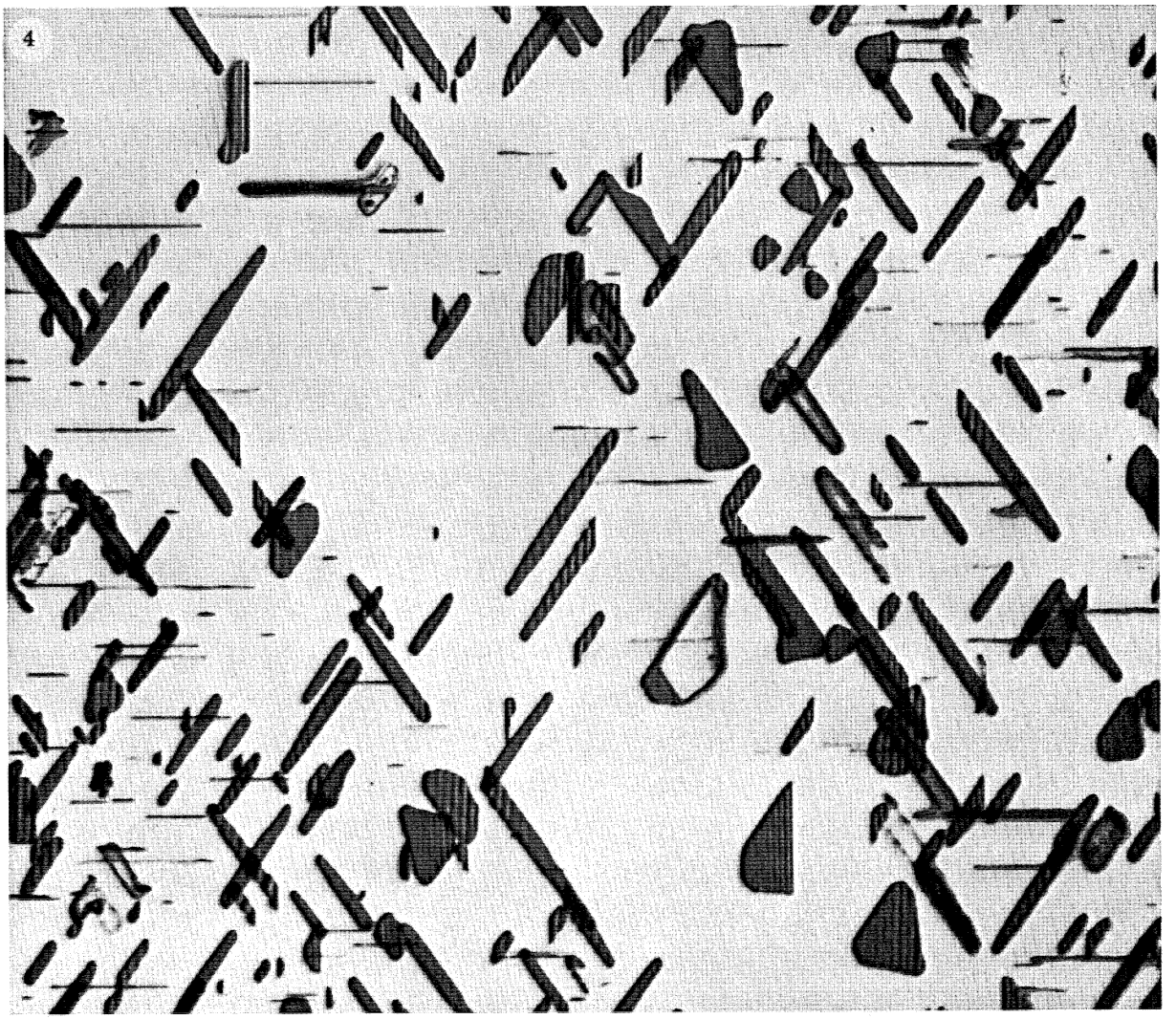

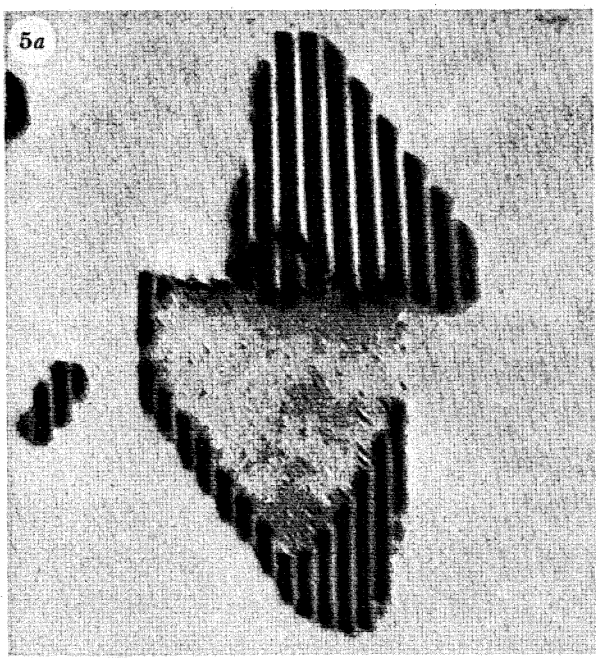

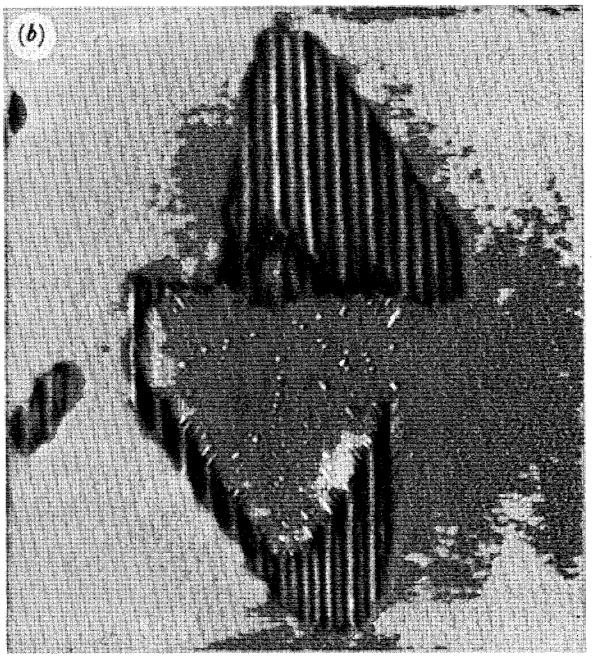

FIGURES 4 AND 5. For description see p. 370.

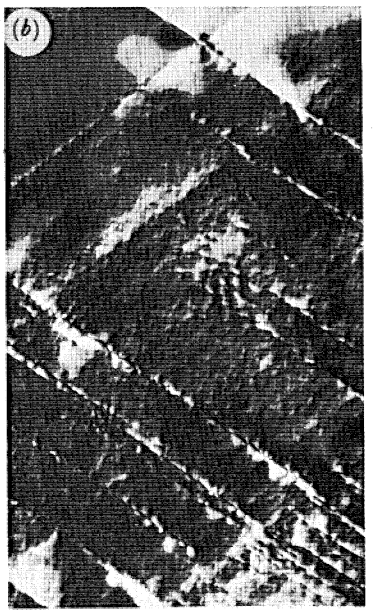

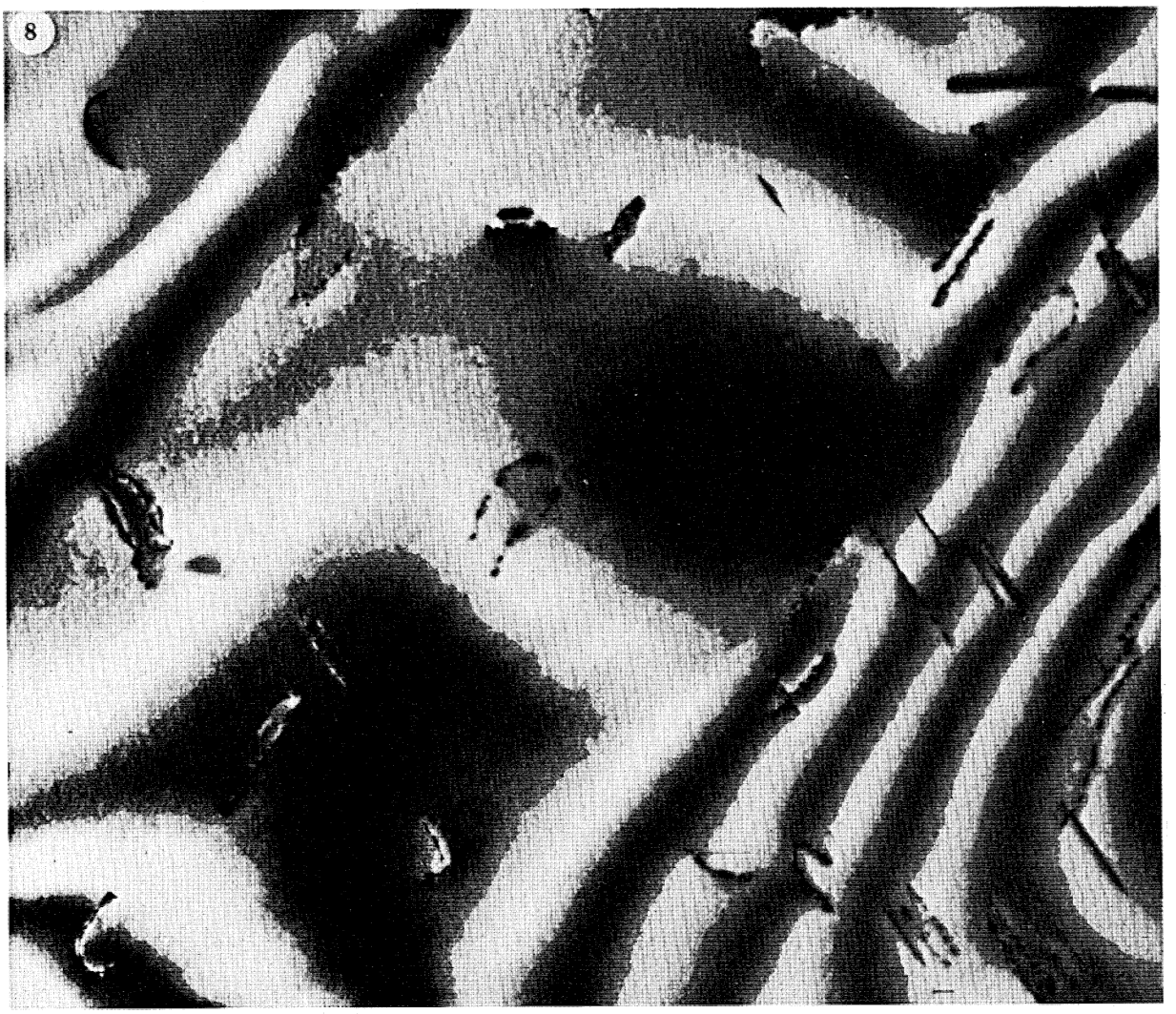

FIGURES 6–8. For description see p. 371.

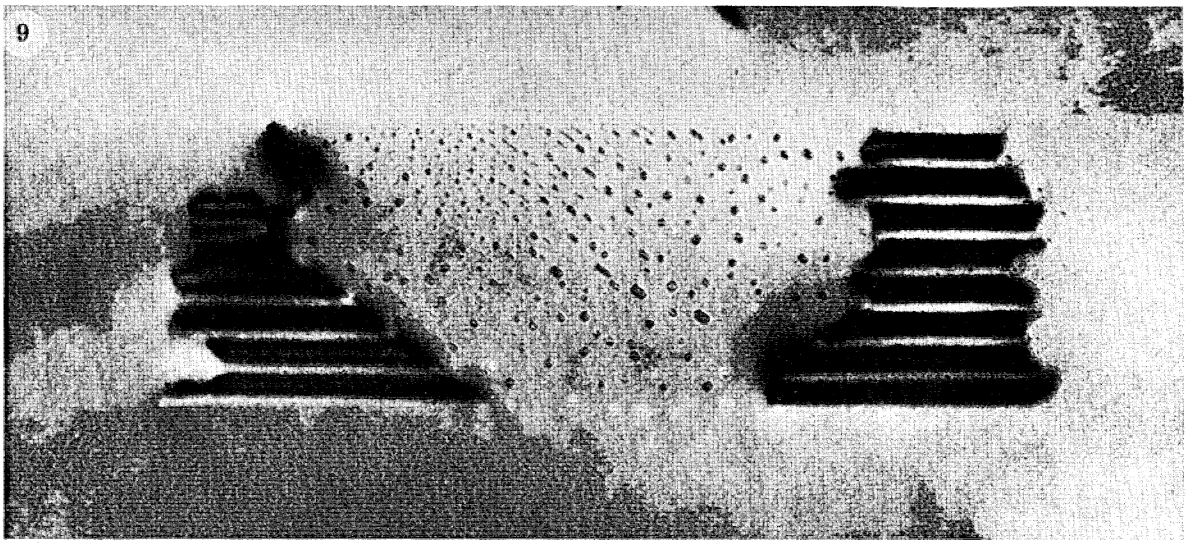

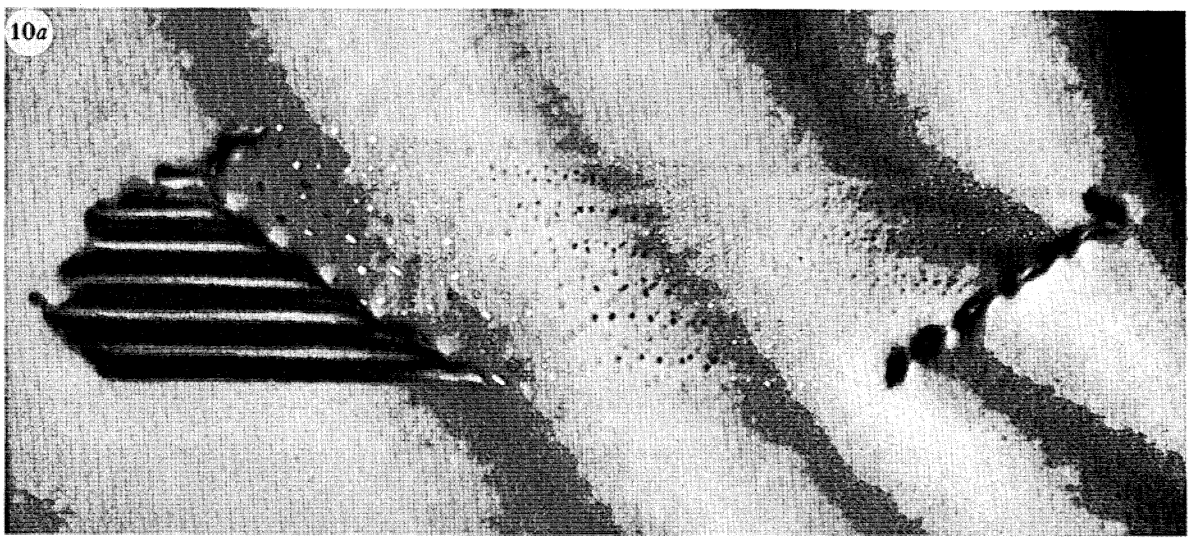

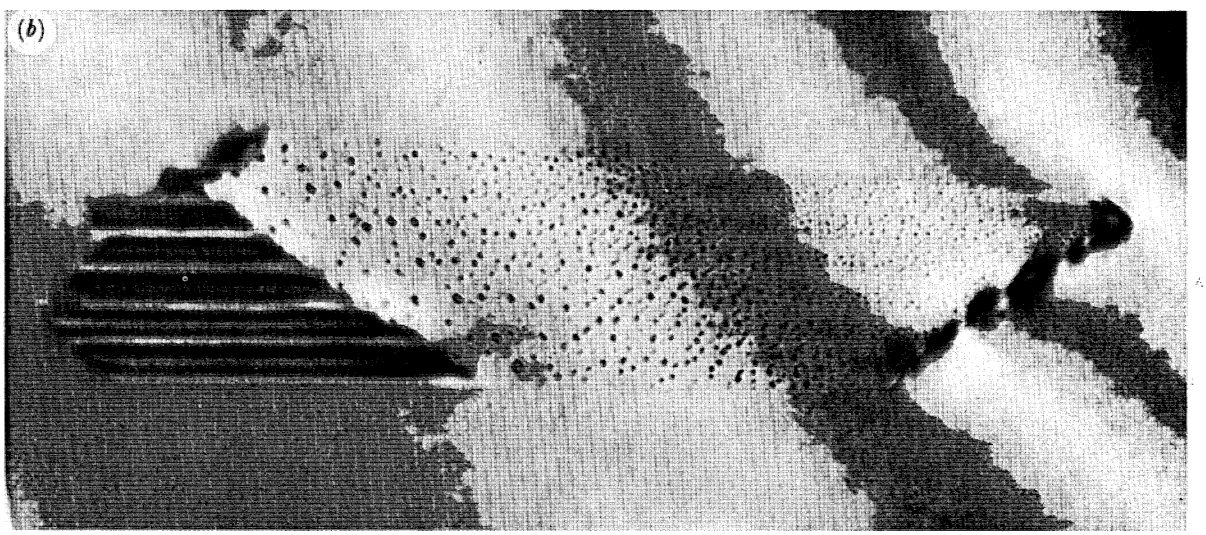

FIGURES 9 AND 10. For description see opposite.

areas from which normal platelet fault-surface contrast is missing. Some statistics derived from micrographs of specimen A4 will be presented in §4.

To learn more about the size and shape of the 'dots' and 'streaks' in A4, the specimen was taken to Oxford for examination in a JEOL JEM 200 CX microscope operated at 200 kV and fitted with an LaB_6 filament, which permitted exposure times as brief as 1 second at magnification as high as 10^5. The first aim was to establish whether these objects were visible by absorption contrast, phase contrast or diffraction contrast due to matrix strain. To this end, numerous through-focus series of micrographs were taken of voidite-containing features. The same [110] zone axis diffraction conditions were retained as far as possible. Figure 3*a*, plate 1, is a high enlargement of the centre of figure 2 where there is a large loop that intersects both top and bottom surfaces of the specimen. More detail of the defects in the plane of the loop can be seen in figures 3*b* and 3*c*, plate 1, which are members of a high-magnification, through-focus series, taken with the 200 CX microscope; figure 3*b* is close to optimum focus, figure 3*c* is underfocused by about 1000 nm. (An intermediate-magnification image of this feature is reproduced in figure 3*a* of Bursill (1983).) Figures 5*a* and 5*b*, plate 2, compare micrographs taken at 120 and 200 kV of the partial platelet at (0.67, 0.60) in figure 2. By means of such high-resolution, through-focus series it was established that the 'dots' and 'streaks' are seen by phase contrast due to difference in electron density between diamond matrix and the volume of the defect, the density within the defect being the lower. Since it appeared possible that the defects were relatively void in comparison with the dense diamond matrix, the term 'voidite' was coined for them as being suitably descriptive without binding description to any particular explanation of their origin. The larger, roughly equiaxed voidites are recognizably faceted parallel to the diamond matrix {111} planes. The 'streaks' are highly elongated octahedra. In figure 5, the partial platelet in the lower half of the field and the apparently normal platelet in the upper half of the field lie on different cube planes. This is evident from the different spacing of their fault fringes, seen most clearly in figure 5*a*, that arises from slight

Description of plate 3

Figure 6. X-ray section topograph through specimen DL4 showing intersecting {111} slip traces. Height of section 2 mm. Direction [00$\bar{1}$] vertical. Bragg reflection 2$\bar{2}$0 obtained in symmetrical transmission through 1 mm thick specimen, projection of diffraction vector points to the right. Cu $K\alpha_1$ radiation, Bragg angle 37.6°.

Figure 7. Birefringence patterns of polished, 50 μm thick, (110) orientation section of specimen DL4 before ion-beam thinning. Field width 0.3 mm. Specimen orientation rotated for strong visibility of (*a*) {111} slip bands, and (*b*) slip-band intersections and individual dislocations.

Figure 8. Panorama of dislocation loops and dipoles filled with voidite sheets, and some individual glide dislocations, in specimen DL4. Specimen thickness is between 0.20 and 0.24 μm. In this and all following micrographs the electron accelerating voltage is 200 kV. Field width 4 μm (6982, original magnification $\times 10^4$).

Description of plate 4

Figure 9. A partial platelet. Both left- and right-hand platelet areas have lobed peripheries; the right-hand boundary between voidite sheet and platelet is also lobed. A few fringing voidites can be seen outside the right-hand periphery of the platelet area on the right, and some voidites can be detected lying on this platelet area. Overall width of the partial platelet image is 0.75 μm. Specimen thickness is 0.22 μm. Here, and also in figures 10–14, the direction [001] is horizontal. The field width is 1 μm, and is also this value in figures 10–15 (7534, original magnification $\times 4 \times 10^4$).

Figure 10. Partial platelet; overall platelet width in image is 0.9 μm, specimen thickness is 0.17–0.20 μm. (*a*) Near-optimum focus, showing depth-dependent cycle of voidite image contrast (7531, original magnification $\times 4 \times 10^4$); (*b*) overfocused image (7530).

departure from exactly symmetrical [110] zone axis diffraction conditions. (Since all specimens are warped to greater or lesser extent, it is impossible to maintain exact [110] zone axis diffraction conditions over a large field of view.) From the size and relative position of these two platelets it is concluded that they have come into contact with each other, and possibly also with a platelet parallel to (001). After some hours under the electron beam these platelets appeared to 'decompose', judged by the loss of fault-fringe contrast, but the new area free from fault fringes did not contain voidites, nor did the process of decomposition appear to affect the existing voidites. Whether the decomposition was initiated by radiation damage, or by stresses produced by local contamination build-up on the specimen surface, is not known. Before attention could be turned to other features, the specimen was accidentally shattered during transfer between specimen holders, and work on this interesting defect population came to an end.

At this time, an investigation of another diamond was being pursued because of its unusual pattern of natural plastic deformation revealed by birefringence. This specimen had been classified as type II by virtue of its transparency in the ultraviolet below 330 nm. It had also suffered some bremsstrahlung irradiation and moderate heating (temperature not greater than 600 °C) by proximity to the electron beam in the NINA synchrotron at the Daresbury Laboratory. The plastic deformation was localized in slip bands parallel to {111} with apparently undeformed, or negligibly deformed, lamellae *ca.* 20–50 μm thick interspersed between the bands of high dislocation density. An X-ray section topograph through the whole 1 mm thickness of the specimen (figure 6, plate 3) and the birefringence patterns of a polished slice of thickness 50 μm cut from it (figure 7*a*, *b*, plate 3) illustrate the style of deformation; individual dislocations can just be resolved locally in these X-ray and birefringence patterns. The dislocation distribution differed so markedly from the very high density typical of type IIa diamonds (Sumida & Lang 1981*a*), or from the high-dislocation-density mosaic structure associated with type IIb diamonds (Hanley *et al.* 1977; Sumida & Lang 1981*b*), that the classification of this crystal as type II came under suspicion. Cathodoluminescence topography showed that the specimen was unusually homogeneous in optical properties, and, surprisingly, that it emitted the H4 system with sufficient strength to mask detection of the H3 system, as far as could be discerned by visual spectroscopic examination. Infrared absorption measurements confirmed that the specimen was of the rare type IaB, or very close to this limit, with, at most, a very weak B′ peak. Recalling the discussion of optical properties in §2*b*, the reason for the previous incorrect optical classification was apparent. The average absorption coefficient $\mu_B(7.8)$ was 0.37 mm^{-1}, which would suggest from equation (3*c*) a rather low nitrogen content of about 0.04%. A measurement of the H4:H3 ratio from the relative strengths of the zero-phonon lines in absorption was kindly carried out for us by Dr Gordon Davies, King's College, University of London, who found the very high value of 17.4. A specimen prepared for electron microscopy by ion-beam thinning the slice shown in figure 7 possessed a satisfactory smooth surface but was rather warped. The low-magnification panorama shown in figure 8, plate 3, is typical of a region remote from the slip bands. It shows only a few isolated glide dislocations; the majority of the dislocations seen belong to dipole loops bounding voidite sheets on cube planes. This specimen slice, designated DL4/A, provided the bulk of the observations described below; those micrographs exhibited that are not of this slice have their specimen identification stated in the figure legends. After study by high-resolution [110] zone axis micrography at Oxford, it was intended to perform experiments with a high-tilt stage at Bristol, but the specimen was lost at Oxford. However, a second specimen from the same crystal, DL4,

was prepared, designation DL4/B, and a number of partial platelets were photographed in the Philips EM 400 microscope under various two-beam diffraction conditions. Unfortunately, this new specimen had a poor surface, which has impeded analysis of the micrographs, and data are still in the process of extraction from them (Sumida & Lang 1987). Specimen DL4/B was then taken to Oxford. Two micrographs of edge-on views of voidite sheets in DL4/B are included in this report (figure 29, plate 12, and figure 30, plate 13). Although the diverse properties of partial platelets, voidites and their associated dislocations to which we desire to draw attention are manifest in some measure in all the micrographs we show, we have attempted to order our description of the micrographs by concentrating in turn on observations primarily concerned with partial platelets, or with dislocation loops, etc., with a final table listing a selection of voidite phenomena deemed noteworthy, and the micrographs in which they are principally exhibited.

(*b*) *Voidites and partial platelets*

Figures 9–15 (plates 4–6) have been selected to illustrate some principal properties of voidites and partial platelets, including simpler interactions between platelets and dislocations. All the platelets concerned have diameters several times greater than the specimen foil thickness. Hence the long axis of their images lies along [001] in (110) projections, and for convenience all these micrographs (except figure 15, plate 6) are oriented with the long axis of the field also parallel to [001] and horizontal. The micrographs in figures 9–15 are reproduced at the same magnification (1.6×10^5), so that they all contain the same field width, 1 μm. The magnification of reproduction is adequate to reveal most of the features referred to in the text, but it is unavoidable that in these and following figures some features alluded to that are small (diameters of order 1 nm), or of low contrast, are only readily recognizable on the original films and prints. The specimen thicknesses in figures 11–15 lie between 0.12 μm and 0.25 μm, and the corresponding width of the strip of partial platelet contained between the upper and lower specimen surfaces is $\sqrt{2}$ times the local specimen thickness. The dimensions of the partial platelet images in the [001] direction range up to 0.9 μm. It is not known whether these partial platelets are elongated parallel to a ⟨110⟩ direction or are roughly equiaxed. The latter case is believed to be more likely in this region of the crystal DL4. Most of the micrographs reproduced are near optimum focus for revealing the size and shape of voidites. It must be borne in mind that with specimen thicknesses as great as $\frac{1}{4}$ μm, say, voidites seen sharply focused close to one surface of the specimen may appear out of focus when close to the other surface. When the voidite population is dense, and the contrast conditions favourable, it can be verified that the trace of the voidite sheet outcrop at a surface of the specimen follows the trace of the cube plane of the platelet, to within a voidite diameter (see, for example, the upper margin of the voidite sheet image in figure 9, plate 4, and the lower margin of the voidite sheet image in figure 14, plate 6). We interpret all these partial platelet images as showing that a large platelet has transformed over part of its area into a sheet of discrete faceted 'negative crystals' of unknown internal content but of lower mean density than the surrounding diamond. We will now consider some of the features illustrated by figures 9–15, dealing first with the voidite sheets and then with the area that shows normal platelet fault fringe contrast.

Euhedral images of voidites

Relatively few voidites with clearly resolved {111} facets do not show some departure from the equiaxed octahedral habit. The largest equiaxed octahedra seen in figures 9–15 have an edge length of 10 nm. At the magnification of these micrographs, the lower size limit for

detection of equiaxed voidites is determined mainly by film granularity, and is about 1 nm. It is difficult to judge whether there is any corner truncation of the voidite octahedra. The voidite thickness parallel to the [110] viewing direction tapers to zero at the apices of the octahedron that point towards [001] and its inverse direction, and the voidite image contrast will likewise go to zero at these apices. An appearance of minor truncations parallel to (001) and $(00\bar{1})$ seen in many voidite images at magnifications of about 10^5 is probably attributable to this taper. In the highest-magnification images of voidites described below (§3*e*), no corner truncation is positively detectable. Under the right diffraction conditions, e.g. in the dark extinction contour covering the left-hand edge of the voidite sheet in figure 10*a*, plate 4, it can be seen that the variation of voidite contrast with distance from the specimen surface follows the cycle: lighter, equal to matrix, darker, equal to matrix, lighter, etc., with respect to the blackness of image of surrounding matrix on the print. The periodicity is the same as the dominant period in the platelet fault fringes. This behaviour is just that expected for a pure phase-contrast object, and is in qualitative agreement with simulations performed for octahedral voidites viewed parallel to a cube axis situated at various depths within a specimen foil having cube-plane orientation (Anstis & Hutchison 1982).

Elongated voidites

Although the majority of voidites are elongated, the degree of elongation varies greatly from sheet to sheet, and within a given sheet. Some highly elongated voidites are seen in figure 13, in the region (0.4, 0.6) where they reach 50 nm in length projected on (110); their actual length parallel to the ⟨110⟩-type axis of elongation is 15% greater. Voidites with a comparably high elongation appear in figure 26, plate 11, and the features first noticed as streaks in early micrographs of specimen A4 are voidites with long axes approaching 100 nm in extreme cases. Most of our examples of conspicuously elongated voidites appear in voidite sheets that also show a gradient in average voidite size, which we now describe.

Description of plate 5

Figure 11. Annular partial platelet with lobate periphery. Overall platelet width in image is 0.6 μm, specimen thickness is 0.12–0.14 μm (7525, original magnification $\times 5 \times 10^4$).

Figure 12. Partial platelet with small fraction of image area occupied by voidite sheet. Overall width of partial platelet image is 0.65 μm, specimen thickness is 0.2 μm. Dislocations on right of field are not associated with the partial platelet (7529, original magnification $\times 4 \times 10^4$).

Figure 13. Partial platelet with high ratio of voidite sheet area to platelet area in the image. Highly elongated voidites appear in upper part of image of voidite sheet. Width of partial platelet image is 0.9 μm, specimen thickness is 0.23–0.25 μm (7532, original magnification $\times 4 \times 10^4$).

Description of plate 6

Figure 14. Partial platelet with a very narrow band of platelet contrast on left of voidite sheet. A single dislocation lies across voidite sheet and platelet areas on the right. Periphery of platelet is lobate, with, on the right, fringing voidites and voidites on the platelet. Overall width 0.9 μm, specimen thickness 0.2 μm (S7011, original magnification $\times 5 \times 10^4$).

Figure 15. Partial platelet with dislocation dipole lying in, or very close to, platelet. Lobate periphery, fringing voidites and voidites on the platelet are noteworthy. Maximum dimension of platelet image is 0.9 μm, specimen thickness is 0.18 μm. (*a*) Near-optimum focus (Q7005, original magnification $\times 4 \times 10^4$); (*b*) underfocused to bring out contrast of voidites on the platelet area (they can be seen as white dots (Q7008)).

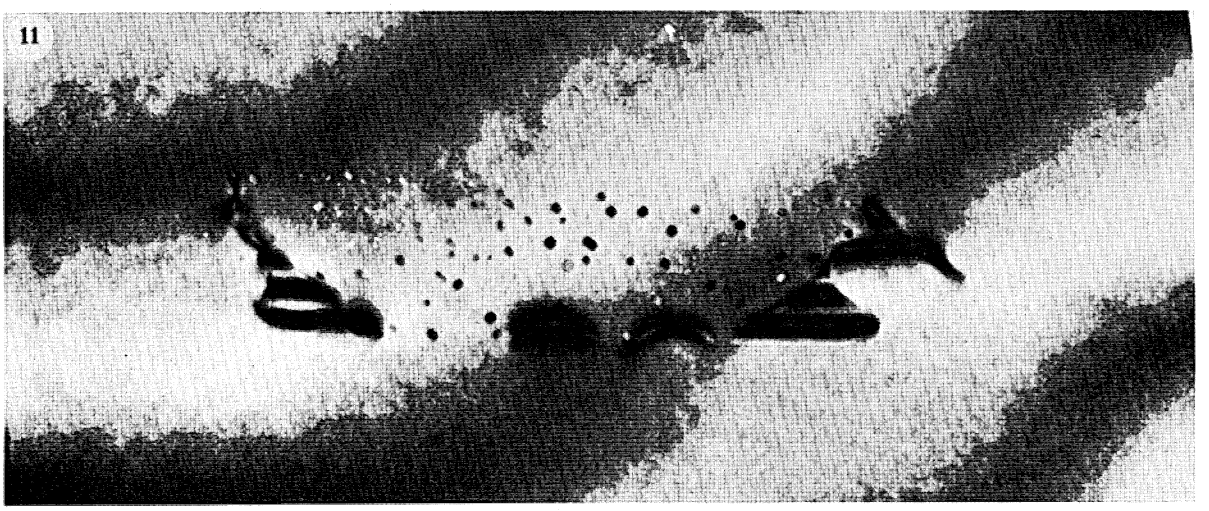

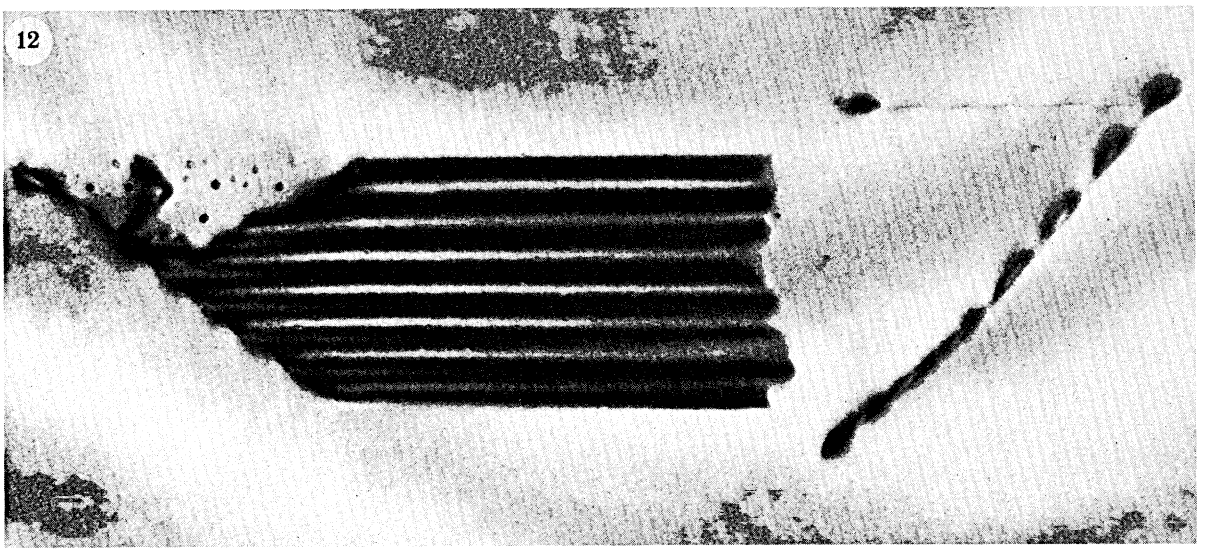

FIGURES 11–13. For description see opposite.

(*Facing p.* 374)

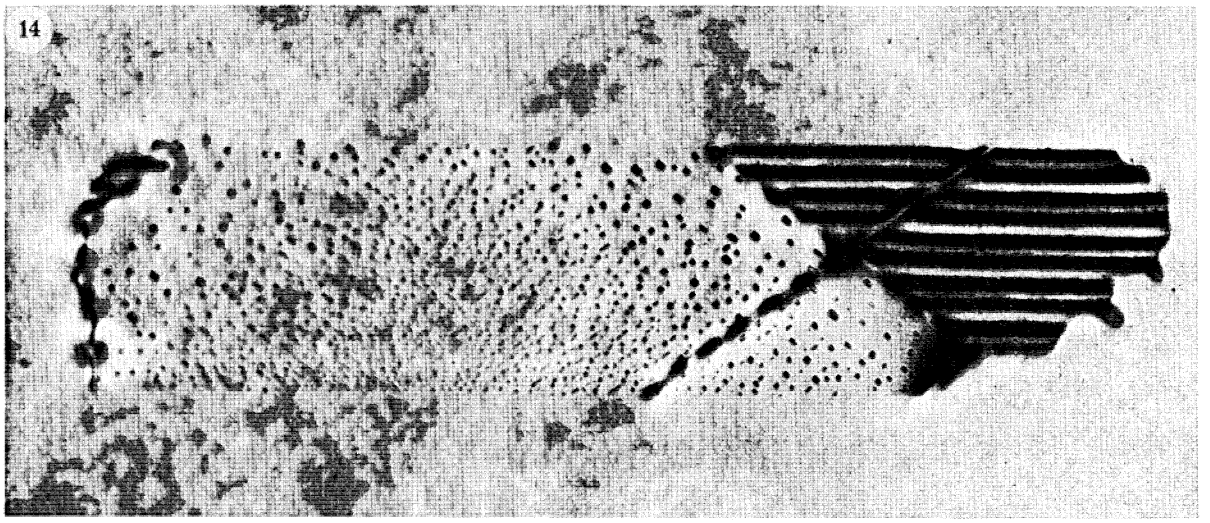

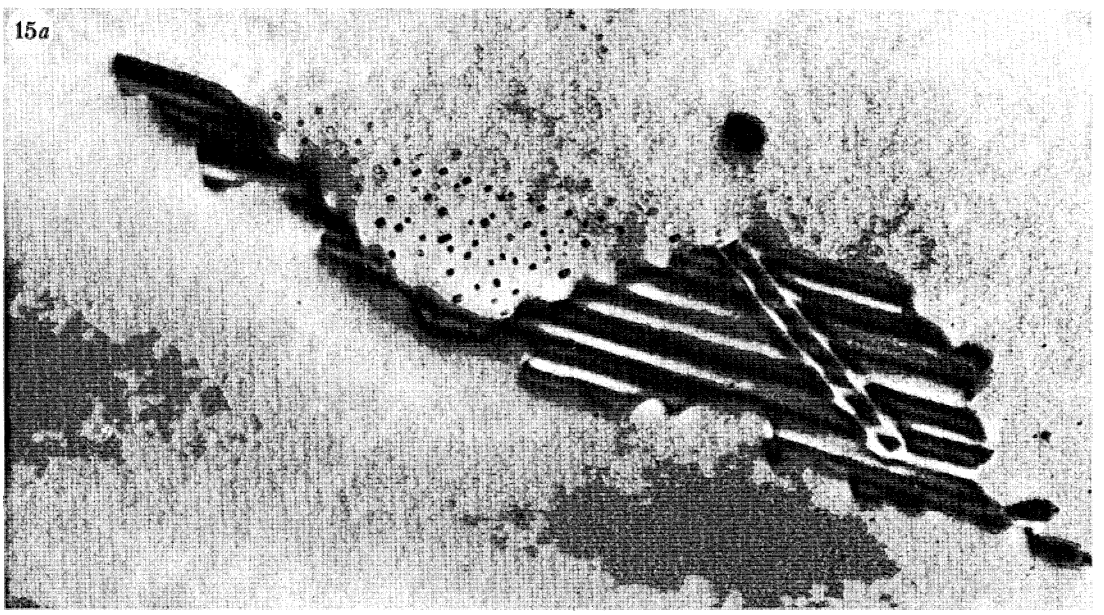

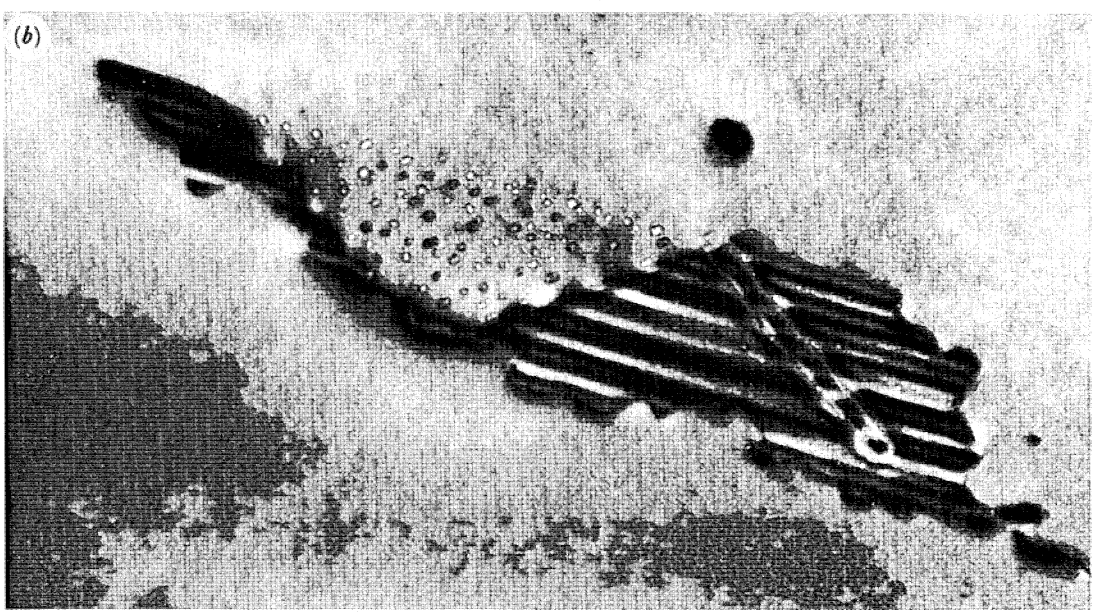

FIGURES 14 AND 15. For description see p. 374.

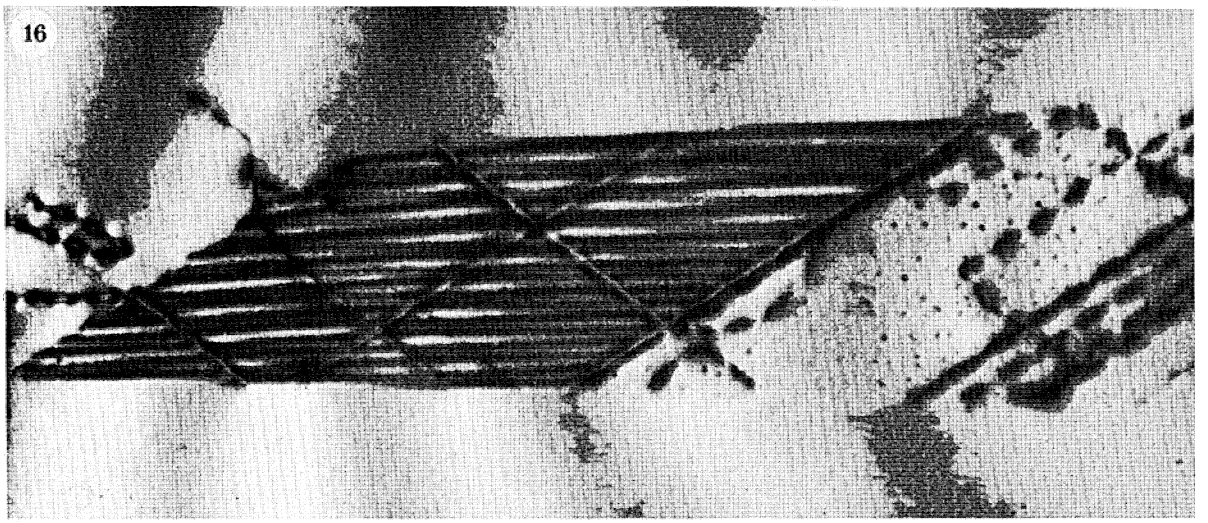

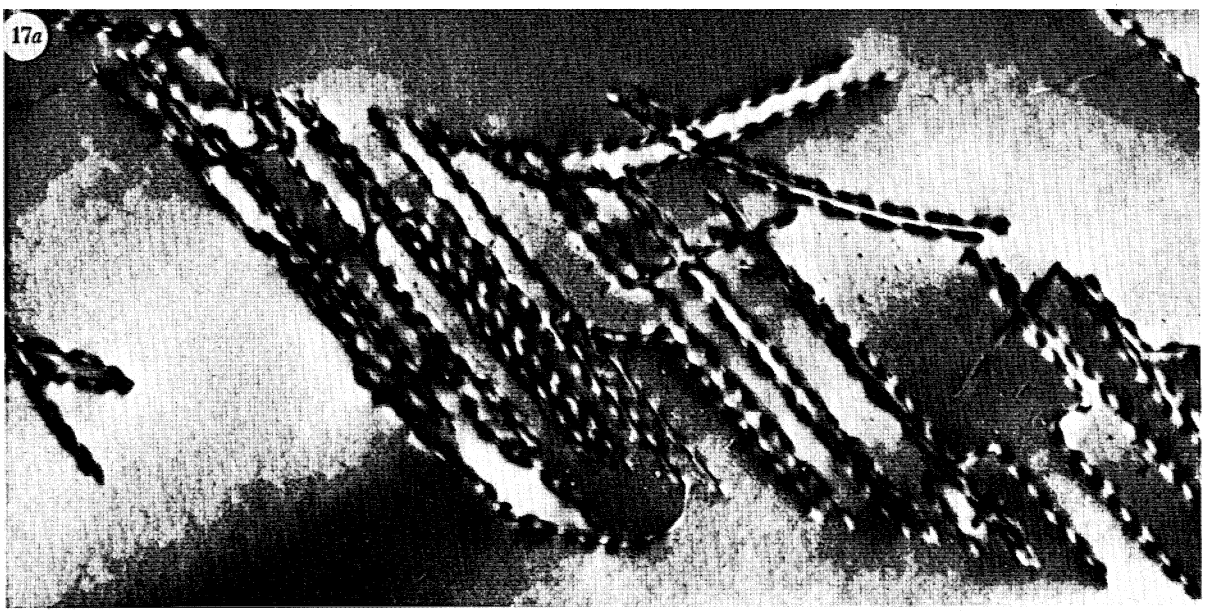

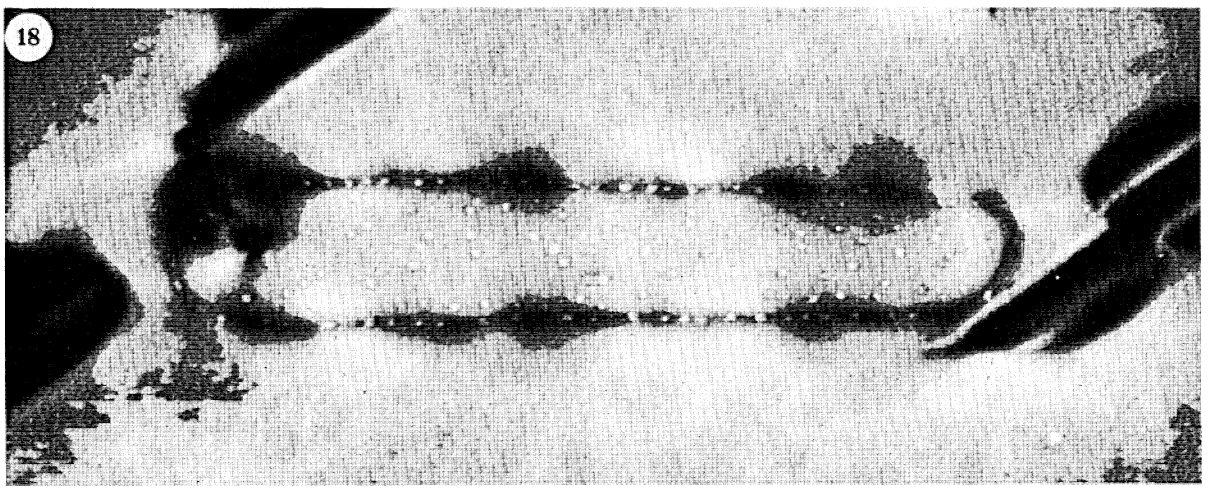

FIGURES 16, 17*a* AND 18. For description see p. 375.

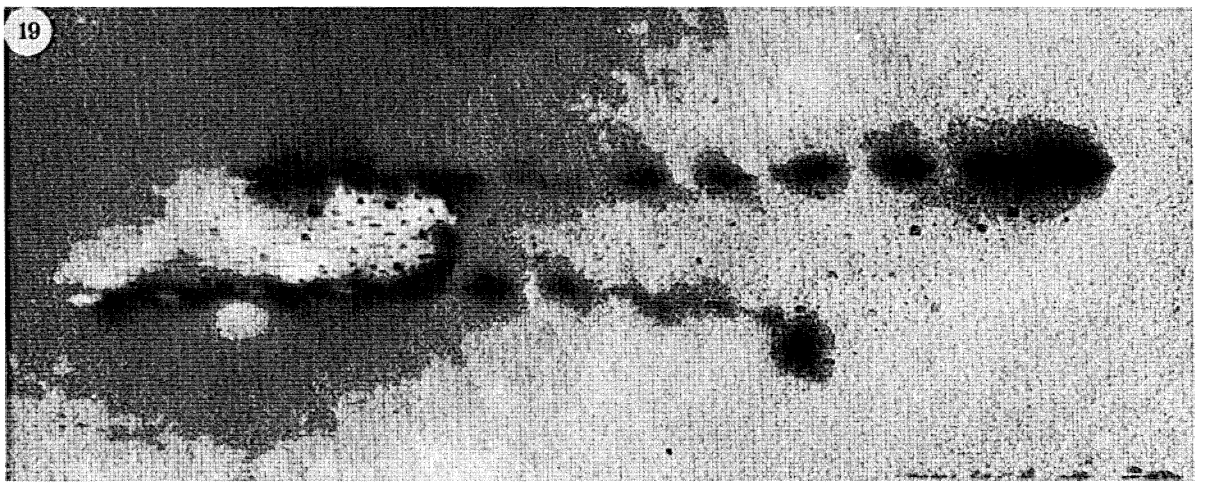

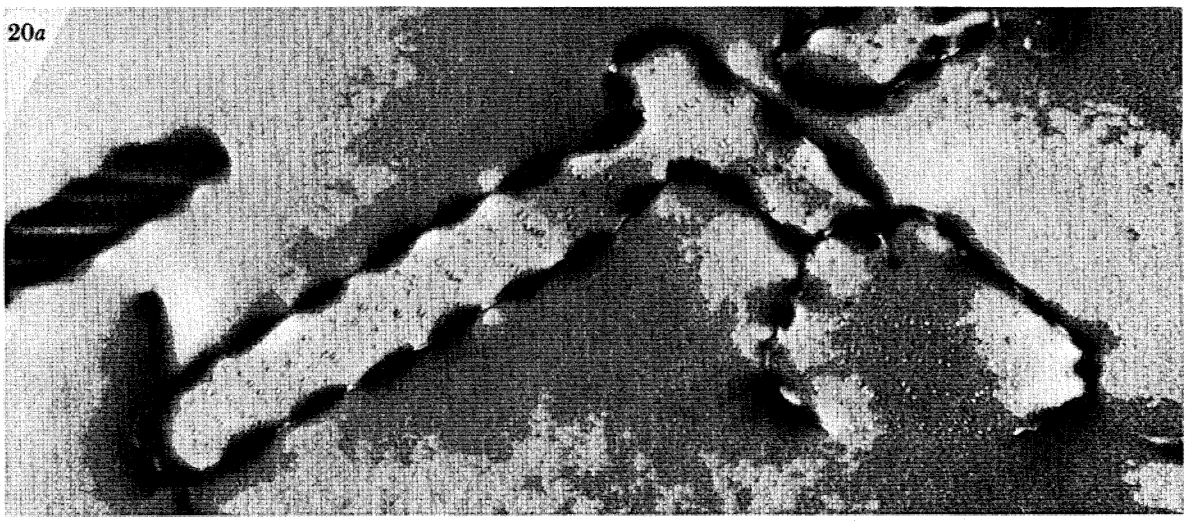

FIGURES 19 AND 20. For description see opposite.

Spatial variation of voidite size

In about half the voidite sheets associated with partial platelets illustrated in the figures, there is an obvious variation of mean voidite size with position in the sheet. Examples are seen in figures 9, 10, 13 and 14. In some cases, a strong impression is obtained that voidite size increases with distance from a 'radiant point' not far outside the strip of voidite sheet captured between top and bottom surfaces of the specimen. This impression is enhanced by the tendency of the voidite elongation axis to point towards the 'radiant'. Thus, for example, one infers that the radiant might have been situated in the missing extensions of the voidite sheet at positions which project on the specimen plane at roughly (0.35, 0.9) in figure 9, plate 4, and (0.35, 0.1) in figure 14, plate 6. An observation related to that just described is the tendency for the largest and most sparsely distributed voidites to be located near the boundary between voidite sheet and platelet areas (see figures 10, 13 and 14).

'Annular' partial platelets

The boundary between voidite sheet and platelet is always sharply defined, and often has long segments parallel to a ⟨110⟩ direction, see, for example, the left-hand boundary of the voidite sheet in figure 10 and the right-hand one in figure 14. The fraction of the total partial platelet area captured in the micrographs under discussion is too small for a reliable estimate of the relative areas of platelet and voidite sheet to be made, and an attempt at reconstructing their overall shapes would be even less convincing. Nevertheless, there is abundant evidence of a tendency for voidite sheets to be surrounded along part of their peripheries by a strip of platelet whose width is small, sometimes very small, compared with the partial platelet diameter, so that the overall configuration would be describable, at least in part, as a voidite sheet surrounded by a platelet annulus. The partial platelet shown in figure 5 falls within the category 'annular', and that at (0.60, 0.35) in figure 4 is a striking example. (It is particularly

Description of plate 7

Figure 16. Major part of image of a large partial platelet whose total intersected length parallel to [001] (i.e. in the horizontal direction) is 1.7 μm. Glide dislocations lie in plane of platelet and voidite sheet. The specimen thickness is 0.24 μm on the left, rising to 0.33 μm at the right-hand edge of the partial platelet, beyond the limits of the field printed. Voidites on the platelet are detectable. Field width $1\frac{1}{3}$ μm (7533, original magnification $\times 3 \times 10^4$).

Figure 17*a*. Voidite sheet with many dislocations in and near the sheet. Direction [001] rotated 13° clockwise from horizontal. Specimen thickness is 0.32 μm. Field width is $1\frac{1}{3}$ μm (K6972, original magnification $\times 4 \times 10^4$).

Figure 18. Voidite-containing dislocation loop completely within the specimen. Direction [001] rotated 35° anticlockwise from horizontal. Field width 0.5 μm, the actual loop length is 0.4 μm and its width is variable between 50 and 60 nm. Defocus chosen to show up voidites strung along the dislocation (4728, original magnification $\times 10^5$).

Description of plate 8

Figure 19. An H-feature comprising a voidite-containing pair of dislocations intersecting both upper and lower specimen surfaces with a bridging dislocation within the specimen. Orientation same as in figure 18. Field width is $\frac{2}{3}$ μm. Observe highly elongated voidites on left of the bridge. On the right there is a 'bimodal' voidite size distribution: some larger voidites with diameters of about 5 nm dispersed in a sea of small, weakly visible voidites having diameters of about 0.5 nm (R7010, original magnification $\times 3 \times 10^4$).

Figure 20. Voidite-containing dislocation loops. Direction [001] is horizontal, field width is 0.8 μm. Comparison of (*a*) bright-field (4706, original magnification $\times 6 \times 10^4$), and (*b*) dark-field image, 111-type reflection (4707).

regrettable that specimen A4 was lost before the latter partial platelet could be studied at high resolution.) In the majority of figures 9–15, some annular characteristics in the partial platelets are evident (figures 11, 13, 14 and 15), and it could be held that figure 9 also shows part of an annular partial platelet. Noteworthy is the left-hand boundary of the voidite sheet in figure 14. The lower segment of the boundary appears no different from the image of a single dislocation, but its upper segment widens into a strip of platelet up to 40 nm in width. There is a similar occurrence at the right-hand boundary of the voidite sheet in figure 13; the strip of platelet here varies in width from 100 nm down to less than the minimum resolvable strip width (*ca.* 10 nm) under the locally applying condition of strong diffraction by many beams.

Indented platelet peripheries and fringing voidites

Whereas the boundaries between internal voidite sheets and their surrounding platelet areas tend to be straight and parallel to a ⟨110⟩-type axis (but by no means always so, see, for example, the right-hand boundary of the voidite sheet in figure 9), the outside boundaries of the platelet areas belonging to the partial platelets shown in figures 9–15 are all indented or wavy to some degree unless they coincide with a ⟨110⟩ direction, as does the left-hand boundary in figure 12, plate 5. In some cases, the partial platelet periphery is quite markedly lobed (figures 14 and 15). The larger, more equiaxed platelets in specimen A4 also show some waviness in platelet periphery when it does not lie along a ⟨110⟩ direction. The platelets at (0.2, 0.1) and (0.7, 0.3) in figure 2 exemplify such wavy peripheries. Outside the indented peripheries of partial platelets we can sometimes detect a few small voidites, which we shall refer to as 'fringing voidites'. They are well seen outside the right-hand edges of the platelet areas in figures 9, 14 and 15. With regard to the platelet area itself, we emphasize that with one possible exception we have not detected any difference between the fringe contrast of the platelet areas belonging to partial platelets and that exhibited by apparently normal platelets not associated with voidites. The possible case of fringe contrast abnormality is to be seen near the right-hand margin of the partial platelet in figure 15, but it seems likely that the influence of the dislocation dipole lying on or close to the platelet is responsible for the irregularity in the fringe pattern observed here. However, this region of the partial platelet is of interest because it very clearly shows voidites lying *on* the area with apparently normal platelet fringe contrast. Further instances of this occurrence will be reported in §3*d*, and in none of them does any fringe contrast abnormality appear.

(*c*) *Voidites and dislocations*

In the study of dislocations associated with voidites, the restriction of observations to a single specimen orientation, that giving the [110] zone axis image, has not proved as serious a handicap to interpretation of the geometry of the dislocation configurations as might be expected. There are usually present some clues which reduce the range of possibilities in the orientation of the dislocations. This is especially true in most of the cases of present concern when the dislocation line is bounding or lying in a voidite sheet that has verifiably a cube-plane orientation, as evidenced by the [001] direction of the traces of the sheet outcrops on the specimen surface. A greater lack is the absence of Burgers vector determinations; generally all that can be said is that very weak dislocation images correspond to a Burgers vector parallel to the electron beam. In our description, we shall pass from features that contain some platelet contrast to those in which it is absent, proceeding generally in the direction of greater complexity.

Dislocations lying on voidite sheets and platelets

A single dislocation may be seen on the small area of voidite sheet contained in the field of figure 12; the dislocations appearing in the right-hand part of the field are independent of the partial platelet. Two dislocations are seen lying in the partial platelet shown in figure 13, and they are involved in a reaction with the dislocation that forms the left-hand boundary of the sheet. Regarding the single dislocation lying across both voidite sheet and platelet areas in figure 14, and the dislocation dipole in figure 15 previously referred to, one does not perceive any obvious involvement of these dislocations with the processes that have led to the present loci of boundaries between voidite sheet and platelet areas; it is possible that the single dislocation and the dipole could have come to their present positions after the partial platelet attained its present state of development.

Figure 16, plate 7, shows the major part of a strip of a very large partial platelet in whose plane many dislocations lie. In attempting to interpret this pattern it must be remembered that each platelet makes equal angles with all four {111} glide planes, and each of the two ⟨110⟩-type directions in a given platelet lies in a pair of {111} planes, one of which is normal to the (110) specimen surface while the other makes 35° with (110). The [110] viewing direction possesses much degeneracy. However, inspection of the neighbourhood of the platelet will generally indicate which glide systems are dominant in that vicinity. In the neighbourhood of the partial platelet shown in figure 16 the dislocation density is low, but enough dislocations are seen to indicate that the principal glide planes are (111) and/or $(11\bar{1})$. One cannot be certain that the dislocations lying on the voidite sheet in the right hand of the field reached that plane before the transformation from platelet to voidites occurred there, but it is deemed likely. The present boundary between voidite sheet and platelet areas lies close to but not coincident with one of the straight dislocation segments. Close inspection of the original film shows that the platelet boundary is slightly wavy and keeps a few nanometres to the right of the straight dislocation, being distant up to 20 nm from it in the upper-right part of the field.

Figure 17*a*, plate 7, contains a large voidite sheet in whose plane many dislocations lie, but other dislocations, including some dipoles, lie close to but not in the sheet. As in figure 16, the dominant glide plane is (111) or $(11\bar{1})$. To help in understanding figure 17*a*, a sketch of the image is shown in figure 17*b* with the outcrops of the voidite sheet emphasized. The voidites

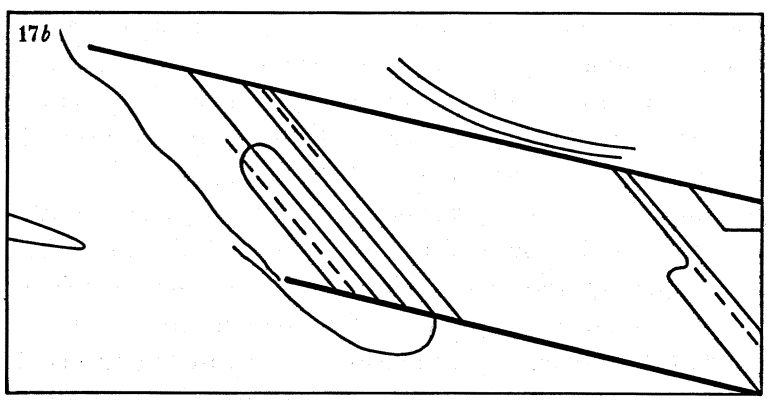

FIGURE 17*b*. Sketch of field of figure 17*a* emphasizing the outcrops of the voidite sheet included in the field (bold lines), a few dislocation landmarks (fine lines), and the fine lines of dark contrast referred to in text (broken lines).

are sparse and rather small compared with the voidite populations already discussed. The image contains some faintly visible fine dark lines parallel to the dominant ⟨110⟩ direction of the dislocations. The position of these lines is indicated by the interrupted lines in figure 17*b*. The lines may be very narrow, highly elongated voidites (effectively fine tubes), but the possibility of a strain-contrast component in the generation of their images cannot be excluded. A similar, but more strongly visible feature appears in figure 26 (plate 11) and is discussed below in §3*d*.

Dislocation loops and dipoles containing voidites

Some dislocation dipoles which lie in ⟨110⟩ directions and contain voidite sheets are 60° dislocations with their Burgers vector making 45° with the plane of the sheet. Thus these dipole loops are 50% prismatic, 50% shear in character. This knowledge of Burgers vector comes from the early work of Woods (Woods 1976; Lang 1977) in which voidite sheets were not detected (but can be safely assumed to have been present), from the analysis of a voidite-containing loop by Stephenson (1977) and from more recent work on specimen DL4/B. Other, rather surprising, findings regarding loops in DL4/B are reported in §4*a*iii. The configurations of dislocations associated with voidite sheets on (100) and (010) illustrated here can be categorized as follows. First, there are entire dipole loops, of which figure 18, plate 7 shows an example. In this case, the [110] view does not identify the crystallographic form of the plane of the loop, but since a voidite sheet within the loop is resolved, the cube-plane orientation of the loop is certain. Secondly, when one or both ends of a dipole loop elongated parallel to a ⟨110⟩ direction are truncated by the specimen surface, the observation that the line joining the pair of dislocation outcrops on the same specimen surface is parallel to [001] within the accuracy of measurement identifies a cube-plane orientation of the loop, whether voidites are resolved or not. This situation applies, for example, to the pair of dipoles seen at (0.9, 0.1) in figure 8, and to the many voidite-containing loops having one end truncated which appear in figure 2. In the third category, there are pairs of dislocations between which lies a voidite sheet, and one or both members of the pair deviate slightly from a ⟨110⟩ direction, for example as seen in figure 3 and figure 19, plate 8, or more markedly so, as in figure 26, plate 11, and in the V-shaped pair on the right in figure 27, plate 12, but where in all cases the presence of a voidite sheet and/or the [001] direction of the line joining dislocation outcrops makes the cube-plane orientation of the loop or line pair evident. Lastly, however, there do exist more complex dislocation loops associated with voidites where at least part of the loop is not contained within the cube plane of the voidite sheet. This departure from planarity is usually observed in association with reactions between loops or platelets belonging to two, or perhaps all three, of the orthogonal cube planes. Some probable examples can be seen in figure 4 at (0.3, 0.8), in figure 8 at (0.17, 0.5), and close to the point (0.33, 0.42) in figure 28, plate 12.

Returning to the entire loop shown in figure 18, one observes at its top left corner (in the orientation of the print) the edge-on image of a voidite sheet parallel to (001). The length of the latter image is similar to the width of the entire loop and of some of the lath-like platelets in the vicinity. Consequently, this edge-on image is interpreted as belonging to a voidite-containing loop elongated along [110] that in all probability contacts the entire loop. Detail in the region of overlap of the images of the two loops is obscured by strong diffraction contrast due to strain. Figure 18 shows well the voidites strung along the dislocation line: the defocus chosen enhances their visibility. This decoration phenomenon is ubiquitous in the case of dislocations associated with voidite sheets, but is not easily recognizable in photographic prints because of masking by the high contrast of the dislocation image.

Figure 19, plate 8, shows a voidite-containing pair of dislocations that intersect both specimen surfaces. A dislocation bridges the pair within the specimen, and from the resulting appearance this configuration is called an H-feature. Noteworthy is the difference in the shapes and size distribution of the voidite populations on either side of the bridging dislocation: observe the strongly elongated voidites on the left and absence of elongation on the right. In another H-feature (figure 25, plate 10), discussed in §3*d*, no significant difference between characteristics of the voidite population on either side of the bridging dislocation is observed. Figure 20*a*, *b*, plate 8, shows a complex loop configuration in bright and dark field imaging, respectively. The voidites within the dislocation loops show well in both images, but those strung along the dislocation lines show much better in the bright-field image. The [110] zone axis bright-field setting provides the most effective method for imaging the overall distribution of voidites, whether on or remote from dislocations. A field with several voidite-containing loops is shown in figure 21, plate 9. A small normal platelet appears in the field at (0.45, 0.15). The edge-on feature close by, at (0.35, 0.15), has the type of contrast associated with edge-on images of platelets rather than of voidite sheets. The right-hand dislocation belonging to the dipole that runs vertically in this view, close to the right-hand margin of the field, reacts with a dislocation that produces strong diffraction contrast in the right-hand bottom corner of the field. At (0.98, 0.21), the image of a voidite sheet parallel to (001) can be discerned, and it is apparent that the dislocation in strong contrast lies close to, but not exactly in the plane of, this voidite sheet. Loops more equiaxed are shown in figure 28, plate 12. In the case of the loop segment in the top right of this field, the main voidite sheet obviously lies on its right hand, but a number of voidites can be seen to the left of this dislocation segment as well as lying on the dislocation itself. There are also voidites in the region around (0.30, 0.38) that are not contained within loops.

(*d*) *Particular observations concerning voidite contrast and distributions*

Here we record a variety of observations, some quite puzzling, that need to be explained before the process of voidite formation can be regarded as sufficiently understood. In the list that follows, we start with a phenomenon briefly mentioned at the end of the discussion in §3*b* concerning indented platelet peripheries and fringing voidites.

Voidites on platelets

In figure 22*a*, *b*, plate 9, two partial platelets are seen. The partial platelet segment constituting the left-hand image is of annular type, whereas the right-hand image suggests a lath-like platelet partly converted to a voidite sheet. The edges of the latter platelet appear slightly wavy, although departing not more than a few degrees from a mean ⟨110⟩ direction. The dislocation pair bounding its adjoining voidite sheet bend up to 15° away from the projection of this ⟨110⟩ direction on (110). The two micrographs reproduced have been selected from an eight-step through-focal series as being the best pair, taken in combination, for revealing the voidites lying on the platelet area of the right-hand partial platelet. In no member of the series, on the other hand, were voidites detected on the small area of platelet fringe contrast presented by the left-hand partial platelet. The voidites of both partial platelets have similar size distributions, the majority of individuals falling in the 3–7 nm range. Some voidites are clearly seen on the bounding dislocations of the right-hand partial platelet, and a few voidites appear to be up to 10 nm outside both the platelet area and the voidite-containing area between the dislocations. Five voidites can be seen on or very close to the platelet margins,

and five more well within the platelet area. The partial platelet seen on the left of the field in figure 23, plate 10, has very similar properties to that in the right of figure 22 just described. Again, the edges of the platelet appear slightly wavy, and some voidites are seen on either side outside the platelet area. About six voidites can be recognized on the platelet itself. Whereas the voidites on the platelets in figures 22 and 23 are not significantly different in size from those in their associated voidite sheets, this is not so in the cases of the voidites that can be detected on the platelet areas of the partial platelets shown in figures 9, 14 and 15. As stated at the conclusion of § 3*b*, there is a small population of fringing voidites outside the wavy peripheries of the platelets in figures 9, 14 and 15. The voidites that can be seen on these platelet areas occur with number density and sizes similar to the fringing voidites in the cases of figures 9 and 15. However, in the case of figure 14, examination of the micrograph shows that the voidites on the platelet are larger and more numerous than the fringing voidites. Their size is comparable with the voidites near the centre of the voidite sheet, their concentration being about a quarter of that at the sheet centre.

Voidite facet contrast

A contrast phenomenon observed in some individual voidite images deserves noting. It is illustrated in figure 24*a*, *b*, plate 10, in which part of the voidite sheet of a partial platelet is shown at high magnification. In this region, some bend contours are present and the original micrographs were developed to high contrast, both these factors providing conditions for the sensitive detection of evidence of strain contrast in the voidite images. A long through-focus series of ten exposures was taken that included some small tilts. A well-developed gradient of voidite size was present in the voidite sheet, the largest voidites being close to the boundary with the area of platelet fringe contrast on the left of the field. The chief feature of interest noticed is seen in the images of the largest voidites in figure 24*a* (i.e. those having edge lengths up to 8 nm). Those voidites whose depth from the specimen surface places them in the 'neutral' contrast condition (i.e. neither excess nor deficiency of blackness in the images of their volumes relative to the blackness of surrounding matrix image) nevertheless show quite distinctly in outline through contrast (dark on the print) from their {111} facets that contain the beam direction. See, for example, the voidites at (0.18, 0.53) and (0.29, 0.69). It is tempting to

Description of plate 9

Figure 21. Group of voidite-containing dislocation loops with some platelets. Direction [001] rotated 52° clockwise from horizontal. Field width is 0.5 μm (4723, original magnification $\times 1.5 \times 10^5$).

Figure 22. A pair of partial platelets; voidites lie on platelet area of right-hand partial platelet. Direction [001] rotated 10° clock-wise from horizontal. Field width is 1 μm, specimen thickness is 0.15 μm. (*a*) Near focus (E6952, original magnification $\times 5 \times 10^4$); (*b*) underfocused (E6957).

Description of plate 10

Figure 23. Partial platelet (left) with voidites on the platelet area, and a dislocation loop segment (upper right) containing many small voidites with diameters < 1 μm. Direction [001] rotated 5° anticlockwise from horizontal. Field width is 1 μm and specimen thickness is 0.25 μm (G6949, original magnification $\times 4 \times 10^4$).

Figure 24. Voidite facet contrast in focused images of voidites. Direction [001] is horizontal, field width is 200 nm, specimen thickness is 80 nm. (*a*) Near focus, some voidites show only facet contrast (N6985, original magnification $\times 8 \times 10^4$); (*b*) overfocused relative to (*a*) (N6984).

Figure 25. An H-feature exhibiting voidite chains. Direction [001] rotated about 40° clockwise from horizontal, field width 0.5 μm, specimen thickness 0.2 μm (4770, original magnification $\times 1.5 \times 10^5$).

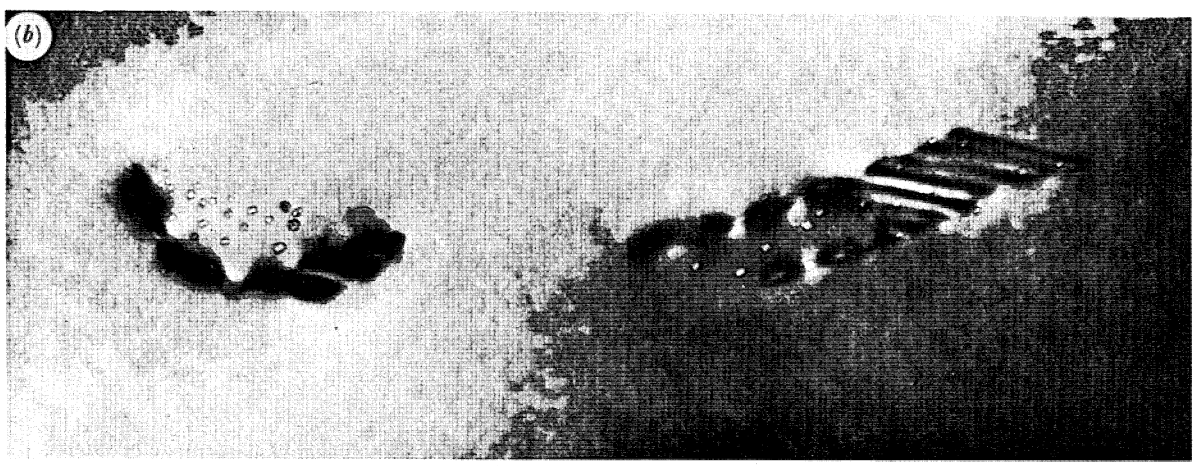

FIGURES 21 AND 22. For description see opposite.

(*Facing p.* 380)

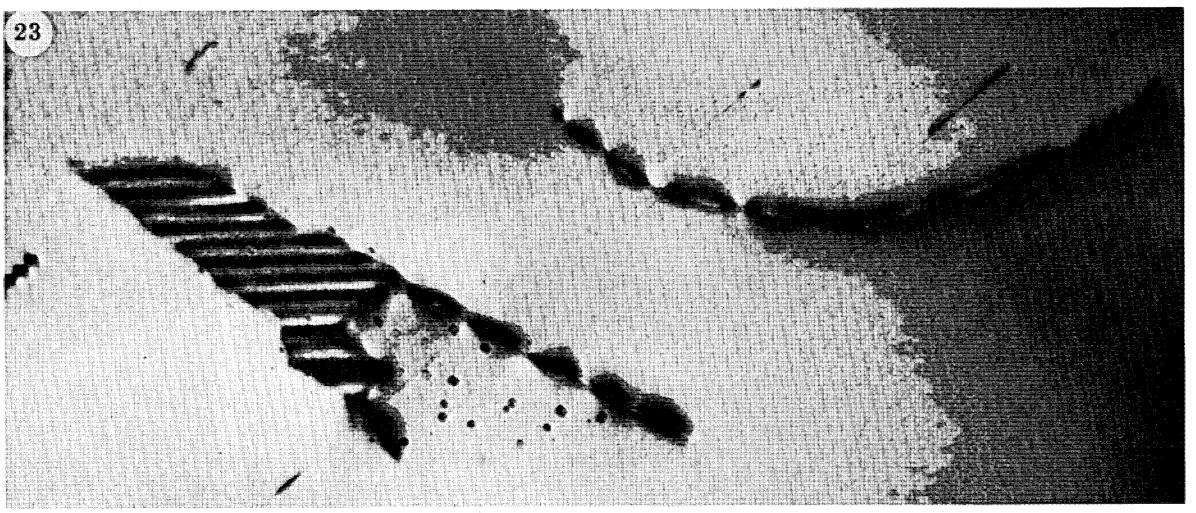

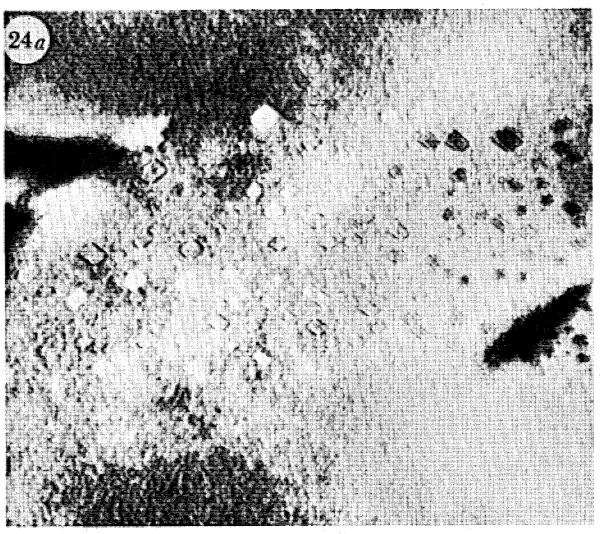

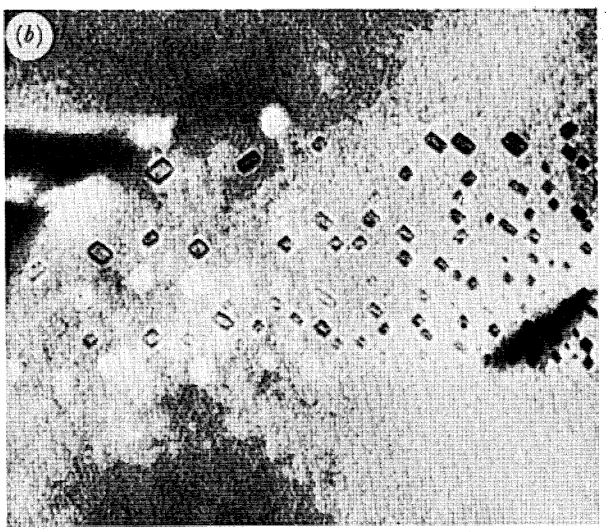

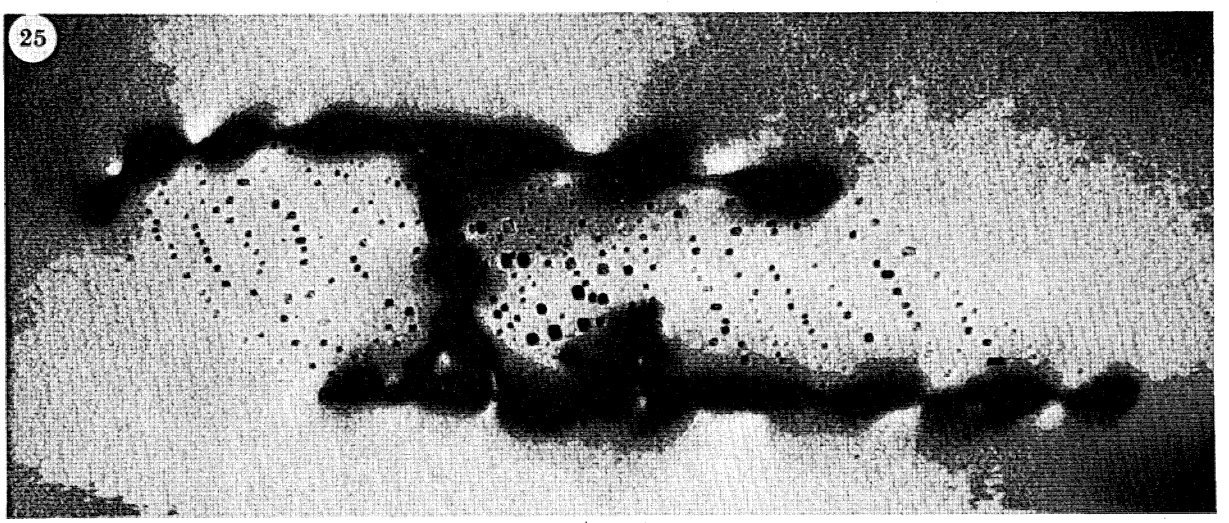

FIGURES 23–25. For description see p. 380.

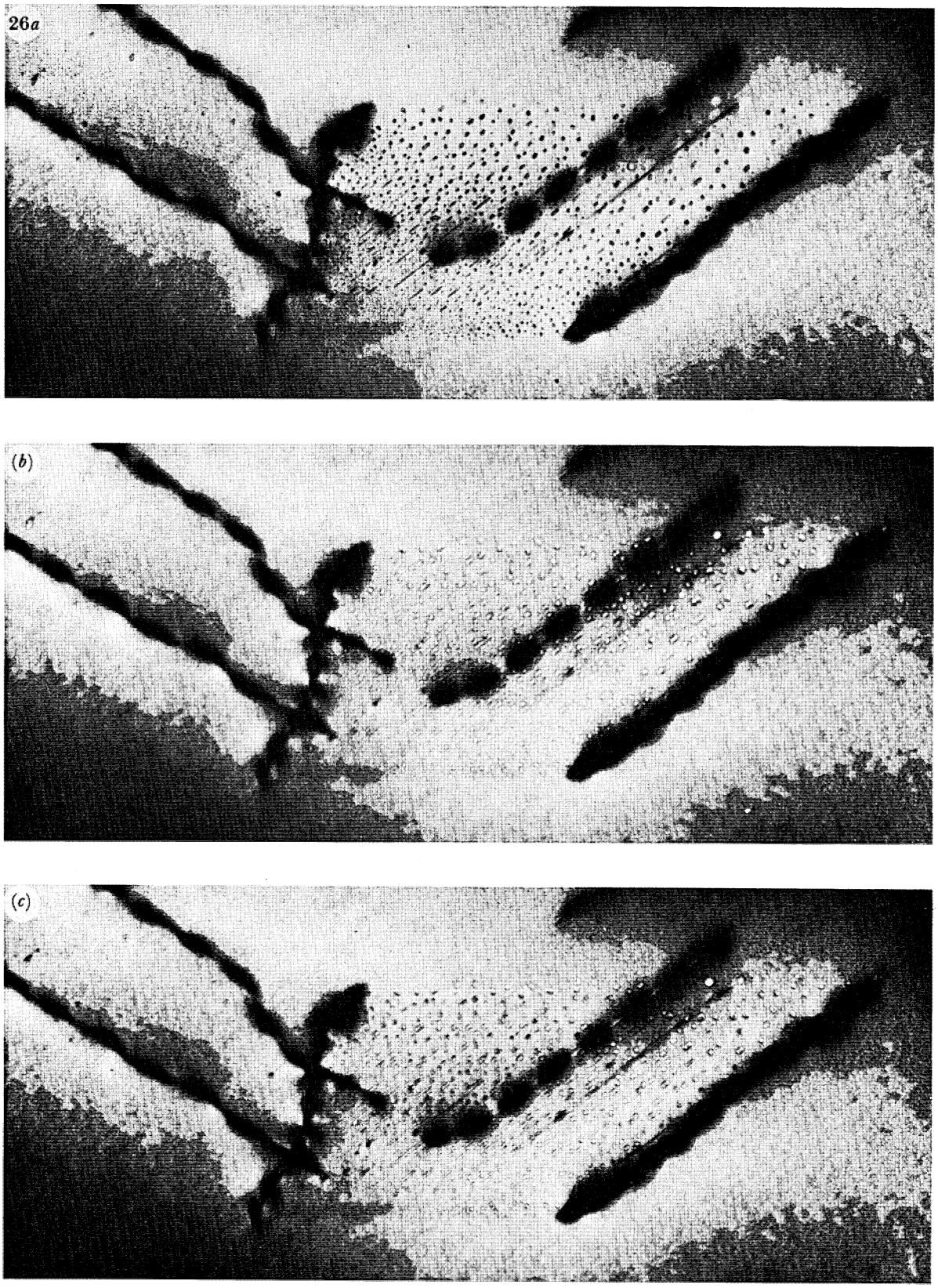

FIGURE 26. For description see overleaf.

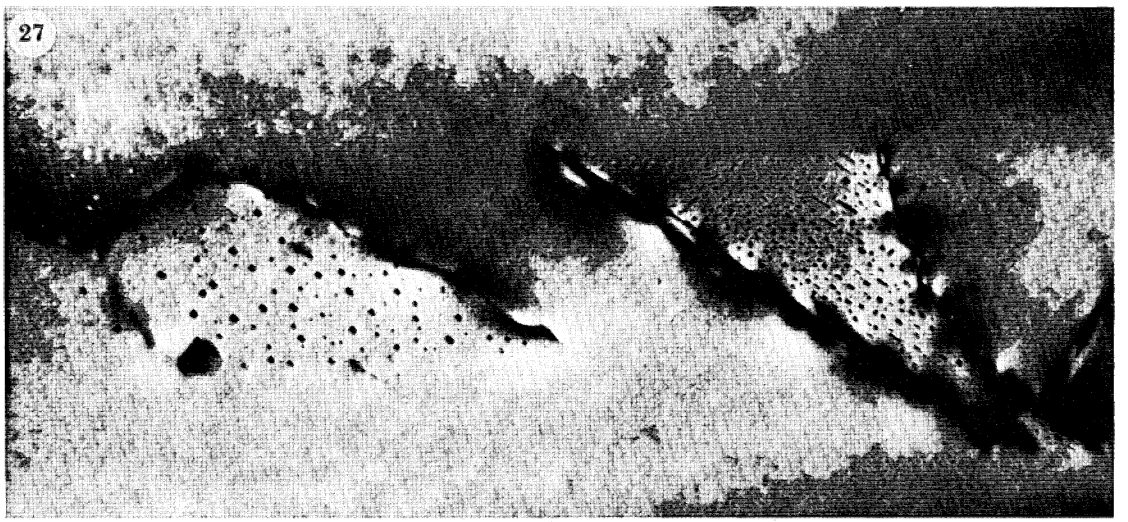

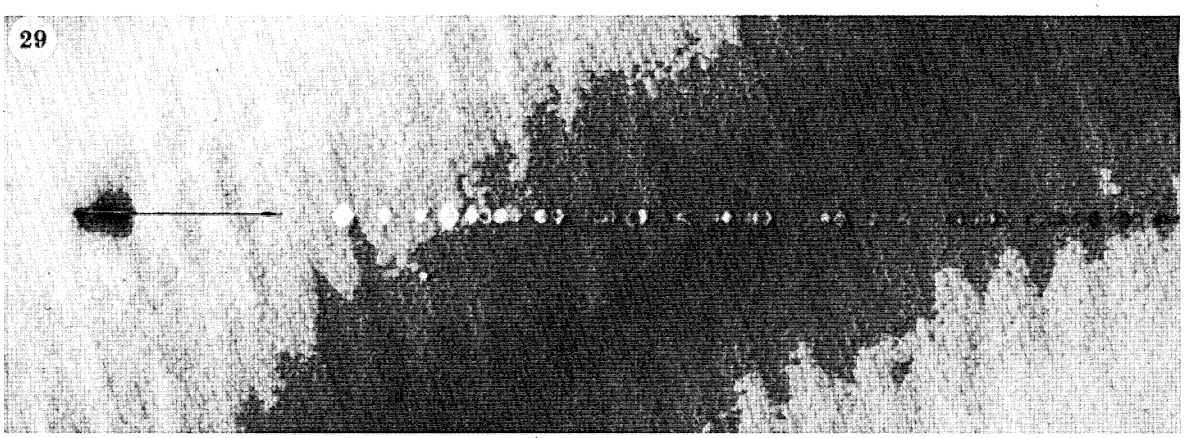

FIGURES 27–29. For description see opposite.

Description of plate 11

Figure 26. Voidite sheets lying between dislocations. The sheet in the field centre contains highly elongated voidites, linear features possibly exhibiting strain contrast, and evidence of residual fault-fringe contrast at its lower margin. The sheet in the upper left of the field contains many voidites with diameters below 1 nm. Direction [001] is horizontal. Field width is 1 μm, specimen thickness is 0.25 μm. The sequence (*a*), (*b*), (*c*) proceeds from near-optimum focus to increasing underfocus ((*a*), I6966; (*b*), I6967; (*c*), I6968, original magnification $\times 4 \times 10^4$).

Description of plate 12

Figure 27. Pair of voidite sheets. Evidence of residual fault surface contrast appears along the outcrop of the right-hand voidite sheet. Direction [001] is horizontal, field width is 0.9 μm (J6971, original magnification $\times 6 \times 10^4$).

Figure 28. Dislocation loops containing well-resolved voidites together with seas of small voidites of diameters < 1 μm. Some voidites appear outside loops. The loop in the lower central part of the field is not confined to a cube plane. Direction [001] is vertical, field width is $1\frac{1}{3}$ μm, specimen thickness about 0.19 μm (H6960, original magnification $\times 4 \times 10^4$).

Figure 29. Edge-on view of partial platelet parallel to (001): platelet contrast on left, voidite sheet in centre and right of field, with largest voidites near platelet boundary. Specimen DL4/B. Direction [001] is vertical in this and the following figures. Field width 0.4 μm (12044, original magnification $\times 1.5 \times 10^5$).

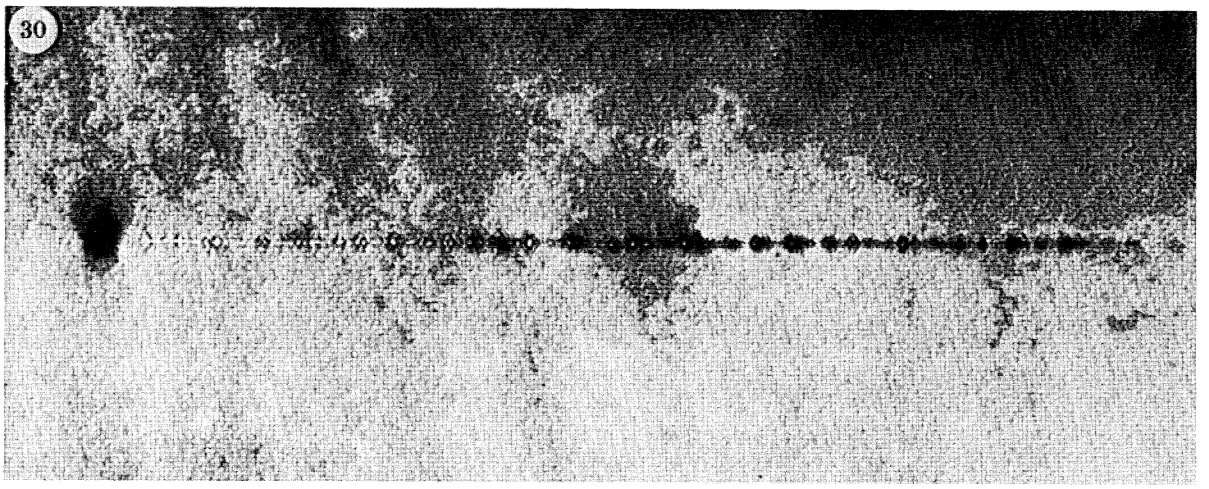

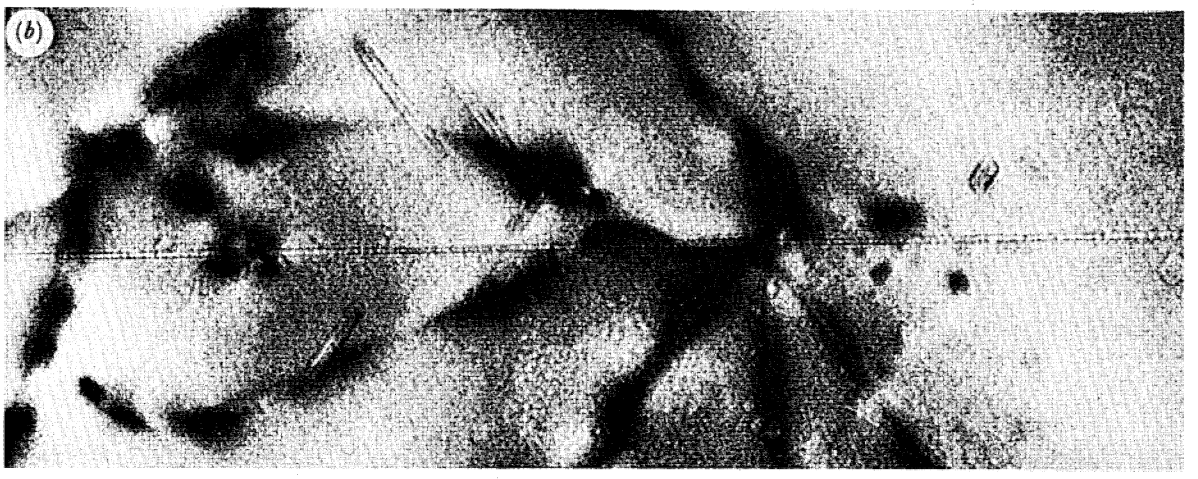

FIGURES 30 AND 31. For description see opposite.

Description of plate 13

Figure 30. Edge-on view of voidite sheet parallel to (001), terminated on left by a strong dislocation image. Many voidite diameters are below 1 nm in this projection. Specimen DL4/B. Field width 0.2 μm (11482, original magnification $\times 2 \times 10^5$).

Figure 31. Field including the middle segment of a voidite sheet parallel to (001) whose total image length parallel to $[\bar{1}10]$ is greater than 1.7 μm. Dislocations and stray voidites also present. (*a*) Field width 1 μm (7526, original magnification $\times 4 \times 10^4$); (*b*) enlargement of top left of (*a*) to show highly elongated voidites apparently attached to dislocations; field width 0.4 μm.

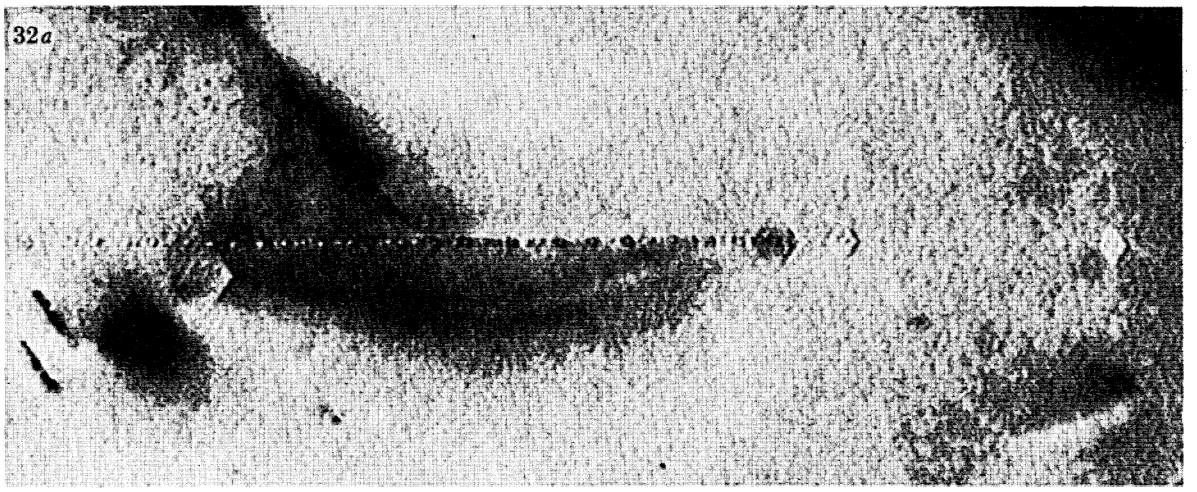

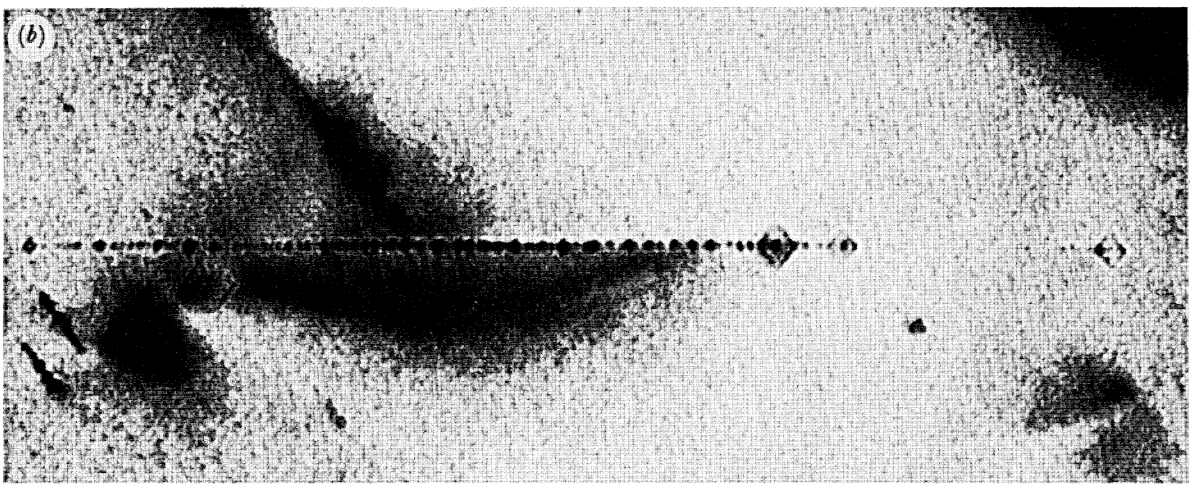

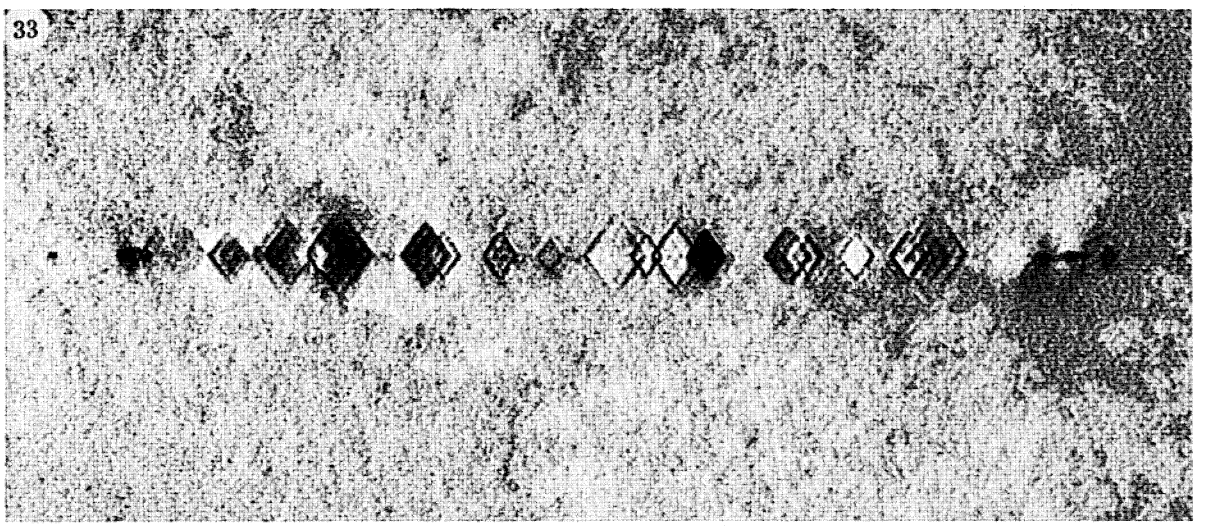

FIGURES 32 AND 33. For description see opposite.

attribute this contrast to a difference in structure between voidite facet surface layer and the matrix, but it is probably an electron-optical effect.

Possible instances of strain contrast

If there were a high internal pressure within voidites, then strain-contrast lobes in the image of the matrix surrounding them might be observable similar to those associated with radiation-produced faceted voids containing helium at high pressure that have been studied in metals (Cochrane & Goodhew 1983). Despite the ranges of defocus and of tilts away from exact [110] zone axis diffraction conditions (either deliberate or due to specimen bends) employed in recording voidite images, no evidence of strain contrast lobes has been recognized. As an example of lack of detectable strain contrast attributable to internal pressure within voidites, we cite the absence of lobes attached to the voidite images in figure 24*a*, discussed above. The single possible strain-contrast manifestation associated with voidites we have encountered is of quite different nature and consists of the fine straight lines (dark on the prints) parallel to ⟨110⟩ directions in voidite sheets, which we have mentioned above in §3*c* with regard to figure 17. The most strongly visible linear feature of this type discovered so far lies in the voidite sheet shown in figure 26, plate 11, running down leftwards from (0.78, 0.77) at the top edge of the voidite sheet to disappear at about (0.55, 0.35). A similar and parallel feature apparently runs close to the dislocation that forms the right-hand boundary of the voidite sheet, lying about 15 nm from the axis of this dislocation, but being so strongly masked by the strong diffraction contrast of the dislocation that it can only be seen on the prints in the region near (0.67, 0.35). Nine images were recorded in this through-focus series. Close examination of the series shows that the two linear features whose location has been given are just the most strongly visible of several similarly oriented lines in this voidite sheet. The line most strongly visible behaves as if it had a fine tube along most of its length, the tube diameter being between 1 and 2 nm, about half that of elongated voidites in the vicinity. Throughout the through-focal series there persists a qualitative difference between the images of these linear features and the pure phase-contrast images of voidites usually observed. The linear features may be lines of impurity decoration marking previous loci of dislocations.

Voidite chains

One noteworthy type of non-random distribution of the individuals in voidite sheets has been encountered in some sheets contained between dislocation dipoles: the voidites tend to be aligned in chains bridging the dipole so that the combination of dipole and voidites takes on the appearance of a ladder with very irregular rungs. Such appearances need to be questioned, however, because the existence of a series of distances from the specimen surface at which voidite contrast is a minimum will tend to impose a ladder-like pattern on a uniform distribution of

---

DESCRIPTION OF PLATE 14

FIGURE 32. Voidite sheet parallel to (001) showing a large range in size and population density of voidites. Field width is 0.2 μm. Total length of voidite sheet image is 0.4 μm. (*a*) Focused to bring out contrast from a large voidite not centred on the sheet, at (0.17, 0.43) (D6947, original magnification $\times 8 \times 10^4$). (*b*) Focused for strong contrast from centre and left-hand segments of voidite sheet in the field (D6949, original magnification $\times 1 \times 10^5$).

FIGURE 33. Voidite sheet parallel to (001) probably contained between a dislocation dipole elongated along [110]. Field width is 0.1 μm.

voidites, the rungs being equispaced and parallel to [001]. The mark of a genuine voidite alignment is its visibility across depth contours. This phenomenon is shown well in figure 25, plate 10, and is arguably also manifested in the dipole loop above the centre of the field of figure 21, plate 9. In the voidite sheets of the H-feature shown in figure 25, the alignments are best seen away from the region of large voidites in the centre of the feature. In the areas of well-developed alignments, the voidite chains run in wavy lines across the dipole, and individual chains can be followed through the cycle of depth-dependent contrast. The chains resemble lines of flotsam on a beach. Some chains appear to split. We regard as significant the observation that all voidite chains recognized have been found in the planes of dislocation dipole loops: no chain has been seen in the voidite sheets of partial platelets.

Bimodal distributions of voidite size

We turn now to an aspect of voidite size variation different from that discussed earlier in §3*b*. The term bimodal is adopted as a brief designation for the cases when (*a*) there appear to be two peaks in the voidite size distribution in a given voidite sheet, or (*b*) there is a significant difference in mean voidite sizes in different sheets that lie close together in the specimen. The important manifestation of (*a*) is when the population of well-resolved voidites (with sizes ranging from 3 nm upwards, say) appears superimposed on a 'sea' of small voidites on the limits of resolution, having sizes under 1 nm. The existence of a voidite sea, detected or suspected, sets serious difficulties in the path of measurement of the integrated volume of a voidite sheet. Sometimes the amount of defocus needed to make the voidite sea visible would render any estimate of the volumes of individuals in the sea totally unreliable. Voidite seas are most easily detected by examination of high-contrast prints, but their detectability is usually determined by granularity in the original micrograph image. However, in the majority of the voidite sheets examined we have not detected a voidite sea, and in most of these cases we are reasonably confident that no significant fraction of the voidite population lies in the size range below 1 nm. No voidite sea has been detected in any of the sheets of well-resolved voidites illustrated in figures 2–18, although the small fringing voidites lying outside the platelet peripheries of some of the partial platelets have diameters down to 1 nm and perhaps less, and thus lie in the size range found in seas elsewhere. In figure 19 there is a voidite sea on the right hand of the bridging dislocation of the H-feature: typical diameters of individuals in this sea are estimated to be about 0.5 nm, a tenth that of the more prominent larger voidites in this region. No voidite sea is detectable in any part of the other H-feature, in figure 25. Voidite seas appear in the loops shown in figure 28, plate 12. The case (*b*) is well exemplified in figure 23. The segment of voidite sheet in the upper right of the field contains only small voidites, few having diameters greater than 1 nm. By contrast, the voidites in the sheet belonging to the partial platelet in the lower left of the field have sizes mainly in the 5–7 nm range, and no sea of small voidites surrounding them is detected. Another example of case (*b*) appears in figure 26, in which one may compare the voidite sheet between the pair of dislocations that enter the field from the top-left corner with the sheet that occupies the field centre. The edge-on views of voidite sheets described below (§3*e*) offer further evidence regarding very small voidites. The problem of detection of voidite seas is closely linked with the question of 'residual fault fringes' considered next.

Residual fault-surface contrast

Appearances of contrast of fault-fringe type in areas covered by voidite sheets will now be pointed out, and the genuineness of evidence for a residual fault surface remaining after

conversion of platelets to voidite sheets will be assessed. When voidite sheets on (100) or (010) are photographed at low magnification and resolution, the individual voidite images merge to produce an overall pattern simulating weak fault-surface fringes. The weak fringes on the image of the voidite sheet at (0.28, 0.8) in figure 8 are an example. This observation is perfectly understandable in view of the periodic variation of contrast with depth of individual voidites under the diffraction conditions usually pertaining. Figure 3*b* represents a case where magnification and resolution are sufficient to resolve the majority of, if not all, voidites. Close examination of the image suggests that the fringes appearing on the voidite sheet when the print is viewed from a distance are fully accounted for by the depth-dependent contrast variation of individual voidite images. Next, consider more problematic micrographs. The difference between figures 10*a* and 10*b* arises from focus change plus a small tilt: figure 10*a* is nearer optimum focus. Comparison of the two figures, concentrating especially on the fringes appearing on the upper-right part of the voidite sheet, does suggest that a fringe-generating factor is present in addition to the contrast periodicity of the voidite images, but not with certainty. In the case of figure 13, the area of interest is in the upper-left part of the voidite sheet, around (0.3, 0.7). For the observed fringe contrast to be simply attributable to voidites one needs to invoke the presence of a rather dense voidite sea, and such presence is deemed unlikely in view of lack of evidence for it elsewhere in this voidite sheet. In the case of the voidite sheet lying between the pair of dislocations in the right-hand half of figure 27, plate 12, the diffraction conditions are such as to generate an overall deficiency of blackness in the image of the voidite-containing cube plane, with only a weak depth-dependent modulation. Looking at the upper-middle part of the voidite sheet, close to its outcrop at the specimen surface, one perceives that all resolved voidites give dark images. Unresolved voidites, if present, should give contrast of similar sign. No other explanation for the background deficiency along the middle part of the voidite sheet outcrop can be suggested other than fault-surface contrast generated on this cube plane. Further evidence favouring the reality of fault-surface contrast comes from the through-focal series of which figure 26*a–c* is representative. The features to note particularly are the dark fringes in the lower left of the principal voidite sheet in the field. The lowest fringe shows strongest contrast in the vicinity of the point (0.38, 0.17), the next fringe above is much weaker. These fringes undergo no change in strength or sign of contrast throughout the through-focal series during which the voidite images change from dark to light (on prints). This series provides our most convincing evidence for the verity of fault-surface contrast generation at the planes in which voidite sheets lie. Well-visible fringes are seen in the central loop and upper right-hand loop segment in figure 28, but because these loops contain a dense population of barely resolved voidites, as previously mentioned, this observation of fringes is not deemed to be of much weight.

(*e*) *Edge-on images of voidite sheets*

The remaining micrographs (figure 29, plate 12, to figure 33, plate 14) all show images of voidite sheets lying in (001). They were taken in regions where the specimen was thinner than in the localities chosen for micrography of partial platelets and voidite sheets lying on cube planes inclined at 45° to the electron beam, but the specimen was always too thick for lattice resolution to be achieved. The first two edge-on views, figures 29 and 30, were obtained from specimen DL4/B, and the rippled appearance due to imperfectly prepared specimen surfaces is evident. Figure 29 is a partial platelet: the strong, sharply defined line image, 70 nm long, on the left is characteristic of normal platelets viewed edge-on. Platelets and voidite sheets are readily distinguishable in high-resolution, edge-on images. The partial dislocation that bounds

the platelet on its left edge produces strong diffraction contrast. The weakness of dislocation contrast at the right-hand edge of the platelet is surprising. Perhaps a combination of diffraction and surface-relaxation conditions enhances the difference in contrast between the two bounding dislocations. In addition, the right-hand platelet boundary may be less straight and more steeply inclined to the electron beam than the boundary on the left, but this cannot be easily ascertained from an edge-on view. As in some of the partial platelets described in §3*b*, the largest voidites in the voidite sheet lie close to the platelet boundary. No contrast from the voidite plane itself is detectable: the gaps between the voidites appear entirely contrast-free. The right-hand edge of the voidite sheet lies beyond the edge of the field of the original micrograph.

Much smaller voidites are seen in figure 30, plate 13. With this voidite sheet some defocus is needed to make the voidite images stand out well above the background granularity. The size of the smallest voidites, whose images merge together in projection, is estimated to be less than 0.5 nm. It would appear that this voidite population resembles a voidite sea similar to those observed in figures 23 and 28. This figure contains the entire length of edge-on image that appears on the original micrograph. A very strong dislocation image terminates the voidite sheet on the left, but there is no dislocation image on the right. By sighting along the image of the voidite sheet, or by setting a straight edge against it, one perceives a slight waviness in the sheet, particularly evident in the segment within about 50 nm from the left-hand bounding dislocation. This unstraightness cannot be attributed to passage of dislocations through the sheet: that would give rise to offsets rather than to undulations. The peak-to-peak waviness is not greater than 0.5 nm, and is similar in magnitude to the diameters of the smallest voidites in the sheet. Another example of apparent voidite sheet waviness is shown in figure 32, plate 14. Some other cases of waviness detectable in edge-on images consist of a single oscillation seen in sheets whose images span the whole micrographic field, and these can be accounted for by a slight S-distortion in the electron-imaging system.

The next micrographs, figures 31, plate 13, and 32, plate 14, demonstrate the difficulty of assessing the total volume of voidites associated with a particular voidite sheet. Figure 31*a* shows the middle segment of a long edge-on image of a sheet of very small voidites. The sheet appears at height 0.75 in the figure. All voidites lying exactly in the sheet are probably smaller than 1 nm in diameter, and some defocus is needed to expand their images to provide a feature recognizable in reproduced micrographs. Another sheet of mainly very small voidites is inclined at 45° to the electron beam, and runs down from the region (0.25, 0.75) to the bottom of the figure: it is not easily recognizable. Part of a local tangle of dislocations is included in this field. Noteworthy is the number of relatively large stray voidites, which can be seen above and below the edge-on voidite sheet. Many of these individual strays have volumes two to three orders of magnitude greater than those of the small voidites in the sheet. Some strays can be detected apparently just touching the sheet, others are well detached from both sheet and dislocations. Figure 31*b* is an enlargement of the top-left corner of figure 31*a*: the voidite sheet on (001) now lies across the field at mid-height. Some equiaxed or slightly elongated strays can be seen distinctly in the right-hand half of the figure. Remarkable are the highly elongated voidites in the left half of the field. They do not lie in a voidite sheet, but appear to be attached to dislocations.

Figure 32*a*, *b* also illustrates a voidite sheet in which many of the voidites are so small that one needs to examine a through-focal series of micrographs to be reasonably certain that no voidite is escaping detection anywhere along the trace of the voidite-containing plane. About

half the total length of the voidite sheet image is contained in these figures. Beyond the left-hand margin, the sheets ends without any apparent dislocation contrast. On the right of the field the sheet is joined by a dislocation that apparently lies in it for the remainder of its length. The following features are illustrated by this pair of micrographs. First, there is a very non-uniform density of voidites in this sheet. Secondly, the voidite size distribution termed bimodal, discussed in §3*d*, is apparent here: there appear to be a few relatively large voidites dispersed among a sea of small voidites in the sheet. Thirdly, there is seen at (0.17, 0.43) a large voidite, not centred on the sheet, but possibly attached to one of the dislocations that show strong contrast in this region. This single voidite has a volume at least three orders of magnitude greater than that of the smaller individuals in the sheet.

The last example of an edge-on view of a voidite sheet, figure 33, plate 14, is a high-magnification image containing well-resolved individual voidites. This sheet has already been exhibited in the review by Bursill (1983), but it merits more description. Features in the plane of the voidite sheet that it is desired to point out will be identified simply by giving their fractional x-coordinate in the field reproduced. Dislocation contrast can be recognized at 0.11 and 0.89, and it is likely that this voidite sheet lies between a pair of dislocations parallel to [110] pasing through these points. On this interpretation, the very small object at 0.04 and the larger, recognizably lozenge-shaped object at 0.92 are small voidites outside the dislocation dipole. All well-resolved voidite images are rhombi in outline. Thus any elongation, if present, must be perpendicular to the plane of the specimen. No waviness of this voidite sheet is detectable. Indeed, on the evidence of these symmetrical voidite images, it would not be unreasonable to infer that the geometrical centres of all the voidites lie within a distance range of one cell edge, a_0, from a geometrical plane parallel to (001). The voidite images demonstrate all phases of the cycle of depth-dependent contrast. They also show contrast, dark on prints, from their facets parallel to the electron beam, similar to that discussed in connection with figure 24, plate 10. In addition, they show within their parallelogram outlines the trellis-like Fresnel interference pattern discussed by Hutchison & Bursill (1983) in connection with a large equiaxed image of a voidite.† There is no evidence of corner truncation of voidites. In some of the gaps between well-resolved voidite images, especially that at 0.32, contrast in the voidite plane is seen. In the case cited it appears to be caused by a few very small voidites. In the largest gap, at 0.63, the voidite plane is completely free from contrast.

(*f*) *Summary of representative micrographs of voidite phenomena*

The aim of this tabulation of micrographs is to facilitate the quick location of figures that exhibit some particular property of voidites or voidite populations. The dozen properties selected for inclusion in table 1 do not include generic characteristics such as {111} facets on voidites or voidite-filled dislocation dipoles etc., but rather, certain specific features that, occurring with greater or lesser frequency, do in aggregate illustrate elements of the diversity and complexity in the full pattern of voidite behaviour. The selection has been restricted to features that appear in two or more micrographs included in this paper. The namings of features in table 1 are mostly self-explanatory; for elaboration upon them earlier paragraphs may be consulted. A cross entered in the table means an occurrence that should be at least clearly recognizable on the prints; underlining indicates noteworthy examples.

† These patterns have now been re-interpreted as overlap moiré interference fringes between the diamond matrix and a crystalline phase filling the voidites (Barry 1986; Hirsch *et al.* 1986*a*).

TABLE 1. REPRESENTATIVE MICROGRAPHS OF VOIDITE PHENOMENA

plate no.	1		2		3	4		5			6		7			8		9		10			11	12			13	14		
figure no.	2	3	4	5	8	9	10	11	12	13	14	15	16	17	18	19	20	21	22	23	24	25	26	27	28	29	30	31	32	33
property																														
highly elongated voidites	·	x	·	·	·	·	·	·	·	x	·	·	·	·	·	x	·	·	·	·	·	·	x	·	·	·	·	x	·	·
radiating patterns of voidites	·	·	·	·	·	x	·	·	·	x	x	·	·	·	·	·	·	·	·	·	·	·	x	x	·	·	·	·	·	·
annular partial platelets	x	x	x	x	·	·	·	x	·	x	x	x	·	·	·	·	·	·	x	·	·	·	·	·	·	·	·	·	·	·
lobate platelet peripheries	x	·	·	·	·	x	x	x	x	x	x	x	·	·	·	·	·	·	·	·	·	·	·	·	·	·	·	·	·	·
fringing voidites	·	·	·	·	·	x	·	x	x	·	x	x	·	·	·	·	·	·	·	·	·	·	·	·	·	·	·	·	·	·
voidites on platelets	·	·	·	·	·	x	·	x	x	·	x	x	x	·	·	·	·	·	x	x	·	·	·	·	·	·	·	·	·	·
bimodal size distribution of voidites	·	·	·	·	·	·	·	·	·	·	·	·	·	·	·	x	·	·	·	x	·	·	x	·	x	·	·	·	x	·
voidite diameters < 1 nm	·	·	·	·	·	·	·	·	·	·	·	·	·	·	·	x	·	·	·	x	·	·	·	·	x	·	x	x	x	x
residual fault fringes (strong evidence)	·	·	·	·	·	·	x	·	·	x	·	·	·	·	·	·	·	·	·	·	·	·	x	x	·	·	·	·	·	·
dislocations lying in platelets and voidite sheets	·	·	·	·	·	·	·	·	x	x	x	x	x	x	·	·	·	·	·	·	·	·	·	·	·	·	·	x	·	·
voidites decorating dislocations	·	·	·	·	·	·	·	·	·	·	·	·	·	·	x	x	x	x	x	·	·	·	·	·	x	·	·	x	·	·
voidite chains	·	·	·	·	·	·	·	·	·	·	·	·	·	·	·	·	·	x	·	·	·	x	·	·	·	·	·	·	·	·

4. DISCUSSION

(a) *The environment of voidites*

(i) *Platelet and voidite-sheet areas*

We will now look at populations of platelets and voidite sheets, and search for clues concerning the processes that lead to formation of voidites. As a first step in examining the environment of voidites we will consider how much nitrogen might be aggregated in existing or erstwhile platelets in our specimens, and compare this with an estimated or plausible value for total nitrogen impurity concentration. For specimen A4 we have an abundance of electron microscopic images from which measures of total platelet area per unit volume of specimen can be derived with greater reliability than previously achieved. Unfortunately, the specimen was too inhomogeneous to give meaningful infrared absorption coefficients, and no infrared absorption measurement had been attempted on it before thinning for transmission electron microscopy. In specimen DL4, on the other hand, the optical homogeneity was unusually high, as judged from cathodoluminescence topography (which can reveal inhomogeneities on a micrometre scale). However, in this specimen only the dislocation loops bounding voidite sheets were present in sufficient abundance to provide data of any statistical worth concerning platelet areas: the partial platelets described in §3 represented only a fraction of erstwhile total platelet

area. Compared with the statistical uncertainties arising from the low population density of defects on {100}, the errors in estimating original platelet area from the present areas of dislocation loops surrounding voidite sheets could be neglected, because in the fields analysed there was no evidence for significant movement of dislocations away from the loci of the peripheries of the original platelets.

To derive the concentration of precipitated nitrogen from platelet area, one must choose a platelet structure model. Without embarking on further discussion of this topic, one can assert certain bounds to the nitrogen content of platelets that are consistent with all lattice-imaging evidence. First, the platelet structure has a thickness not greater than one 'abnormal' diamond cell whose height is between $1.35a_0$ and $1.4a_0$. Secondly, the structure contains neither marked voids nor excesses of electron density compared with normal diamond. With these constraints, it does not seem feasible to fit in more than the four nitrogen atoms per area, a_0^2, of platelet prescribed in the Lang (1964) model, and it is deemed unlikely that a structure of near-normal density will contain less than the two nitrogen atoms per area, a_0^2, proposed by Humble *et al.* (1985*b*). On these bases, the atomic fractions of nitrogen in diamond represented by a total platelet area of 1 μm^2 in a volume of 1 μm^3 come out as 1.78×10^{-4} and 0.89×10^{-4}, respectively. Such uncertainty within a factor of two is not greatly out of line with the cumulative uncertainty in area per unit volume measurements, even with favourable specimens and good electron microscopic technique.

Table 2 presents platelet area measurements and statistics derived therefrom. All micrographs except 6982 were taken with the Philips EM 400 microscope operated at 120 kV. The field of micrograph 8069 lies in the same growth zone as figure 2, and its features were displayed on the cover of the *Bulletin of the Institute of Physics, London*, volume 35 (February 1984). The field called 'loops 1' was used for determinations of Burgers vectors of loop dislocations. The micrographs listed are all [110] zone axis bright-field images. Specimen thicknesses were determined from the images of defects of known orientation cut by both top and bottom specimen surfaces. Mean thickness estimates, obtained from such measurements on films or prints, have a precision of about $\pm 5\%$ in the case of specimens A4 and DL4/B, but only about $\pm 10\%$ in the region of DL4/A in figure 8. However, the stated magnifications of micrographs 8071, 8069 and 2364 may be in error by up to 5%. If the true magnification were $x\%$ greater than that stated, then the true figure for total defect area per unit volume would also be $x\%$ greater than the stated value. Most of the platelet area in the micrographs of specimen A4 is contained in highly elongated platelet 'laths'. In these micrographs of moderately low magnification there is an uncertainty of about 10% in lath width measurement. Clearly, only areas of defects lying on (100) and (010) can be measured. The sum of such areas is multiplied by $\frac{3}{2}$ to obtain the total defect area on {100} in the specimen volume. The final column of table 2 has used the Lang (1964) platelet model to give an upper estimate of the number of nitrogen atoms (expressed as a fraction of all atoms in the crystal) that could have been precipitated in platelets. The fields of micrographs 8069 and 8071 represent a zone of specimen A4 poorer in platelet area per unit volume than most of the specimen area thin enough for transmission electron microscopy, perhaps by a factor of three or four. One might therefore guess that the average concentration of platelet nitrogen in this inhomogeneous crystal was about $400/10^6$. Now it was pointed out by Davies (1970) that, in diamonds showing predominantly the A features in the infrared absorption spectrum, the linear relation established between the strength of this absorption and assayed nitrogen content was, within experimental error, independent

TABLE 2. TOTAL PLATELET PLUS VOIDITE SHEET AREAS, AND ESTIMATED PRECIPITATED NITROGEN CONTENT

specimen	micrograph no., original magnification	field	specimen area analysed / μm²	mean specimen thickness / μm	number of features measured: platelets	number of features measured: partial platelets	number of features measured: voidite sheets	total defect area on {100} / μm²	defect area per unit volume / μm² μm⁻³	maximum precipitated nitrogen / atoms per 10⁶ atoms
A4	8071 ×10500	figure 2	14	0.30	89	1	11	3.0	0.72	128
A4	8069 ×10500	*Bull. Inst. Phys., Lond.*	8.4	0.31	93	0	7	2.0	0.76	135
DL4/A	6982 ×10000	figure 8	14	0.20	0	0	16	0.84	0.30	53
DL4/B	2364 ×28000	loops 1	8.8	0.28	0	0	17	0.69	0.28	50

of the strength of the 'platelet' infrared absorption peak at 7.3 μm, and it therefore followed that only a small fraction (less than 10%) of the total nitrogen content can reside in the platelets. On the other hand, for diamonds showing predominantly the B infrared absorption spectrum there is a dearth of data to indicate likely ratios between 'platelet' nitrogen and B-defect nitrogen concentrations. If specimen A4 had verged towards the type IaA limit in A defect:B defect ratio, then one would conclude that it had an unusually high nitrogen content, of order $\frac{1}{2}$% atomic. But it is believed that the regions of A4 investigated had relatively low A defect:B defect ratios, and it follows that there is no reason to deem as exceptionally high its content of nitrogen precipitated in platelet form derived above. Regarding specimen DL4, the closeness of the two measurements can be taken as fortuitous, considering the small totals of defects contained in the fields analysed. For specimen A4, the mean of the two defect area per unit volume values should be correct to ±25%, and for specimen DL4 to about ±45%. Recalling the figure stated in §3*a* for nitrogen content in B-defect form within DL4 (which is a representative of the type IaB class of diamonds), namely, 400 N atoms per 10^6 atoms in the crystal, one finds the ratio of present B-defect nitrogen content to erstwhile platelet nitrogen content to be 8:1. Since this determination is unique, no counter-example bids for discussion.

(ii) *Numbers and dimensions of platelets and dislocations loops*

Figures 2 and 4 represent regions in specimen A4 where platelets are sufficiently large and sparse for the presence of abnormal defects to be easily detected. An analysis of the defect populations in some similar fields will now be described. Matters considered include the range of micrographic data available, the types of defect searched for particularly, and the conclusions drawn from the surveys. The counting of defects was performed on [110] zone axis images, magnification ×10500, taken in the Philips EM 400 operated at 120 kV. Most of the 44 micrographs available were of this type. One region investigated, called region X (not illustrated here), was chosen for its freedom from micrometre-scale zonal variations in defect size and density, together with its possession of a substantial area (*ca.* 200 μm^2) of uniform thickness of 0.35 μm. Counts of defects were also performed in two zones of width 3 μm, along strips of length *ca.* 60 μm (called Y and Z), that ran between the fields of figures 2 and 4. The strip Y was well defined either side by narrow zones *ca.* 1 μm thick having a very low platelet density. Zone Y extends into the bottom-left part of figure 4. An extension of zone Z is represented in the upper right-hand of figure 4. The specimen thickness in zones Y and Z ranged from 0.34 to 0.49 μm.

Measurements and counts of defects are recorded in table 3. The former are subject to uncertainties due to possible error in electron microscope magnification similar to those noted for data in table 2. Regarding normal platelets, the remarkable feature is the clear division between laths and roughly equiaxed platelets. In region X, the great majority of non-lath shapes were nearly circular. For brevity, the classification 'rounds' is adopted for all non-lath-like shapes. In zones Y and Z, a frequent characteristic of non-laths, especially the larger ones, is to be partly bounded by a straight edge parallel to a ⟨110⟩ direction. In some cases the platelet shape is describable as a wide lath with a protuberance on one side. The platelet at (0.62, 0.57) in figure 4 is one such. Extreme developments of the 'lath with protuberance' shape were exhibited by some of the giant platelets observed by Woods (Woods 1976; Lang 1979). If platelets had the zig-zag structure proposed by Hutchison *et al.* (1982), then the preferential extension in only one of the two ⟨110⟩ directions in the cube plane would not be surprising,

TABLE 3. DEFECT TYPES AND INTERACTIONS IN SPECIMEN A4

	feature	region X	zone Y	zone Z
(1)	area examined/μm^2	370	169	166
(2)	volume examined/μm^3	120	68	67
(3)	defects per unit volume/μm^{-3}	26	30	23
	normal platelets			
(4)	laths	1529	1054	702
(5)	rounds	458	162	188
(6)	total laths + rounds	1987	1216	890
(7)	ratio, rounds: laths	0.30	0.15	0.27
(8)	typical round diam./μm	0.20	0.21	0.28
(9)	typical lath length/μm	0.6	0.7	0.7
(10)	typical lath width/μm	0.07	0.07	0.07
	abnormal defects			
(11)	loop + loop	31	32	23
(12)	loop + platelet	23	26	9
(13)	loop + defect on (001)	32	54	48
(14)	loop fraction	6	26	64
(15)	partial platelet	4	3	5
(16)	entire, isolated loop	2	0	0
(17)	total abnormal defects	98	141	149
(18)	ratio, abnormal: normal defects	0.05	0.12	0.17
(19)	ratio, partial platelets: 10^3 normal platelets	2	2.5	5.6

but it would leave the considerable minority of round shapes to be accounted for. Rounds are not laths that have failed to grow, for average areas of laths and rounds are similar. In region X, one gains the impression that there exists some slight tendency for rounds to occur in clusters of, say, three or four individuals in a specimen area of 1 μm^2 or less. In the counting of laths and rounds, defects are included that it is judged have not less than half their area captured in the specimen foil. This judgment is straightforward in the case of rounds. For example, one would include all three rounds in the vicinity of (0.7, 0.3) in figure 2, but exclude that at (0.8, 0.8). The decision whether or not to include a lath is more subjective, depending upon one's conception of the distribution of lath lengths and its mean. These parameters are hard to assess. However, in specimens where entire laths and laths truncated by both top and bottom specimen surfaces occur with roughly equal frequency, one can conclude that the average lath length on (100) or (010) is about twice the specimen thickness, assuming that the length distribution is not very skew. However, the evidence does not preclude a tail in the distribution extending towards lengths much longer than the mean: exceptionally long laths would be indistinguishable among other laths truncated by both surfaces.

Turning to the classification of abnormal defects in table 3, the features numbered 11 and 12 refer to defects on (100) or (010). We believe that the great majority of these involve interactions between defects lying on different cube planes, but the single [110] zone axis view provides no clue to this relation in the majority of cases. However, when the configuration is a combination of two long dipole loops, or a long loop and a platelet lath, direct geometrical evidence can be obtained from the overall dimensions of the image of the combination in two situations, which we refer to as cases (*a*) and (*b*). In case (*a*), the two defects have similar long axes in projection in the [110] view, i.e. the axes of both defects are parallel to $[1\bar{1}2]$ or to $[\bar{1}12]$. Then, if their combined length projected on (001) exceeds the known local specimen thickness, the two defects lie on non-parallel cube planes. In case (*b*), the image of one defect has $[1\bar{1}2]$

as long axis, and the other has $[\bar{1}12]$. In this case, if their combined length projected on $(1\bar{1}0)$ exceeds tan $54\frac{3}{4}°$ times the specimen thickness the two defects lie on the same cube plane. Search in zones Y and Z found six certain or almost certain examples of case (*a*), and none of case (*b*), although three loops having the 'boomerang' shape corresponding to the geometry of case (*b*) did appear very likely to have been derived from combination of two defects on parallel cube planes.

In the case of interaction between a defect on (100) or (010) with a defect on (001), one cannot be sure at a magnification of only 10500 whether the latter is a platelet or a dislocation loop, although sometimes abnormal contrast of the defect on (001) (e.g. the defect at (0.27, 0.82) in figure 4), or detectable departure from planarity in (001), indicates that the (001) defect is not a normal platelet. To avoid questionable classification, no differentiation between types of defect on (001) is attempted among the defects counted under feature 13. Similarly, there is no category for 'platelet + defect on (001)' since there is the likelihood that in the [110] zone axis view the images of a platelet on (100) or (010) and of a defect on (001) seen overlapping are of defects at different heights in the specimen, and not in contact. By 'loop fraction' (feature 14) it is meant that the loop segment contained within the specimen foil does not include the other defect with which interaction has occurred. A typical hairpin-shaped, voidite-containing loop fraction is at (0.94, 0.35) in figure 2. The presumption that there has been a reaction with another defect, not captured in the foil, follows from the extreme rarity, indeed possible absence, of loops seen entire and apparently without contact with any other defect. Diligent search disclosed only two examples, and they cannot be rated as more than 'very probable' because there exists the possibility of their being in contact with the tip of a defect on (001) of which too small a fraction is contained within the specimen for it to be detected in the micrographs. The much larger number of loop fractions seen in zone Z compared with region X is believed to result from there having been more very long laths in zone Z, and among these the proportion transforming into voidite-filled dipole loops has been high.

An important characteristic of specimen A4 is the absence of dislocations other than the loops enclosing voidite sheets. No grown-in dislocation, or dislocation associated with plastic deformation, was detected in any of the fields examined. Bearing in mind this circumstance, we can draw the following conclusions regarding the regions of specimen A4 subjected to close scrutiny. The primary conclusion is that transformation of a platelet into a voidite sheet surrounded by a dislocation loop is initiated when two platelets approach each other very closely. This concurs with Woods's (1976) view of the origin of dislocation loops in the two specimens he studied, both very similar to A4 in characteristics. The configurations observed in category 13 of table 3 suggest that a large majority of reactions have occurred when the tip of a lath meets a platelet surface on another cube plane, rather than from edgewise contact of platelets resulting from their lateral expansion. This finding is not surprising in view of the dominance of the lath shape. Taking average platelet dimensions and number densities from table 3, one can estimate that every cube of edge length 0.5 μm will contain on average a platelet parallel to one cube plane in each orientation, and that the average platelet area contained, when projected on the faces of the cube, will cover about a fifth of one cube face normal to each cubic axis. With the average lath length being equal to the cube face diagonal, the observed fraction of about 10% of all platelets having become involved in reactions is understandable, and one might expect perhaps twice that rate if platelets nucleated and grew independently of each other.

On the question of how close platelets can come without reacting, we have a single piece of evidence from three views, taken at a magnification of 48000, of the close proximity of the tip of a lath on (010) to the edge of a round on (100). Their separation could not be detected by parallax between images taken with specimen tilts of 30° on either side of the [110] zone axis orientation, and so is believed to have been not more than 2 nm.

A second conclusion drawn from the figures in table 3 is that whereas the transformation of platelets to voidite-filled dislocation loops is likely to spread to both of the platelets that have come into close proximity, in a substantial minority of cases (*ca.* 40%) one of the platelets remains untransformed. On the other hand, the rarity of partial platelets shows that transformation of a platelet, once started, has a very high probability of proceeding to completion (excluding the possible retention of segments of platelet annuli too narrow to be distinguished from the image of the peripheral dislocation in images at 10500 × magnification).

Turning now to consider specimen DL4, a quite different ratio of loops to platelets is evident, and most noteworthy is the presence of glide dislocations. Although large, evenly thinned areas were not available to provide low-magnification panoramas, the defect population can be summarized qualitatively as follows. The image areas were divided fairly sharply between those obscured by a high density of glide dislocations, and others containing relatively few glide dislocations, say about 1 per square micrometre, on average. In the latter, the dominant defects were voidite-filled dislocation loops. The ratio of elongated to equiaxed loops was about 3:2. Partial platelets were rare compared with complete loops, and complete platelets were rarer still.

(iii) *Burgers vectors of loop dislocations*

Finally we return briefly to the topic, introduced in §3*c*, of the Burgers vectors of dislocations surrounding voidite sheets. Examination of specimen DL4/B at Oxford with a JEOL JEM 100-B microscope operated at 100 kV (P. Pirouz, personal communication) disclosed Burgers vectors of magnitude a_0 normal to the plane of the loop. Of 12 loops analysed, Dr Pirouz found 10 to have this Burgers vector, and only 2 to have a $\frac{1}{2}\langle 110\rangle$ Burgers vector making 45° with the loop plane, i.e. the 50% shear, 50% prismatic loop type found by Woods (1976) and Stephenson (1977).† An examination of a set of micrographs of a field of loops, both equiaxed and elongated (called 'loops 1'), in specimen DL4/B, taken under a selection of '2-beam' diffraction conditions with the Philips EM 400 microscope at Bristol operating at 120 kV, yielded equal numbers of the normal $\frac{1}{2}\langle 110\rangle$ and the abnormal $\langle 001\rangle$ type of Burgers vector among 24 voidite-containing loops not displaying any significant departure from cube-plane orientation or any other unusual feature. (Examples of unusual features are 'loops within loops', and cases where the dislocation bounding the voidite sheet divides into a pair of dislocations along part of its trajectory.) Pirouz found all loops to be of interstitial character. Thus, on the evidence of determinations as yet small in number, it may be concluded that the dislocation bounding a voidite-filled loop is quite likely to have a Burgers vector that is not a primitive lattice translation, although the normal $\frac{1}{2}\langle 110\rangle$ Burgers vectors also occur among these dislocations.

† Further studies have brought the total of loops in specimen DL4/B analysed at Oxford up to 36. Two-thirds of them have Burgers vector a_0 normal to the loop plane (Hirsch *et al.* 1986*b*).

(*b*) *The volumes of voidites*

Here we report measurements of the volumes of individual voidites and of the voidite volume per unit area in voidite sheets. We consider in turn the selection of voidite sheets to be measured, the technique of measurement and the results obtained. The present measurements constitute an extension and refinement of those of Barry (1982) reported by Bursill (1983). Barry measured voidite volumes in five voidite-filled loops of aggregate area 0.13 μm^2. In the present work, 12 voidite sheets were studied, and measurements of voidite sizes were carried out over an aggregate area of 0.68 μm^2. Sheets containing relatively large and well-resolved voidites, and lacking any evident sea of small voidites, were the obvious candidates for analysis. Where possible, micrographs with least defocus were selected. The more 'simple' voidite-sheet configurations were preferred; in practice this resulted in choosing mainly those sheets located in large partial platelets rather than in platelet-free loops. The areas of interest in the selected micrographs were printed on to large sheets of film that were examined as transparencies on a viewing screen. They gave an overall magnification of 5×10^5. This magnification was adopted as being about the optimum for measuring voidite dimensions with the unaided eye against scales graduated in millimetres, fashioned as described below.

Parameters that could be used in measuring the volume, V, of a regular octahedron seen in projection along [110] are the length of the octahedron edge, e, parallel to $[1\bar{1}0]$, the perpendicular distance, p, between faces seen edge-on (i.e. between $(\bar{1}11)$ and its inverse, or between $(1\bar{1}1)$ and its inverse), or the side length, a, of the parallelogram outline of the octahedron. The lengths a are parallel to $[1\bar{1}2]$ and $[\bar{1}12]$ for the parallelogram sides formed by $(\bar{1}11)$ and $(1\bar{1}1)$, respectively.

The volume V is given by

$$V = 0.4714e^3 = 0.8660p^3 = 0.7258a^3. \tag{4}$$

For the many voidites that are elongated in one of the $\langle 110 \rangle$ directions in the cube plane of the voidite sheet, two dimensions have to be measured. Those chosen were the longer side, b, and the shorter side, a, of the parallelogram outline of the elongated octahedron seen in projection on (110). The formula for voidite volume V is then

$$V = 0.726a^3 + 1.089a^2(b-a). \tag{5}$$

The acute angle between a and b is $70\frac{1}{2}°$. Therefore scales were constructed to form a V of opening angle $70\frac{1}{2}°$ into which the voidite image could be tucked so that the scales lay along the loci, as best judged, of the $(\bar{1}11)$ and $(1\bar{1}1)$ faces seen edge-on. This shape-fitting technique avoids determining the positions of the octahedron apices pointing towards [001] and $[00\bar{1}]$. As was pointed out in §3 (*b*), when discussing euhedral images of voidites, the contrast of the image vanishes as these apices are approached. Keeping the measuring V with its bisector in a vertical orientation, and the [001] direction on the photographic sheet film bearing the voidite images also vertical, the dimensions a and b of a voidite image could be read off at one setting, and were derived from the positions of the images of the [110] edges of the elongated voidite as seen against the arms of the V. These voidite edges formed the relatively sharp, high-contrast corners of the parallelogram image. It is important that the scale markings should be fine, so as to obscure as little as possible of the intensity profile across the image. Most measurements were performed with scales in the form of rows of fine dots spaced 1 mm apart. The sheet films

of voidite images were developed to a low or moderate contrast to avoid strongly nonlinear regions of the photographic density characteristic curve. Such nonlinearities could introduce changes in the apparent size of objects. An allowance for microscope defocus was made subjectively, by comparing the images being measured with a standard through-focus series of voidite images. Only when dealing with the larger and best-focused voidite images can one have confidence in measuring a and b to within $\pm 10\%$ in the important size range between, say, 3 nm and 10 nm. Thus a minimum uncertainty of $\pm 30\%$ attaches to the resulting volume measurements. The advantage of making measurements on photographic film rather than on photographic paper prints is particularly clearly manifested when darkening of the background due to strain contrast is present, as is the case close to the dislocations surrounding voidite sheets. On film it was possible to make good measurements of many voidites lying close to dislocations, when on the prints those same voidite images were largely hidden by blackening due to the dislocation contrast.

The results of measurements on a total of 2062 voidites are given in table 4. The fraction of the voidite sheet area covered by the voidites themselves is not negligible; the fifth column of table 4 shows that it is about 0.1 on average. The total voidite sheet area over which measurements were made, A_g, and the net area, A_n, obtained after subtracting from A_g the aggregate area occupied by voidites on the cube plane of the voidite sheet, i.e. $\sqrt{2} \sin 70\frac{1}{2}^\circ \Sigma ab$, are both listed. In only half of the twelve sheets examined was it deemed profitable to attempt voidite image measurement over the whole sheet area appearing in the micrographs.

TABLE 4. VOIDITE VOLUMES

figure no.	micrograph no.	voidite sheet area/10^4 nm^2 gross (A_g)	net (A_n)	voidite sheet area (fraction covered by voidites)	no. of voidites measured, N	aggregate volume, ΣV / 10^4 nm^3	thickness of ΣV spread over A_n $(\Sigma V/A_n)$/nm	$(\Sigma V/A_n a_0)$
3	4709	5.57	4.94	0.11	141	1.76	0.35	0.99
9	7534	8.26	7.56	0.08	157	2.30	0.30	0.85
10*a*	7531	7.67	6.75	0.12	244	2.86	0.42	1.19
11	7524	7.11	6.65	0.06	71	1.83	0.27	0.77
13	7532	6.20	5.52	0.11	175	2.02	0.36	1.02
14	S7011	6.30	5.54	0.12	223	2.18	0.38	1.07
15*a*	Q7005	4.60	4.12	0.10	96	1.71	0.41	1.16
22*a*	E6952	1.52	1.42	0.06	28	0.29	0.20	0.57
25	4770	4.21	4.03	0.04	238	0.30	0.07	0.21
26*a*	I6966	9.28	8.29	0.11	418	2.43	0.29	0.82
27R	J6971	2.39	2.07	0.14	177	0.67	0.32	0.91
27L	J6971	4.96	4.76	0.04	94	0.50	0.10	0.29

It is considered that the most instructive way of expressing the aggregate voidite volume is to state the thickness of the layer it would form when uniformly spread over A_n. This reflects the belief that A_n is the area over which nitrogen in the platelet structure has been fully, or at least substantially, replaced by carbon to reconstitute normal diamond structure, and over which additional carbon layers have been introduced, in number depending upon the magnitude of the Burgers vector of the interstitial dislocation loop bounding the voidite sheet. Accordingly, the last two columns of table 4 show this thickness, $\Sigma V/A_n$, in absolute measure and also expressed as the ratio $\Sigma V/A_n a_0$, i.e. as a fraction of a cell edge a_0 of normal diamond.

Turning to consider the measurements on particular voidite sheets, some call for comment,

as follows. It is concluded that the most precise measurement of ΣV was obtained from the loop in figure 3, plate 1. This measurement benefited both from guidance afforded by a comprehensive through-focal series of images of this feature and from the substantial contribution to ΣV made by extremely elongated voidites. For such voidites, the uncertainty in V is mainly determined by the uncertainty in a^2 rather than in a^3, and in this sheet the uncertainty in the measurement of a is judged not to be in excess of $\pm 10\%$, on the basis of measurements of images in the through-focal series. It is believed that an accuracy of $\pm 30\%$ was achieved in the value of ΣV for this sheet. In the voidite sheets in figures 9, 10*a* (plate 4), 13 (plate 5), 14 (plate 6), and 26*a* (plate 11), of which certain parts only were used, the photographs give an idea what fraction of the sheet could profitably be included, namely, about three-quarters of the sheet area in figure 9, the left-hand half of the sheet in figure 10, the lower-middle part, only about one-third of the whole sheet area, in figure 13, and the right-hand half in figure 14. In figure 26*a*, the lower-left region of the sheet was excluded, although reasonably satisfactory measurements of the highly elongated members of the voidite population in that region could have been obtained. For each of these five voidite sheets just mentioned, $\pm 50\%$ is adopted as a cautious estimate of the uncertainty in the ΣV measurement. In figures 11 (plate 5), 15*a* (plate 6), and 22*a* (plate 9), all voidite images were good, but the numbers measured were smaller, and an uncertainty of $\pm 50\%$ in the ΣV value is again proposed, as a cautious estimate of the accuracy attained. Figure 25, plate 10, has a somewhat complicated dislocation configuration, but well-focused micrographs of this feature were available. It was also one of the five voidite sheets studied by Barry (1982); his findings will be quoted below. The 'R' and 'L' appended in the table to the figure number 27, plate 12, signify the voidite sheets on the right and left of figure 27, respectively. All the area of the left-hand sheet was used, but for the sheet on the right the upper-left part, comprising about one-third of the sheet area, was excluded. The noteworthy feature of these sheets is their disparity in values of $\Sigma V/A_n$. However, the left-hand sheet has abnormalities: there are some large voidites outside the confines of the dislocation loop. The latter situation also applies with regard to the loops in figure 28, plate 12. Measurement of the volumes of resolved voidites in the loops of figure 28 would clearly give a low value of $\Sigma V/A_n$. So too would such measurement in the case of the upper right-hand voidite sheet in figure 23, plate 10. The pair of sheets in figure 23 resembles those in figure 27 in representing cases of close juxtaposition of sheets, one apparently 'voidite-rich' and the other 'voidite-sparse', as far as voidites of measurable dimensions are concerned. (The upper right-hand loop in figure 23 and the loops in figure 28 were remarked upon in the discussion of bimodal distributions of voidite size in §3*d*, when the presence of 'voidite seas' in these loops was pointed out.) However, no voidite sea is detectable in the left-hand sheet in figure 27 nor in either half of the H-feature in figure 25. With regard to the other H-feature illustrated, figure 19 (plate 8), there is a disparity in mean voidite sizes on either side of the bridging dislocation and, as noted in §3*d*, a voidite sea is present to the right of this dislocation.

The measurements in table 4 can be summarized as follows. Six out of the seven voidite sheets associated with partial platelets, and three out of the five voidite sheets in features lacking observed areas of platelet contrast appear to belong to one class, exhibiting a ratio $\Sigma V/A_n a_0$ of about unity. In the case of the one partial platelet whose voidite sheet yielded a ratio only half this value, the number of voidites measured was small. The mean value of $\Sigma V/A_n a_0$ for this majority class, derived from table 4 by weighting measurements on individual voidite sheets

proportionally to N, including the sheet of figure 22*a*, but excluding those of figures 25 and 27L, comes out as 0.97.

We may now compare the present measurements with those of Barry (1982). He expressed his volume measurements in terms of the ratio $2\Sigma V/A_g a_0$. Dividing his figures by two renders them comparable with the last column of table 4, to sufficient accuracy. In the order of their listing by Bursill (1983) they become 0.31, 0.23, 0.41, 0.25 and 0.39, values all much lower than those of the majority class in table 4. The ratio 0.23 just quoted is Barry's value for the H-feature of figure 25, in good agreement with that in table 4. The four other ratios were found in loops of the following types: 0.31, a loop truncated by both specimen surfaces, shown in figure 3*b* of Bursill's (1983) review; 0.41, another doubly truncated loop; 0.25 and 0.39, two adjacent and apparently associated loops.

Our use of the ratio $\Sigma V/A_n a_0$ is not to be taken as implying the assumption that all the carbon in the volume of diamond equal to the total voidite volume has been available for distribution over A_n. The amount of carbon remaining in the voidites is unknown. All that can be said concerning the present voidite contents is that its density is not greater than about one-third that of the diamond matrix. This conclusion derives from comparison of the observed electron microscopic contrast with simulations of voidite images, for example the simulations of Anstis & Hutchison (1982). If the matter within the voidite were half carbon and half nitrogen, condensed with the stoichiometry of paracyanogen, $(CN)_x$, say, then the amount of carbon available for distribution over A_n would be reduced to not less than about $\frac{5}{6}$ of the value used in calculating the last two columns of table 4, a reduction of no great significance. The replacement of the nitrogen in either the Lang or zig-zag models of the platelet structure requires a diamond layer of thickness $0.25a_0$. To form a normal $\frac{1}{2}\langle 110\rangle$ interstitial dislocation loop as well requires a layer of thickness $0.75a_0$, and if the Burgers vector were of magnitude a_0 perpendicular to the platelet plane then the thickness needed is $1.25a_0$. However, it is necessary to consider where the replaced nitrogen might go, and to what extent its dispersal in point defects will generate a supply of carbon atoms adequate, or more than adequate, to replace the dinitrogens in platelets. These questions are discussed below.

(*c*) *The formation of voidites*

In this discussion of platelets and voidites we assume that the only impurity element in diamond we have to deal with is nitrogen. In actual fact there is evidence both from mass-spectrographic analysis (Melton & Giardini 1976) and from non-destructive nuclear analysis techniques (Sellschop *et al.* 1980) that both hydrogen and oxygen can be present in concentrations comparable with that of nitrogen in average type Ia specimens. Most of the oxygen found is likely to come from microscopic non-diamond mineral inclusions, but in the case of hydrogen the manifestation of sharp lines in the infrared absorption spectrum at 3107 and 1405 cm^{-1} provides not only easily ascertainable evidence of this element's presence but also shows it to be bound to carbon, probably in the vinylidene group $>C{=}CH_2$ (Woods & Collins 1983). However, no lines at 3107 and 1405 cm^{-1} were detected in the infrared absorption spectrum of specimen DL4. We take this as justifying the conclusion that bound hydrogen has no particular association with voidite-containing diamonds, and we exclude it from a role in the processes of platelet and voidite formation that we will outline.

We discuss first the formation of platelets, and will look at reactions involving A-defects, B-defects and platelets. For the structure of the A-defect we adopt Davies's (1976) proposal:

two nitrogen atoms substituting for two carbon atoms on adjacent atomic sites in the diamond structure. Regarding the B-centre, we assume that it contains the next smallest even number of nitrogen atoms, i.e. four. A very plausible model (J. Loubser & J. Van Wyk 1981, personal communication), that we accept, is four nitrogen atoms substituting for four carbon atoms tetrahedrally surrounding a carbon vacancy. The process of aggregating singly substituted nitrogen atoms into dinitrogen A-defects, i.e. that of converting diamond from type I b to type I a A, is now quite well understood (Evans & Qi 1982), but it does not concern us here, for we take a type I a A diamond as our starting material.

As described in §2*b*, A-defects, B-defects and platelets are each identified by characteristic infrared absorption features. Brozel *et al.* (1978) introduced a graphical method of displaying the relative strengths of these three absorptions in type I a diamonds, as follows. The abscissa scale is the percentage of B (or A) features in the sum of the overlapping A and B profiles, and spans the range from type I a A to type I a B diamond. The ordinates show the ratio (on an arbitrary scale) of the 'platelet' absorption peak at 7.3 μm to the total amount of nitrogen in A and B defects derived from equations (2) and (3) of §2*b*. Davies (1981) applied the same plotting method (but with ordinates equal to $\mu(7.3)/\mu(7.8)$, i.e. to the ratio of absorption at 7.3 μm to the total absorption at 7.8 μm) to a larger sample, of over 50 specimens. The majority of Davies's specimens lay in the range between the type I a A limit and those having a value of about 0.5 in their ratio $\mu^{\mathrm{A}}_{7.8}/\mu(7.8)$, i.e. the ratio of the contribution of A-feature absorption at 7.8 μm, symbolized by $\mu^{\mathrm{A}}_{7.8}$, to total absorption at 7.8 μm. This majority of 'mainly A' specimens showed a very clear trend of linear proportionality of $\mu(7.3)/\mu(7.8)$ to $\mu^{\mathrm{B}}_{7.8}/\mu(7.8)$, where $\mu^{\mathrm{B}}_{7.8}/\mu(7.8) = 1-[\mu^{\mathrm{A}}_{7.8}/\mu(7.8)]$. There is thus proportionality of 'platelet' absorption to B-feature absorption, for most specimens in this range of diamond types.

We regard Davies's plot as highly significant, and interpret it as showing that the primary reaction for platelet formation is

$$l\mathrm{A} = m\mathrm{P} + n\mathrm{B}, \tag{6}$$

where A and B represent a single A-defect and B-defect, respectively, P is a unit of area a_0^2 of platelet structure and l, m and n are integers. Each defect can be produced by inserting α nitrogen atoms and removing β carbon atoms. Thus for the A-defect, $\alpha = 2, \beta = 2$, and for the B-defect $\alpha = 4$ and $\beta = 5$. If the platelet has the structure of the Lang or zig-zag models then $\alpha = 4$ and $\beta = 2$ for P. With these values of α and β, (6) becomes

$$6\mathrm{A} = \mathrm{P} + 2\mathrm{B}. \tag{7a}$$

Equation (6) will balance provided the ratio α/β for A is intermediate between its values for P and B. If, for example, we took a less simple platelet model, P′, with less nitrogen and lower density, having $\alpha = 7$ and $\beta = 4$ in 2P′, say, then (7*a*) would be replaced by

$$19\mathrm{A} = 4\mathrm{P}' + 6\mathrm{B}. \tag{7b}$$

In the reaction of (7*b*), less nitrogen from A defects goes into B defects than in (7*a*). Equation (6) assumes that the nitrogen concentration is large compared with the concentration of carbon vacancies or interstitials in the diamond before or after the reaction. This should be so in the majority of type I a diamonds, which have a low dislocation density. If severe plastic deformation takes place before or during the epoch of platelet formation, (6) may not be applicable, and the diamonds affected might not follow the linear trend on the Brozel–Davies plot.

At this juncture we may introduce voidites as possible reagents in addition to A, B and P. Since voidites are {111}-faceted, negative crystals in type Ia diamonds, it is natural to assume that their surfaces are lined with nitrogen so as to eliminate dangling carbon bonds. One can construct a series of increasing sizes of regular octahedral voidites with adsorbed nitrogen on their surfaces in the way described by Bursill (1983), and define a voidite order, n, that for $n \geqslant 2$ is recognizable as one unit less than the number of diamond (111) interplanar spacings in the distance, p, between voidite facets: $p = (n+1)\, d_{111}$, where $d_{111} = 0.206$ nm. The B defect falls into place as a voidite of first order, and we may begin the enumeration of voidite hierarchy with it, as shown in table 5 (adapted from Bursill (1983), and corrected). With this model the ratio α/β steadily diminishes as n increases; for voidites of 5 nm diameter it has fallen to about 0.1. However, we envisage the likelihood of residual matter within voidites. Within the bulk of the voidite such matter might have a density possibly as high as one-third the density of the diamond matrix, as explained in §4*b*. If the matter were solely nitrogen, there would then be a limiting ratio α/β of about $\frac{1}{3}$ for very large voidites, and if carbon and nitrogen were present in equal proportions the limiting ratio would be about $\frac{1}{5}$.† (We note in passing that the absence of detectable strain contrast patterns due to high internal pressure in voidites, discussed in §3*d*, is not a critical indicator of the maximum possible nitrogen pressure in voidites. The rigidity modulus of the diamond matrix is much higher, and the voidite size relatively small, in comparison with the cases of faceted, radiation-produced gas bubbles in metals that have been much studied. Cochrane & Goodhew (1983) simulated two-beam images of cubic bubbles, edge length 20 nm, in vanadium, and concluded that the gas pressure in the bubble must reach between 0.5 and 0.75 GPa before significant strain contrast would be observable. Although our diffraction conditions were different, we may scale their results to obtain a rough estimate that a pressure of between 6.5 and 10 GPa would be needed in a relatively large voidite, 10 nm in diameter, to produce significant strain contrast. Since nitrogen gas reaches a density one-quarter that of diamond at a pressure of only 1.5 GPa at room temperature (Bridgman 1924), we believe that we must depend upon the phase contrast evidence to provide an upper limit to the density of voidite contents, whether volatile or not.)

Observe the possibility that higher-order voidites could be formed together with B defects during platelet formation. Equation (6) can be modified to become

$$l\mathrm{A} = m\mathrm{P} + n\mathrm{B} + \Sigma r_n V_n. \tag{8}$$

It is easily verified that the introduction of voidites will drastically reduce the ratio n/l compared with its values in (7*a*) and (7*b*). Now the plots of both Brozel *et al.* (1978) and Davies (1981) include a few diamonds that exhibit the 7.3 μm 'platelet' absorption without detectable B absorption. If (8) applied to these diamonds, then their apparent anomalous infrared absorption behaviour would be explained. It would be desirable to perform a high-resolution electron microscopic examination of platelet-containing diamonds that have anomalously low B absorption. The presence of small voidites on some platelet areas of specimen DL4 has been pointed out in §3*d* (see table 1). It must be regarded as an open question whether these originated during the processes of platelet formation or platelet elimination.

† Recent electron diffraction and imaging experiments have detected a face-centred cubic crystalline phase within voidites (Barry 1986; Hirsch *et al.* 1986*a*, *b*). The latter workers confirmed by electron energy-loss spectra that nitrogen was a major constituent of voidite contents. Barry suggests that the crystalline phase is NH_3, Hirsch *et al.* that it is a new high-pressure allotrope of nitrogen.

TABLE 5. VOIDITE HIERARCHY

order	symbol	α	β	α/β	diameter/nm
1	$V_1 \equiv \mathrm{B}$	4	5	0.8	—
2	V_2	16	26	0.61	0.6
3	V_3	36	71	0.51	0.8
4	V_4	64	148	0.43	1.0
5	V_5	100	265	0.38	1.2
n	V_n	$\alpha = 4n^2$	$\beta = 4n^2 + \sum_{k=1}^{n} (2k-1)^2 = \frac{1}{3}n(4n^2+12n-1)$		

Granted the presence of voidites on or close to a platelet, there is the possibility of some platelet elimination accompanied by a redistribution of voidite sizes towards lower orders. Equations (9*a*) and (9*b*) offer simple illustrations of this process, by using the values of α and β in table 5,

$$8\mathrm{P} + 3\mathrm{V}_2 = 20\mathrm{B} \qquad (9a)$$

$$7\mathrm{P} + 5\mathrm{V}_3 = 13\mathrm{V}_2. \qquad (9b)$$

Note from table 1 that when fringing voidites have been observed, so too have voidites on platelet areas. In figure 11, the platelet area is small, and the number of voidites seen on this area is too small to indicate whether they and the fringing voidites have significantly different size distributions. As described in §3*d*, voidites on platelets and fringing voidites are similar in sizes and numbers in figures 9 and 15, but in figure 14 the voidites on the platelet do appear larger and more numerous than the fringing voidites. Thus there is mixed support for the process exemplified by (9*a*) and (9*b*).

Finally we consider the dominant processes of platelet elimination and voidite formation, those in which the resulting voidite sheet is surrounded by a perfect dislocation loop of interstitial character. The two possible dislocations will be symbolized by $D_{\frac{1}{2}}$ for the 50 % shear, 50 % prismatic dislocation having a Burgers vector of $\frac{1}{2}\langle 110\rangle$ type, and by D_1 for the pure edge dislocation with Burgers vector equal to a_0 normal to the loop plane. As discussed in §§2*a* and 2*c*, a normal platelet is surrounded by an imperfect dislocation whose Burgers vector is $\boldsymbol{u}_\mathrm{m} = \boldsymbol{u}_\mathrm{p}$ normal to the platelet plane, i.e. having Burgers vector components $(0, 0, u_\mathrm{p})$ in the case of a platelet parallel to (001). This dislocation we call D_p. The imperfect dislocation at the boundary between an area of untransformed platelet and a voidite sheet will have Burgers vector components $(0, \frac{1}{2}, \frac{1}{2}-u_\mathrm{p})$, where the loop dislocation bounding the voidite sheet is of $D_{\frac{1}{2}}$ type, and we call this imperfect dislocation $D_{\frac{1}{2},\mathrm{p}}$. When the loop dislocation is of type D_1 the corresponding Burgers vector components of the imperfect dislocation (which we call $D_{1,\mathrm{p}}$) are $(0, 0, 1-u_\mathrm{p})$. Taking $u_\mathrm{p} = 0.356a_0$, the value obtained from the electron microscopic moiré measurements (Bursill *et al.* 1981), the values of b^2 for the dislocations $D_{\frac{1}{2},\mathrm{p}}$ and $D_{1,\mathrm{p}}$ are $0.27a_0^2$ and $0.41a_0^2$, respectively. There is repulsion between D_p and both $D_{\frac{1}{2},\mathrm{p}}$ and $D_{1,\mathrm{p}}$, greater in the case of the latter dislocation as shown by the relative values $\boldsymbol{b}_\mathrm{p}\cdot\boldsymbol{b}_{\frac{1}{2},\mathrm{p}} = 0.05$ and $\boldsymbol{b}_\mathrm{p}\cdot\boldsymbol{b}_{1,\mathrm{p}} = 0.23$. Narrow annular strips of platelet contrast surrounding voidite sheet areas in partial platelets were described earlier (see §3*b* and table 1). It is presumed that they indicate situations where the driving force for completion of the platelet elimination reaction has been insufficient to overcome the mutual repulsion between the imperfect dislocations on either side of the platelet strip.

Consider first the reaction when the loop dislocation bounding the voidite sheet is $D_{\frac{1}{2}}$. The removal of P and the passage of $D_{\frac{1}{2}}$ over its area must be balanced by the formation of defects giving an average ratio α/β of $\frac{4}{6}$. This is achieved in the reaction

$$(\mathrm{P}-D_{\frac{1}{2}}) = \mathrm{B}+V_0, \tag{10}$$

where V_0 represents a single carbon vacancy in the diamond structure. Assuming that the individual carbon vacancies, V_0, aggregate to form electron-microscopically observable voidites, then the resulting voidite sheet would have $\Sigma V/A_{\mathrm{n}}\,a_0 = 0.12$, lower than that of any sheet measured so far. We can obtain magnitudes of $\Sigma V/A_{\mathrm{n}}\,a_0$ in line with those found by Barry (1982) and the lowest values in table 4 by filling the voidites with nitrogen up to the permissible maximum allowed by the phase contrast criterion. As previously stated, this would give $\alpha/\beta = \frac{1}{3}$ for very large voidites. For smaller voidites, of diameter *ca.* 5 nm, say, the contribution to their nitrogen capacity from the concentrated layer of adsorbed nitrogen on their surfaces is not insignificant, and would raise α/β into the range 0.4–0.45. The products of the platelet elimination reaction could then be distributed between B defects and voidites in proportions such as suggested by the equation

$$10(\mathrm{P}-D_{\frac{1}{2}}) = 8\mathrm{B}+(8\mathrm{N}-20\mathrm{C}), \tag{11}$$

with the components going into voidite formation enclosed in the bracket on the right-hand side. Here the value of α/β for voidites is 0.4, on average, and $\Sigma V/A_{\mathrm{n}}\,a_0$ is 0.25, corresponding roughly with the low values in table 4.

Turning now to consider reactions involving D_1 we find more flexibility in the range of solutions. Equation (12) illustrates a possible distribution of reaction products,

$$10(\mathrm{P}-D_1) = 4\mathrm{B}+(24\mathrm{N}-80\mathrm{C}). \tag{12}$$

The value of α/β is down to 0.3 for the voidite average, and $\Sigma V/A_{\mathrm{n}}\,a_0$ is 1.0, in agreement with the average for the majority class of voidite sheets in table 4. It is easily verified that the value of $\Sigma V/A_{\mathrm{n}}\,a_0$ will remain about unity if some carbon remains in the voidite to give voidite contents containing carbon and nitrogen in equal proportions: the needed reduction of α/β to about 0.2 for the average voidite can be achieved by increasing the B/P ratio to between 0.6 and 0.7. It may be concluded from the equations above that the disadvantage of introducing a dislocation of larger Burgers vector in platelet elimination reactions is outweighed by the smaller number of B defects (or voidites of very low order) that have to be produced, and by the presumably lower energy of voidites having a lower nitrogen content.

As yet we have no electron-microscopic evidence concerning the process of nucleation of dislocations of either $D_{\frac{1}{2}}$ or D_1 type in specimens such as DL4, where voidite sheet formation has not usually been triggered by close approach of platelets. We observe glide dislocations trapped on partial platelets and voidite sheets (see table 1), but whether these dislocations have promoted or impeded platelet elimination is not apparent. It will be recalled that in the description of figure 16 in §3*c* a situation was described that could be interpreted as impediment of the platelet-to-voidite transformation front by a trapped dislocation lying on the untransformed platelet.

The authors thank Professor Sir Charles Frank, F.R.S., and Professor Sir Peter Hirsch, F.R.S., for their interest and advice. Financial support from the U.K. Science and Engineering

Council is gratefully acknowledged, and also from the following bodies by the authors indicated: the Australian Research Grants Committee and the University of Melbourne (J.C.B. and L.A.B.) and De Beers Industrial Diamond Division (Pty) Ltd (A.R.L.).

References

Anstis, G. R. & Hutchison, J. L. 1982 In *Proc. 10th Int. Conf. on Electron Microscopy* (*Hamburg*), vol. 2, pp. 93–94.
Barry, J. C. 1982 Ph.D. thesis, University of Melbourne.
Barry, J. C. 1986 *Ultramicroscopy* **20**, 169–176.
Barry, J. C., Bursill, L. A. & Hutchison, J. L. 1983 *Phil. Mag.* A **48**, 109–121.
Barry, J. C., Bursill, L. A. & Hutchison, J. L. 1985 *Phil. Mag.* A **51**, 15–49.
Berger, S. D. & Pennycook, S. J. 1982 *Nature, Lond.* **198**, 635–637.
Bridgman, P. W. 1924 *Proc. Am. Acad. Arts Sci.* **59**, 173–211.
Brozel, M. R., Evans, T. & Stephenson, R. F. 1978 *Proc. R. Soc. Lond.* A **361**, 109–127.
Bursill, L. A. 1983 *Endeavour* **7**, 70–77.
Bursill, L. A., Hutchison, J. L., Sumida, N. & Lang, A. R. 1981 *Nature, Lond.* **292**, 518–520.
Clark, C. D. & Davey, S. T. 1984 *J. Phys.* C **17**, 1127–1140.
Cochrane, B. & Goodhew, P. J. 1983 *Physica Status Solidi* A **77**, 269–282.
Collins, A. T. 1982 *J. Phys.* D **15**, 1431–1438.
Collins, A. T. & Woods, G. S. 1982 *Phil. Mag.* B **45**, 385–397.
Davies, G. 1970 *Nature, Lond.* **225**, 758.
Davies, G. 1972 *J. Phys.* C **5**, 2534–2542.
Davies, G. 1976 *J. Phys.* C **9**, L537–542.
Davies, G. 1977 *Chemy Phys. Carbon* **13**, 1–143.
Davies, G. 1980 *Ind. Diam. Rev.* **40**, 466–469.
Davies, G. 1981 *Nature, Lond.* **290**, 40–41.
Davies, G. & Summersgill, I. 1973 In *Diamond Research 1973*, pp. 6–15. London: Industrial Diamond Information Bureau.
Evans, T. 1978 In *Diamond Research 1978*, pp. 17–22. Ascot: De Beers Industrial Diamond Division (Pty) Ltd.
Evans, T. & Phaal, C. 1962 *Proc. R. Soc. Lond.* A **270**, 538–552.
Evans, T. & Qi, Z. 1982 *Proc. R. Soc. Lond.* A **381**, 159–178.
Frank, F. C. 1964 *Proc. phys. Soc.* **84**, 745–748.
Hanley, P. L., Kiflawi, I. & Lang, A. R. 1977 *Phil. Trans. R. Soc. Lond.* A **284**, 329–368.
Hirsch, P. B., Hutchison, J. L. & Titchmarsh, J. M. 1986*a* *Phil. Mag.* A **54**, L49–L54.
Hirsch, P. B., Pirouz, P. & Barry, J. C. 1986*b* *Proc. R. Soc. Lond.* A **407**, 239–258.
Hoerni, J. A. & Wooster, W. A. 1955 *Acta crystallogr.* **8**, 187–194.
Humble, P. 1982 *Proc. R. Soc. Lond.* A **381**, 65–81.
Humble, P., Mackenzie, J. K. & Olsen, A. 1985*a* *Phil. Mag.* A **52**, 605–622.
Humble, P., Lynch, D. F. & Olsen, A. 1985*b* *Phil. Mag.* A **52**, 623–641.
Hutchison, J. L. & Bursill, L. A. 1983 *J. Microsc.* **131**, 63–66.
Hutchison, J. L., Bursill, L. A. & Barry, J. C. 1982 *Inst. Phys. Conf. Ser.* no. 61, pp. 369–372.
James, P. F. & Evans, T. 1965 *Phil. Mag.* **11**, 113–129.
Kaiser, W. & Bond, W. L. 1959 *Phys. Rev.* **115**, 857–863.
Lang, A. R. 1964 *Proc. phys. Soc.* **84**, 871–876.
Lang, A. R. 1977 *Phil. Mag.* **36**, 495–500.
Lang, A. R. 1979 In *Properties of diamond* (ed. J. E. Field), pp. 425–469. London: Academic Press.
Melton, C. E. & Giardini, A. A. 1976 *Nature, Lond.* **263**, 309–310.
Moore, M. & Lang, A. R. 1972 *Phil. Mag.* **25**, 219–227.
Moore, M. & Lang, A. R. 1977 *J. appl. Crystallogr.* **10**, 422–425.
Raman, C. V. & Nilakantan, P. 1940 *Proc. Indian Acad. Sci.* A **11**, 389–397.
Sellschop, J. P. F., Madiba, C. C. P. & Annegarn, H. J. 1980 *Nucl. Instrum. Meth.* **168**, 529–534.
Stephenson, R. F. 1977 Ph.D. thesis, University of Reading.
Sumida, N. & Lang, A. R. 1981*a* *Inst. Phys. Conf. Ser.* no. 60, pp. 319–324.
Sumida, N. & Lang, A. R. 1981*b* *Phil. Mag.* A **43**, 1277–1287.
Sumida, N. & Lang, A. R. 1982 *J. appl. Crystallogr.* **15**, 266–274.
Sumida, N. & Lang, A. R. 1987 (In preparation.)
Suzuki, S. & Lang, A. R. 1975 *Acta crystallogr.* A **31**, S260.
Takagi, M. & Lang, A. R. 1964 *Proc. R. Soc. Lond.* A **281**, 310–322.
Walker, J. 1979 *Rep. Prog. Phys.* **42**, 1605–1659.
Woods, G. S. 1976 *Phil. Mag.* **34**, 993–1012.
Woods, G. S. & Collins, A. T. 1983 *J. Phys. Chem. Solids* **44**, 471–475.

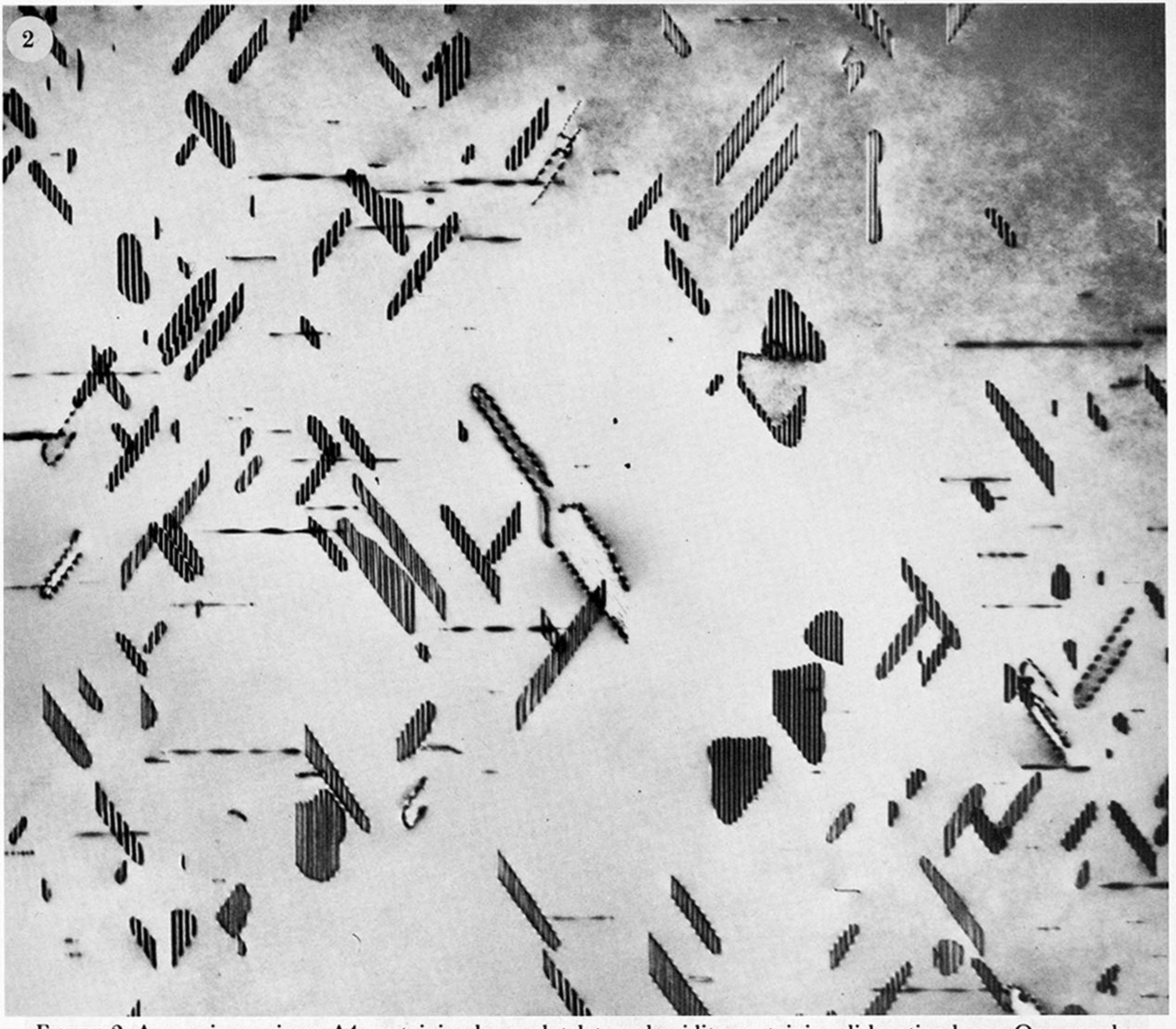

FIGURE 2. A zone in specimen A4 containing large platelets and voidite-containing dislocation loops. One annular partial platelet also appears. Specimen thickness in centre of field is 0.3 μm. Electron accelerating voltage 120 kV. In this figure and in figures 4 and 8, [001] points towards top of field and the field width is 4 μm (8071, original magnification ×10500).

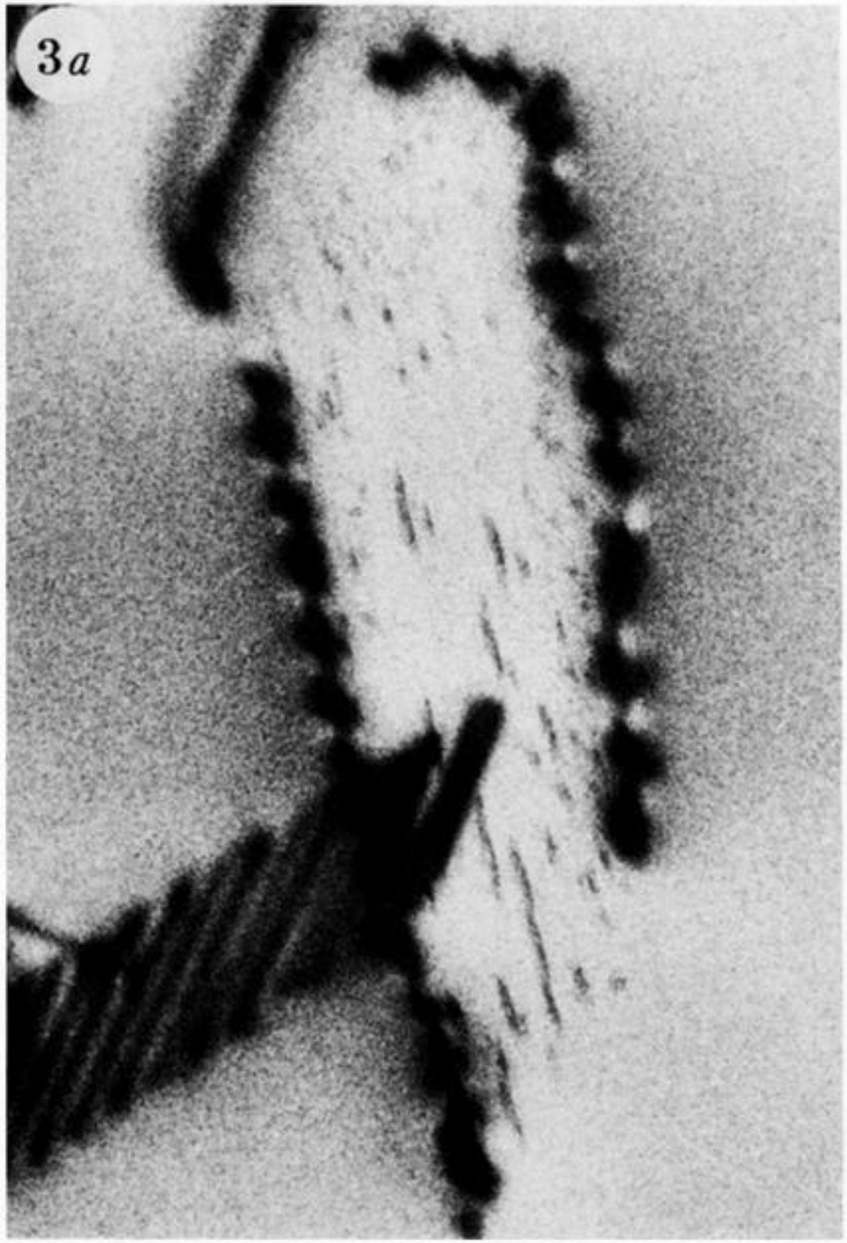

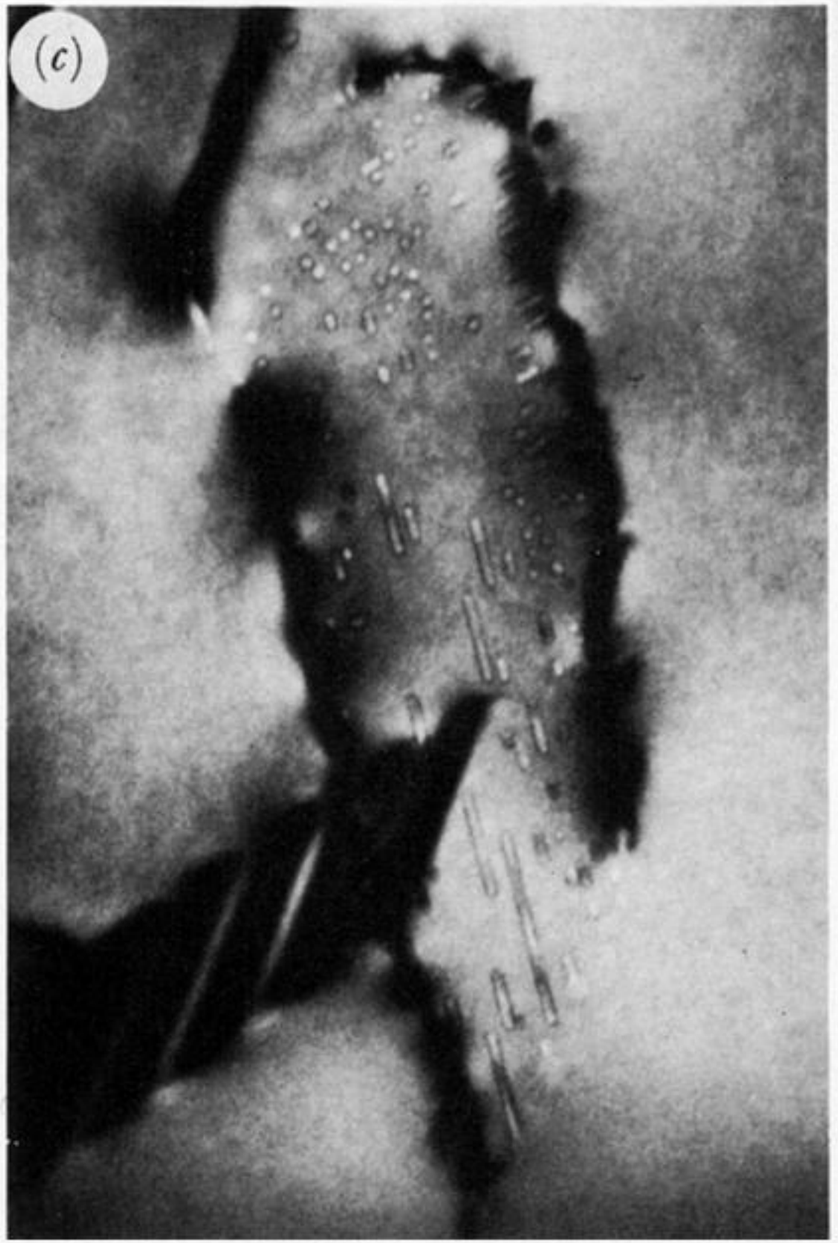

FIGURE 3. Detail in the large voidite-containing loop at the centre of the field of figure 2. The image is rotated about 17° clockwise relative to figure 2 (magnification $\times 160000$). (*a*) Enlargement from the low-magnification micrograph, figure 2. (*b*) High magnification and resolution, electron accelerating voltage 200 kV, close to optimum focus. Longest voidite image is about 3×80 nm in projection. (4709, original magnification $\times 10^5$.) (*c*) As (*b*), but underfocused by about 1 μm (4716).

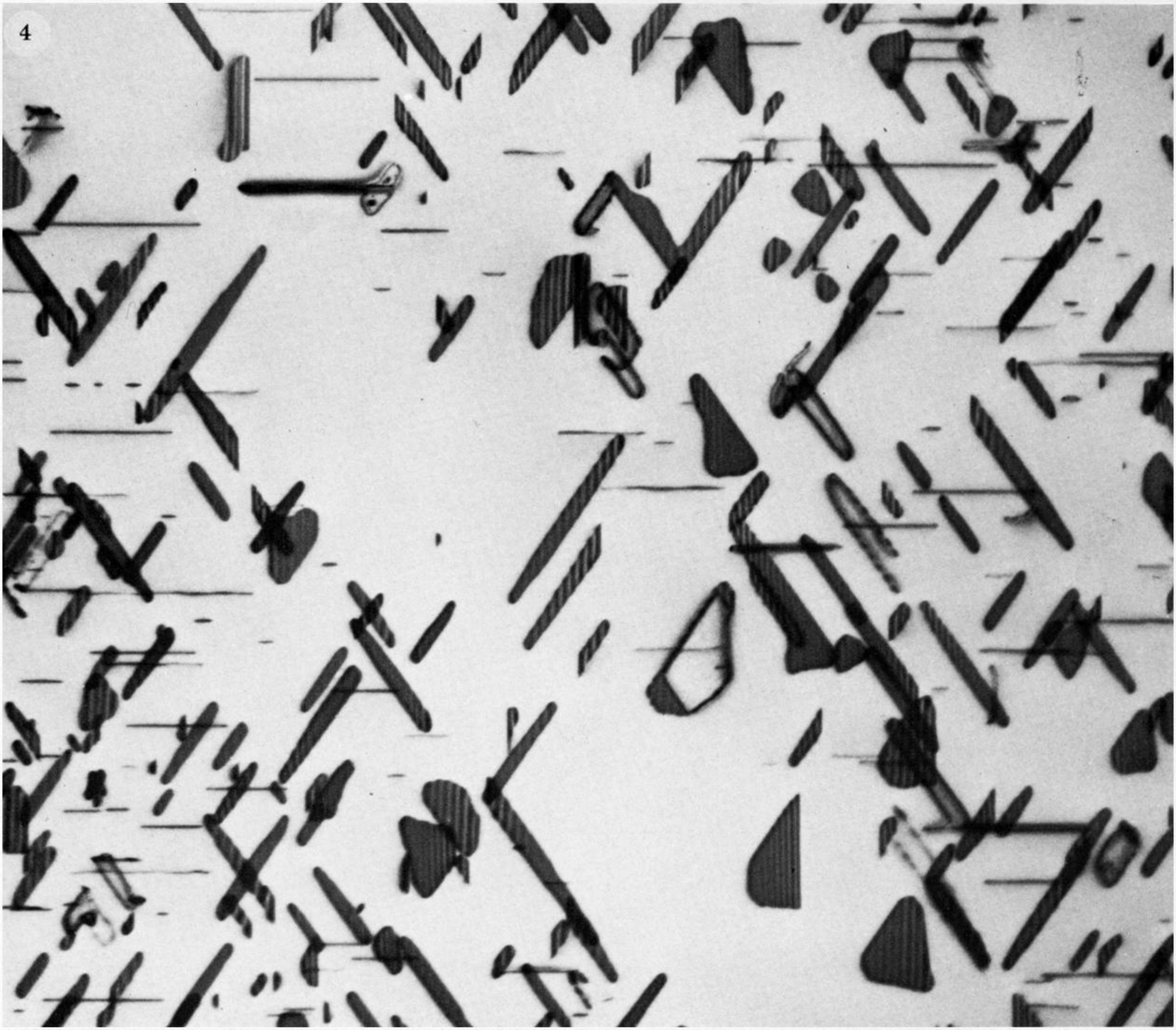

FIGURE 4. A field in the same zone of specimen A4 as that shown in figure 2, but in a region where specimen thickness is 0.5 μm. The longest dimension of the annular platelet at (0.60, 0.35) is 0.6 μm. The longest platelet lath entirely contained within the specimen is 0.83 μm long. Electron accelerating voltage 120 kV. Field width 4 μm (8045, original magnification ×10500).

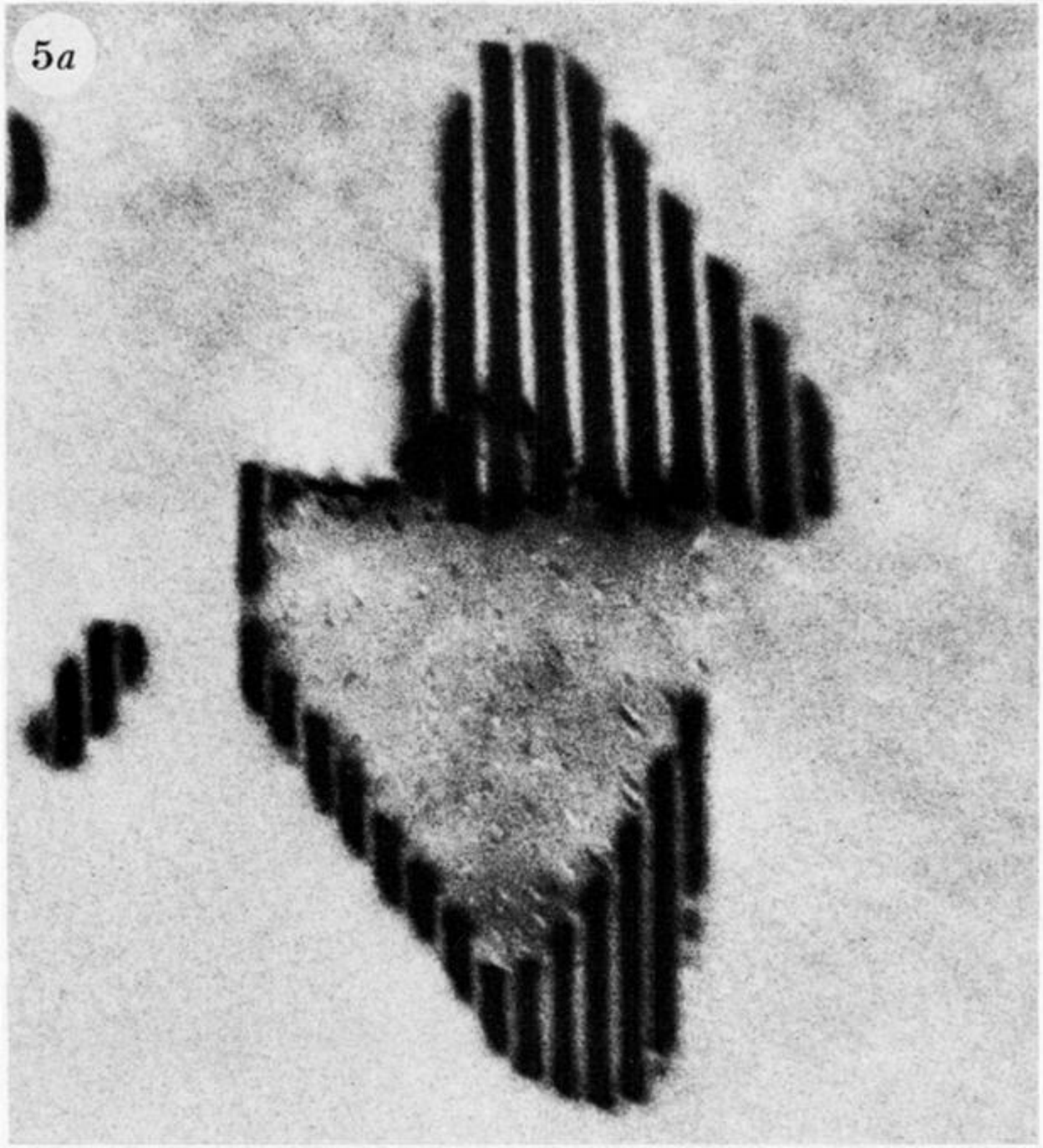

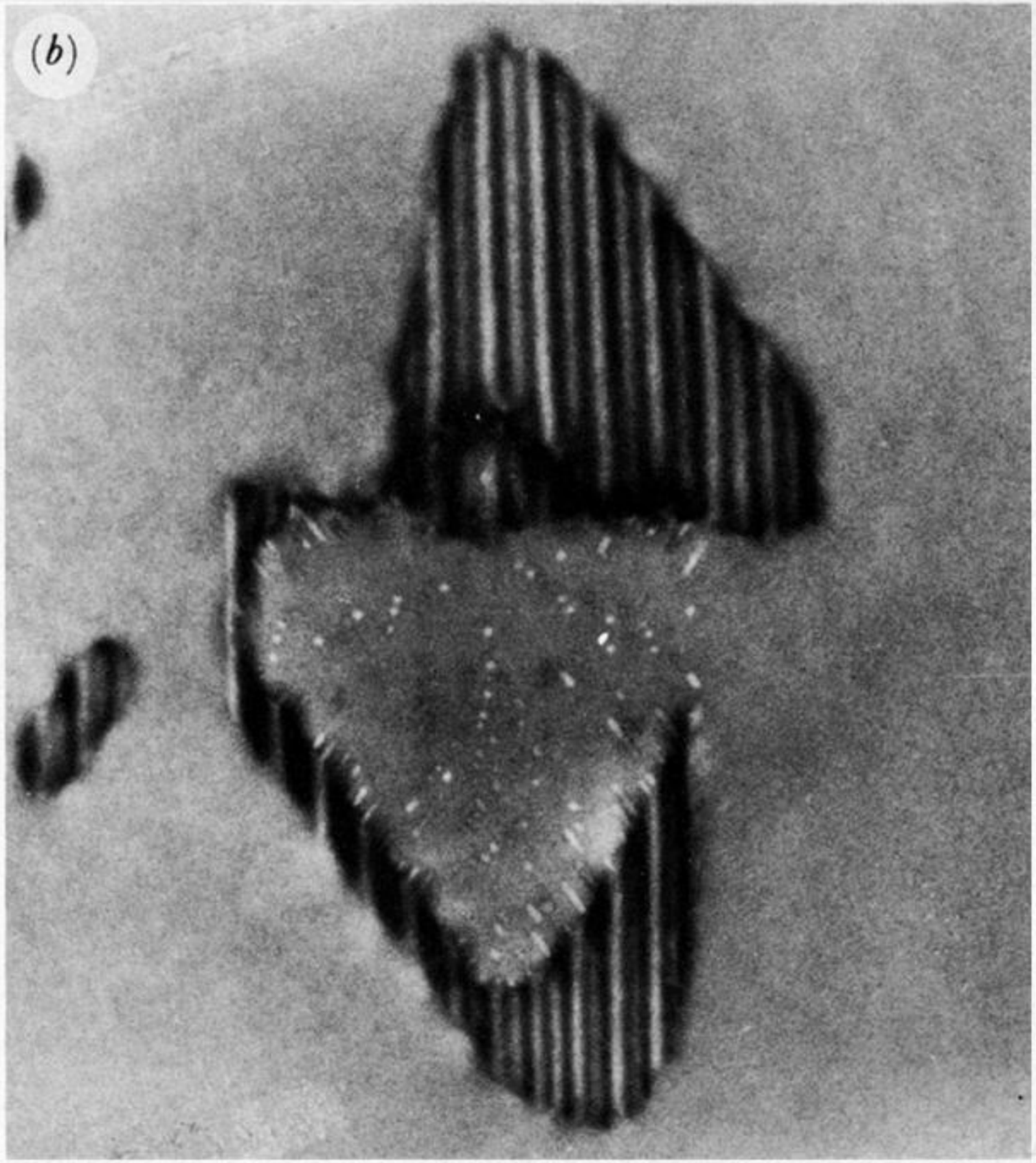

FIGURE 5. Detail of the platelet combination seen at (0.67, 0.60) in figure 2. The local specimen thickness is 0.22 μm (magnification ×160000). (*a*) Enlargement from figure 2; (*b*) higher resolution, electron accelerating voltage 200 kV. Focus chosen to maximize visibility of voidites at depths that produce light contrast on print (4686, original magnification $\times 10^5$).

FIGURE 6. X-ray section topograph through specimen DL4 showing intersecting {111} slip traces. Height of section 2 mm. Direction [00$\bar{1}$] vertical. Bragg reflection 2$\bar{2}$0 obtained in symmetrical transmission through 1 mm thick specimen, projection of diffraction vector points to the right. Cu Kα_1 radiation, Bragg angle 37.6°.

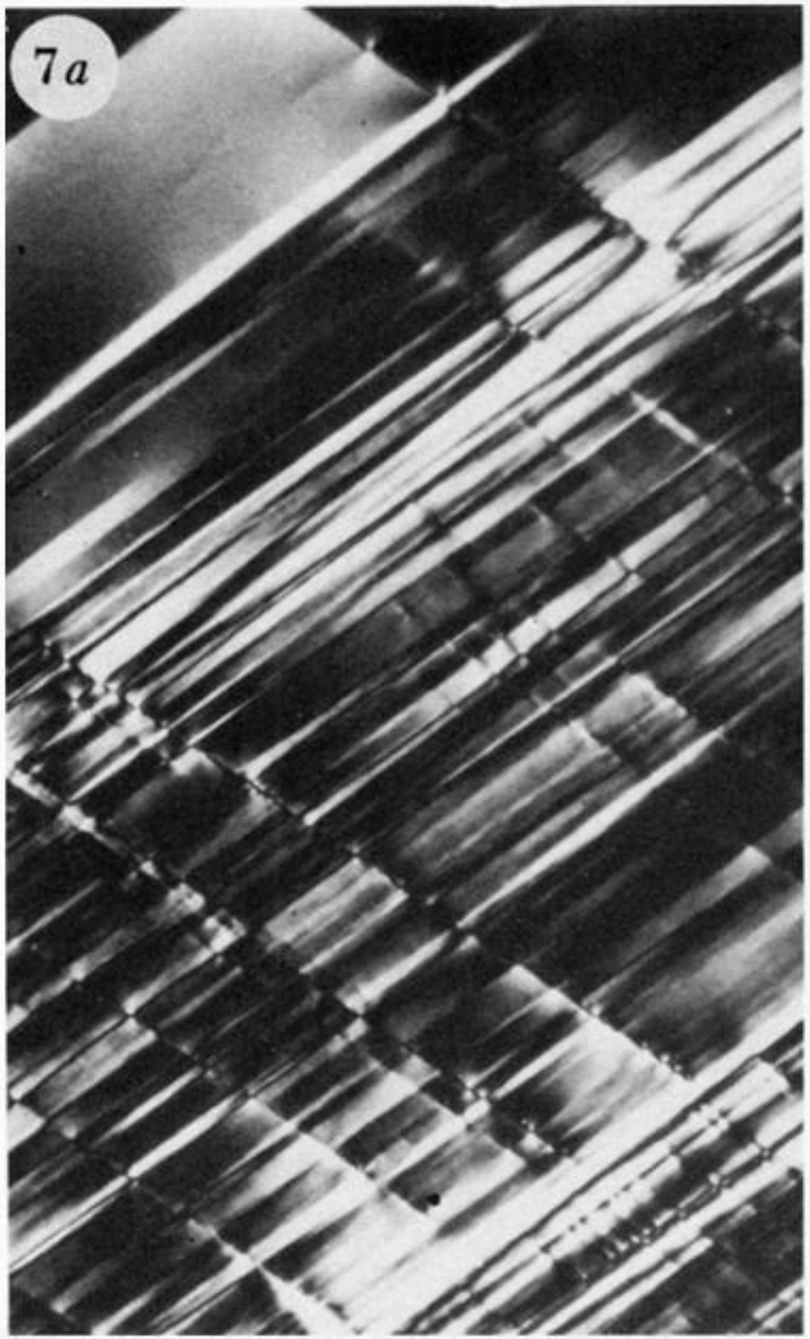

FIGURE 7. Birefringence patterns of polished, 50 μm thick, (110) orientation section of specimen DL4 before ion-beam thinning. Field width 0.3 mm. Specimen orientation rotated for strong visibility of (*a*) {111} slip bands, and (*b*) slip-band intersections and individual dislocations.

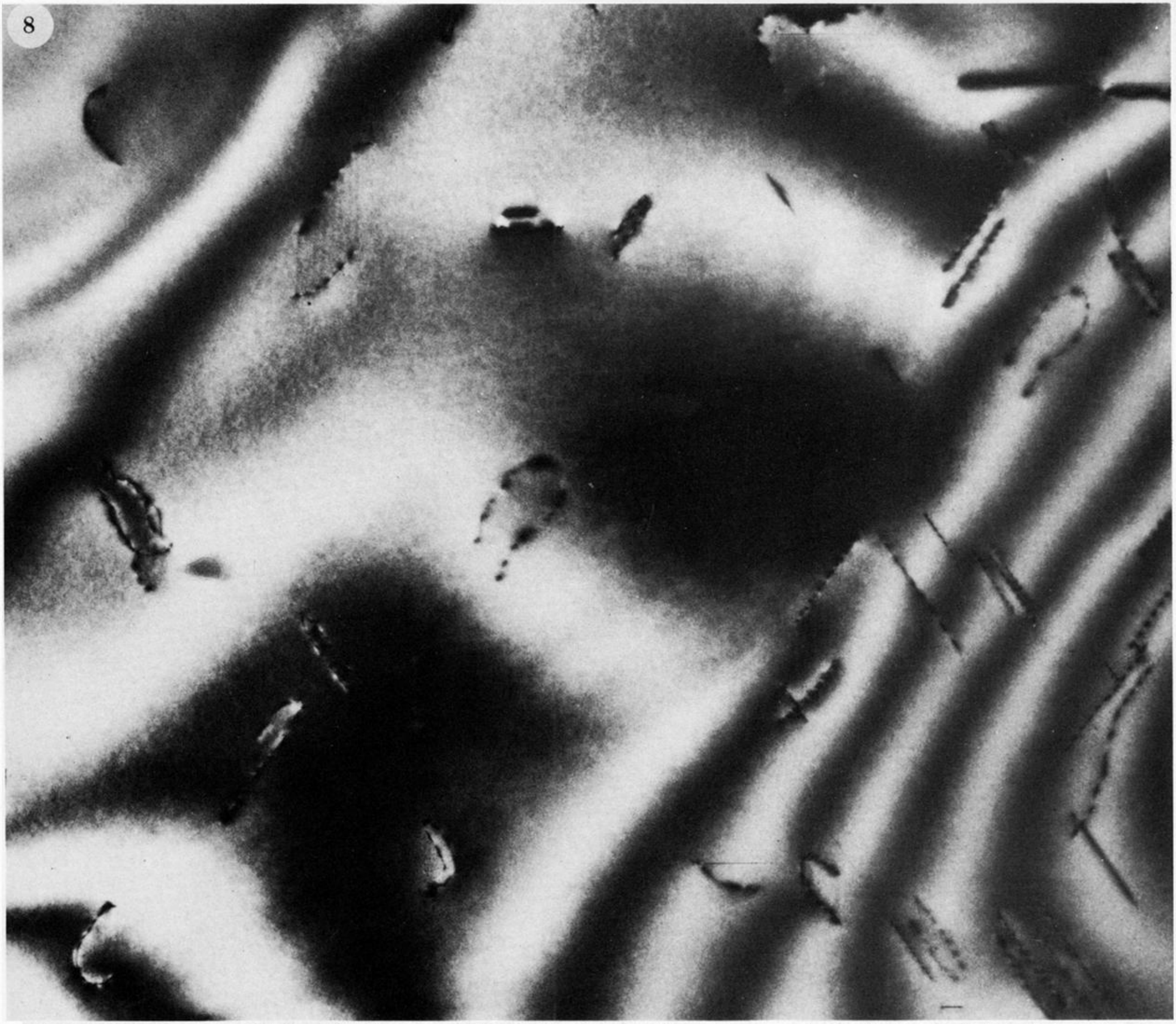

FIGURE 8. Panorama of dislocation loops and dipoles filled with voidite sheets, and some individual glide dislocations, in specimen DL4. Specimen thickness is between 0.20 and 0.24 μm. In this and all following micrographs the electron accelerating voltage is 200 kV. Field width 4 μm (6982, original magnification $\times 10^4$).

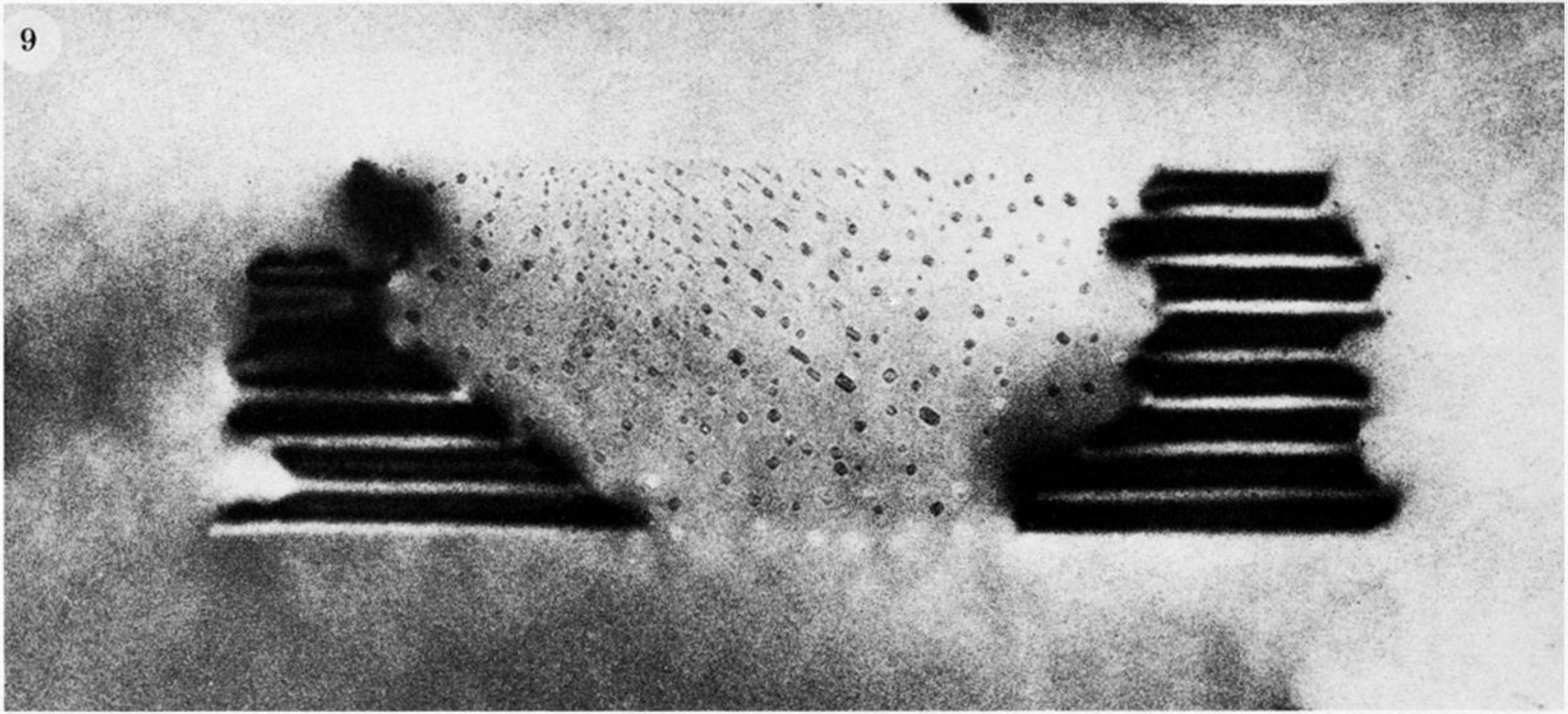

FIGURE 9. A partial platelet. Both left- and right-hand platelet areas have lobed peripheries; the right-hand boundary between voidite sheet and platelet is also lobed. A few fringing voidites can be seen outside the right-hand periphery of the platelet area on the right, and some voidites can be detected lying on this platelet area. Overall width of the partial platelet image is 0.75 μm. Specimen thickness is 0.22 μm. Here, and also in figures 10–14, the direction [001] is horizontal. The field width is 1 μm, and is also this value in figures 10–15 (7534, original magnification $\times 4 \times 10^4$).

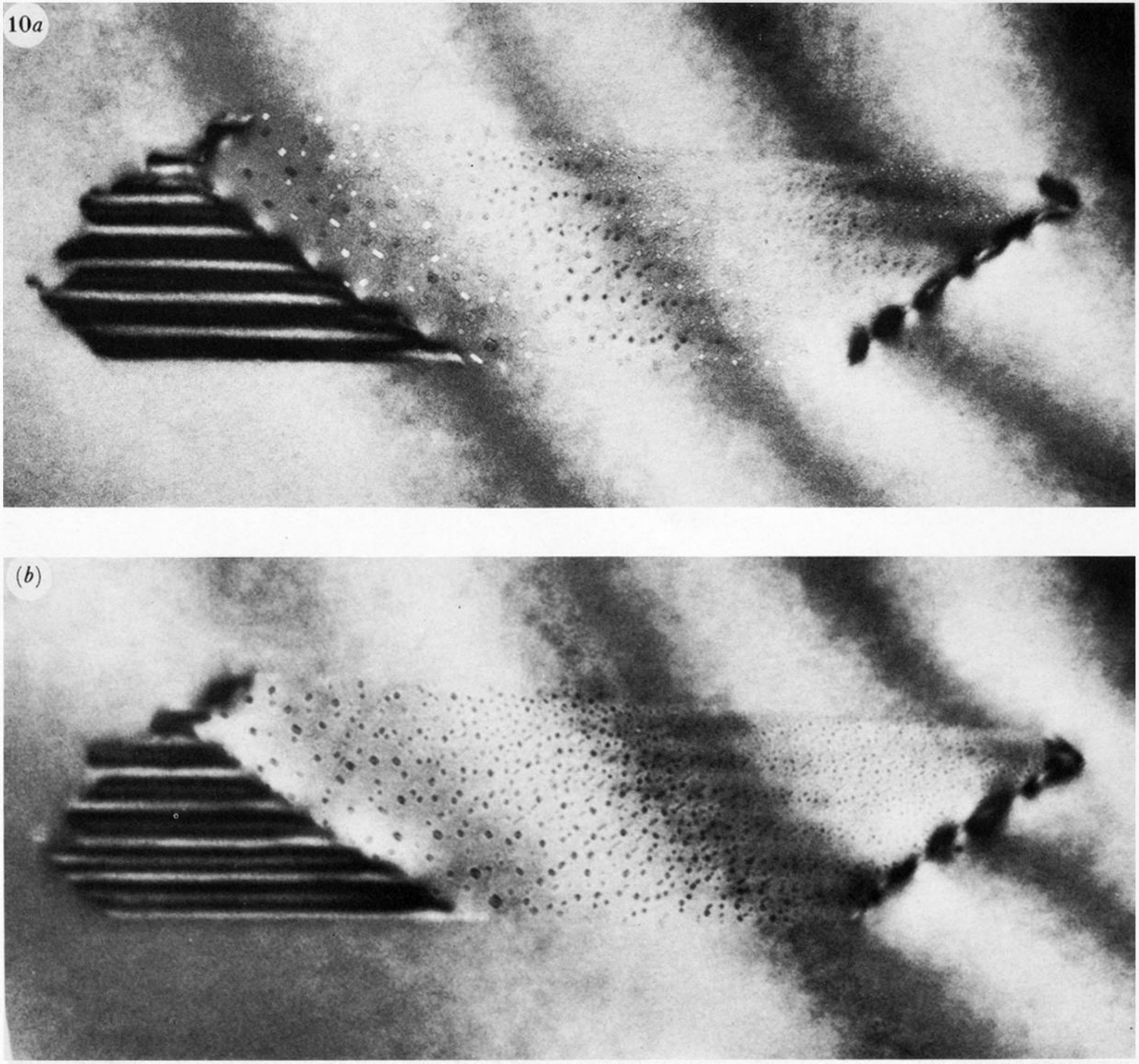

FIGURE 10. Partial platelet; overall platelet width in image is 0.9 μm, specimen thickness is 0.17–0.20 μm. (*a*) Near-optimum focus, showing depth-dependent cycle of voidite image contrast (7531, original magnification $\times 4 \times 10^4$); (*b*) overfocused image (7530).

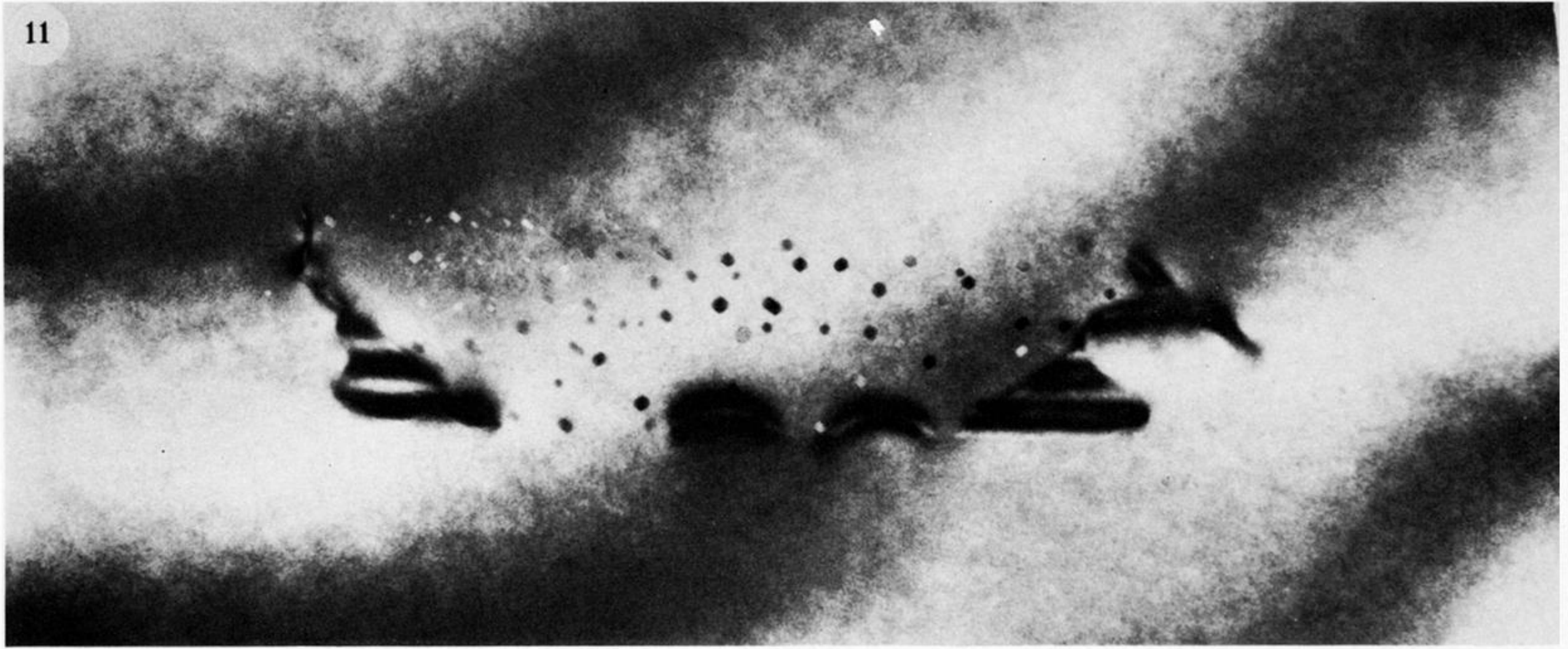

FIGURE 11. Annular partial platelet with lobate periphery. Overall platelet width in image is 0.6 μm, specimen thickness is 0.12–0.14 μm (7525, original magnification $\times 5 \times 10^4$).

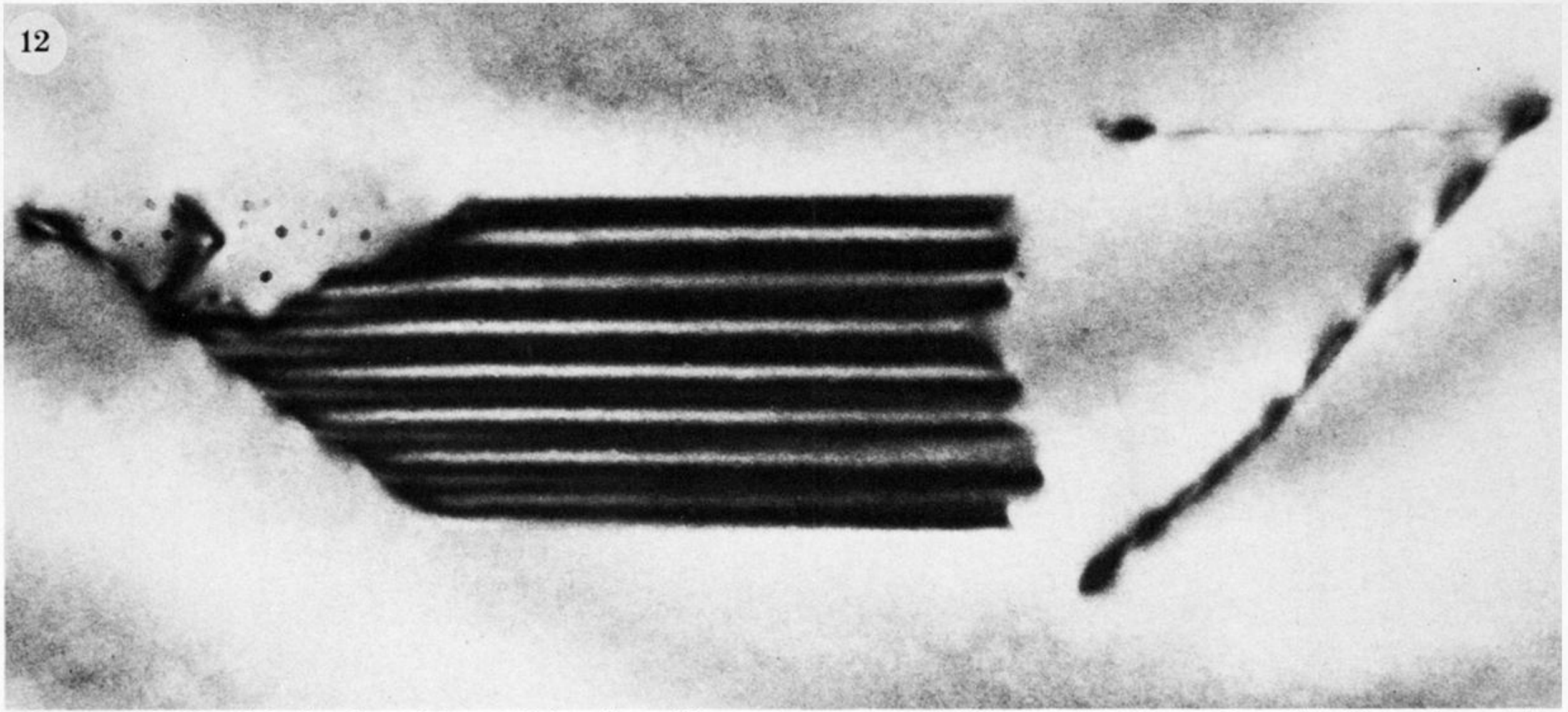

FIGURE 12. Partial platelet with small fraction of image area occupied by voidite sheet. Overall width of partial platelet image is 0.65 μm, specimen thickness is 0.2 μm. Dislocations on right of field are not associated with the partial platelet (7529, original magnification $\times 4 \times 10^4$).

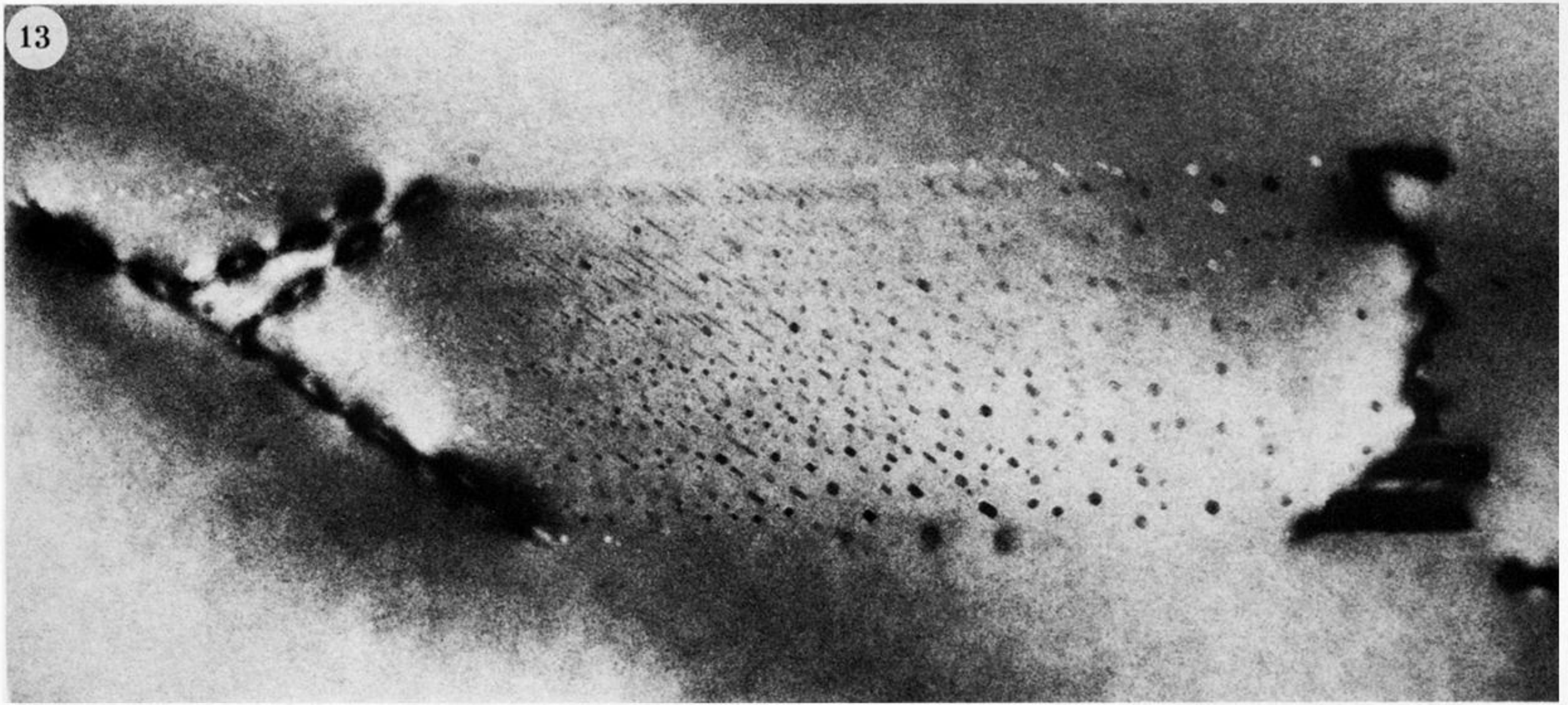

FIGURE 13. Partial platelet with high ratio of voidite sheet area to platelet area in the image. Highly elongated voidites appear in upper part of image of voidite sheet. Width of partial platelet image is 0.9 μm, specimen thickness is 0.23–0.25 μm (7532, original magnification $\times 4 \times 10^4$).

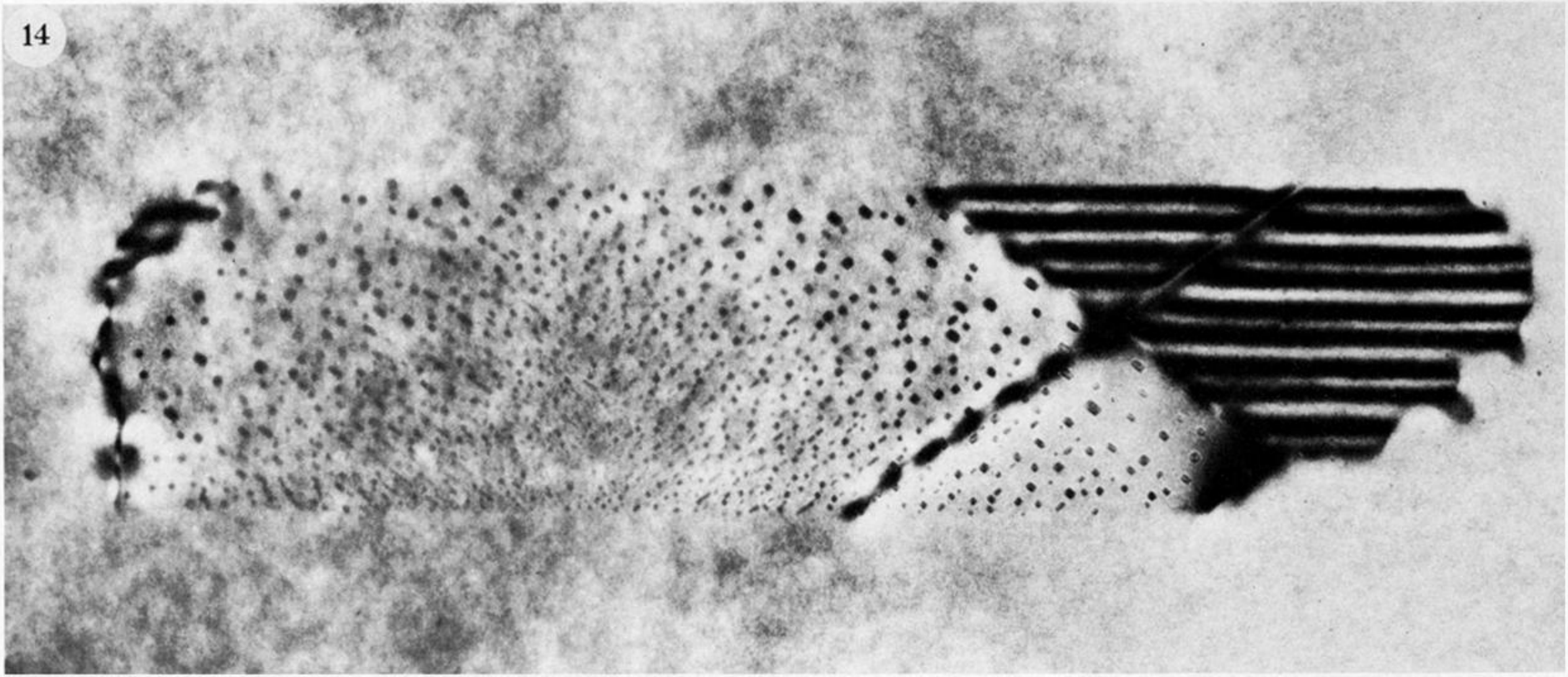

FIGURE 14. Partial platelet with a very narrow band of platelet contrast on left of voidite sheet. A single dislocation lies across voidite sheet and platelet areas on the right. Periphery of platelet is lobate, with, on the right, fringing voidites and voidites on the platelet. Overall width 0.9 μm, specimen thickness 0.2 μm (S7011, original magnification $\times 5 \times 10^4$).

15*a*

(*b*)

FIGURE 15. Partial platelet with dislocation dipole lying in, or very close to, platelet. Lobate periphery, fringing voidites and voidites on the platelet are noteworthy. Maximum dimension of platelet image is 0.9 μm, specimen thickness is 0.18 μm. (*a*) Near-optimum focus (Q7005, original magnification $\times 4 \times 10^4$); (*b*) underfocused to bring out contrast of voidites on the platelet area (they can be seen as white dots (Q7008)).

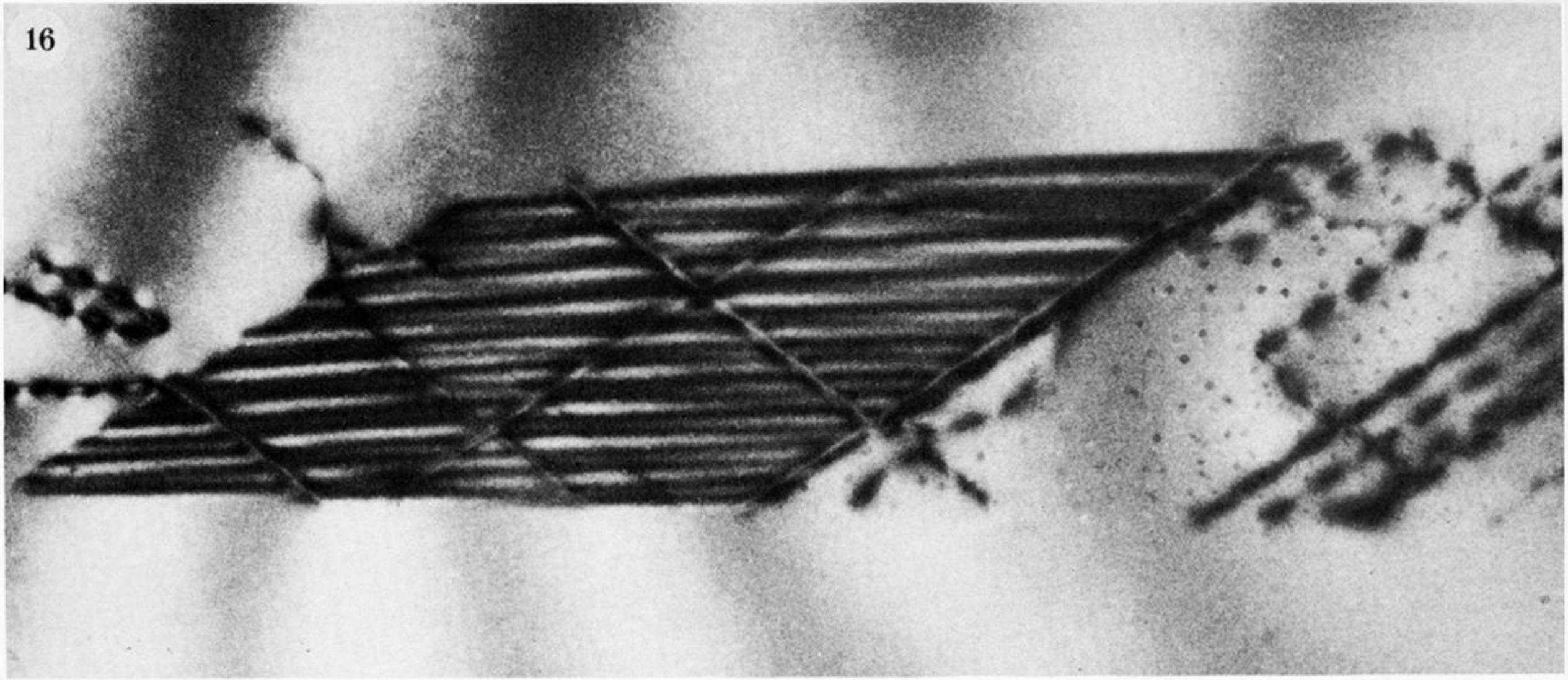

FIGURE 16. Major part of image of a large partial platelet whose total intersected length parallel to [001] (i.e. in the horizontal direction) is 1.7 μm. Glide dislocations lie in plane of platelet and voidite sheet. The specimen thickness is 0.24 μm on the left, rising to 0.33 μm at the right-hand edge of the partial platelet, beyond the limits of the field printed. Voidites on the platelet are detectable. Field width $1\frac{1}{3}$ μm (7533, original magnification $\times 3 \times 10^4$).

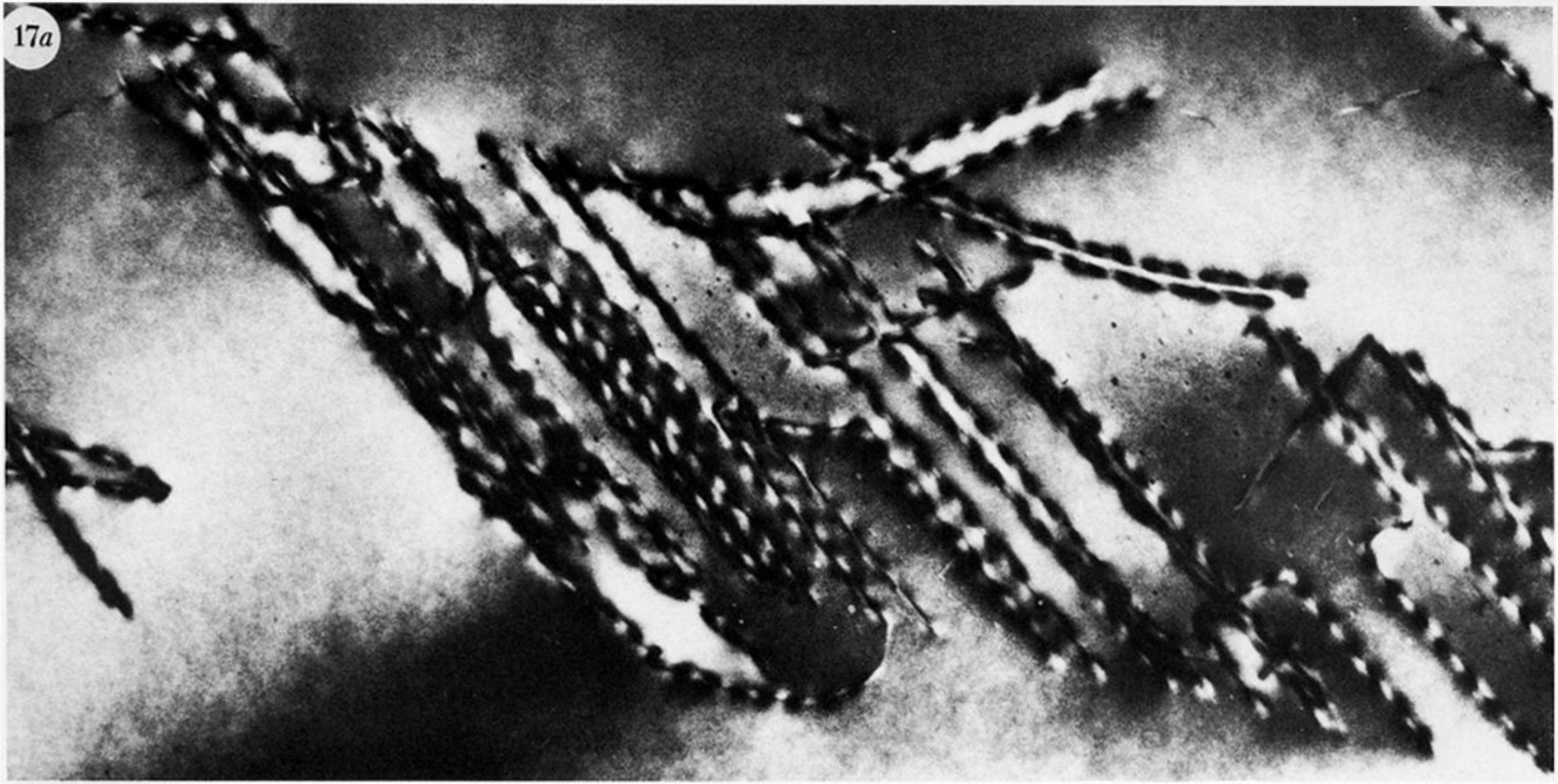

FIGURE 17*a*. Voidite sheet with many dislocations in and near the sheet. Direction [001] rotated 13° clockwise from horizontal. Specimen thickness is 0.32 μm. Field width is $1\frac{1}{3}$ μm (K6972, original magnification $\times 4 \times 10^4$).

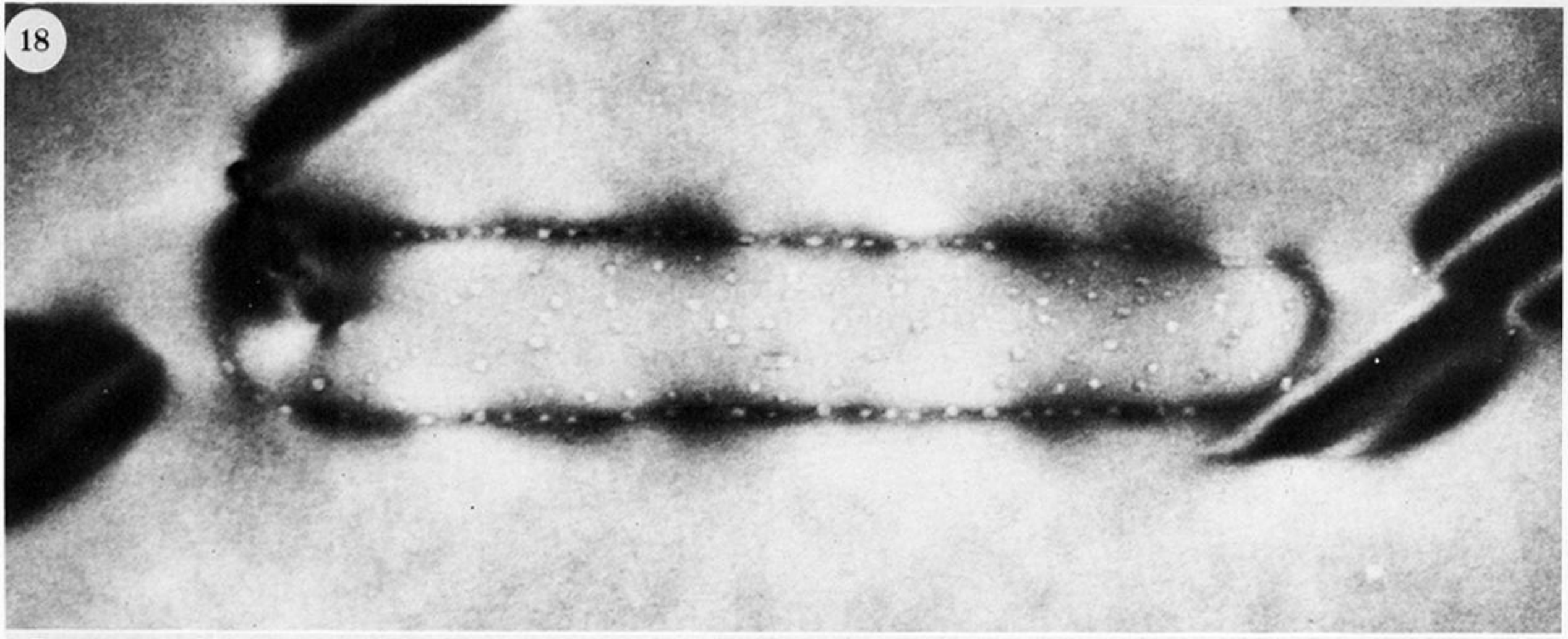

FIGURE 18. Voidite-containing dislocation loop completely within the specimen. Direction [001] rotated 35° anticlockwise from horizontal. Field width 0.5 μm, the actual loop length is 0.4 μm and its width is variable between 50 and 60 nm. Defocus chosen to show up voidites strung along the dislocation (4728, original magnification $\times 10^5$).

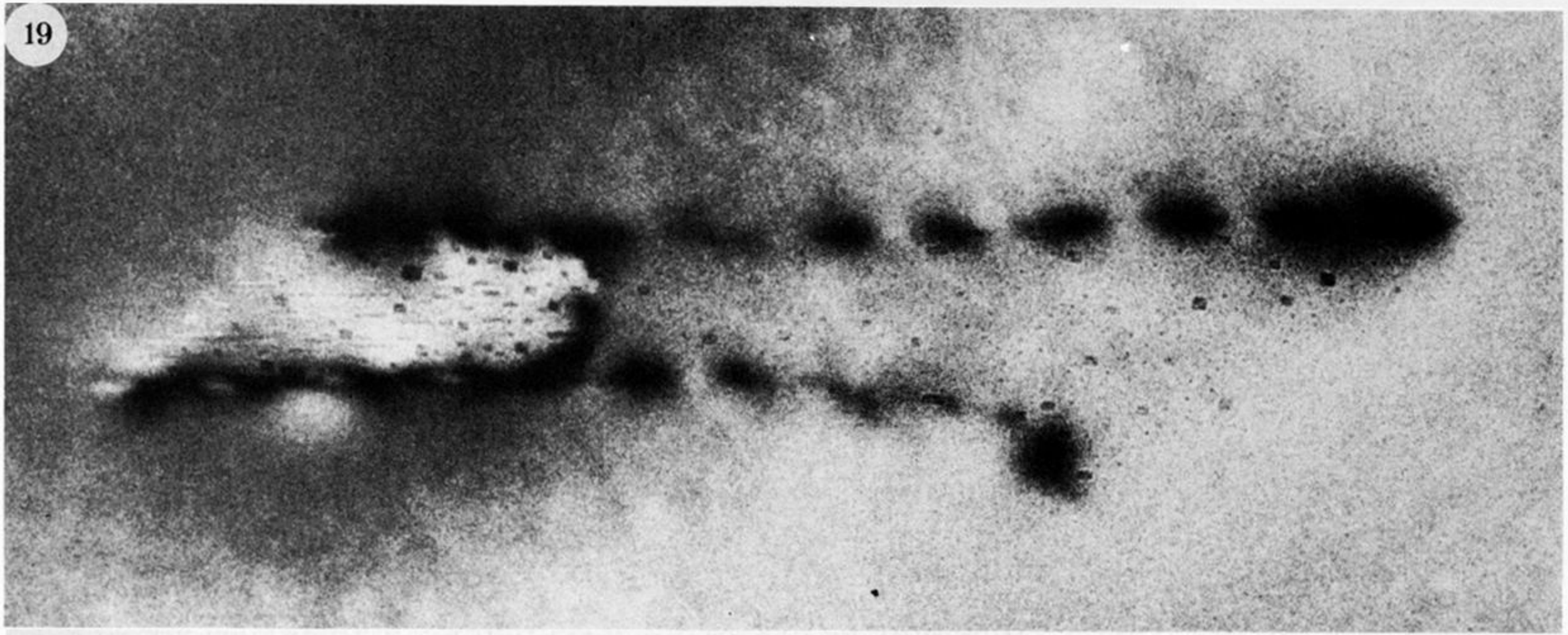

FIGURE 19. An H-feature comprising a voidite-containing pair of dislocations intersecting both upper and lower specimen surfaces with a bridging dislocation within the specimen. Orientation same as in figure 18. Field width is $\frac{2}{3}$ μm. Observe highly elongated voidites on left of the bridge. On the right there is a 'bimodal' voidite size distribution: some larger voidites with diameters of about 5 nm dispersed in a sea of small, weakly visible voidites having diameters of about 0.5 nm (R7010, original magnification $\times 3 \times 10^4$).

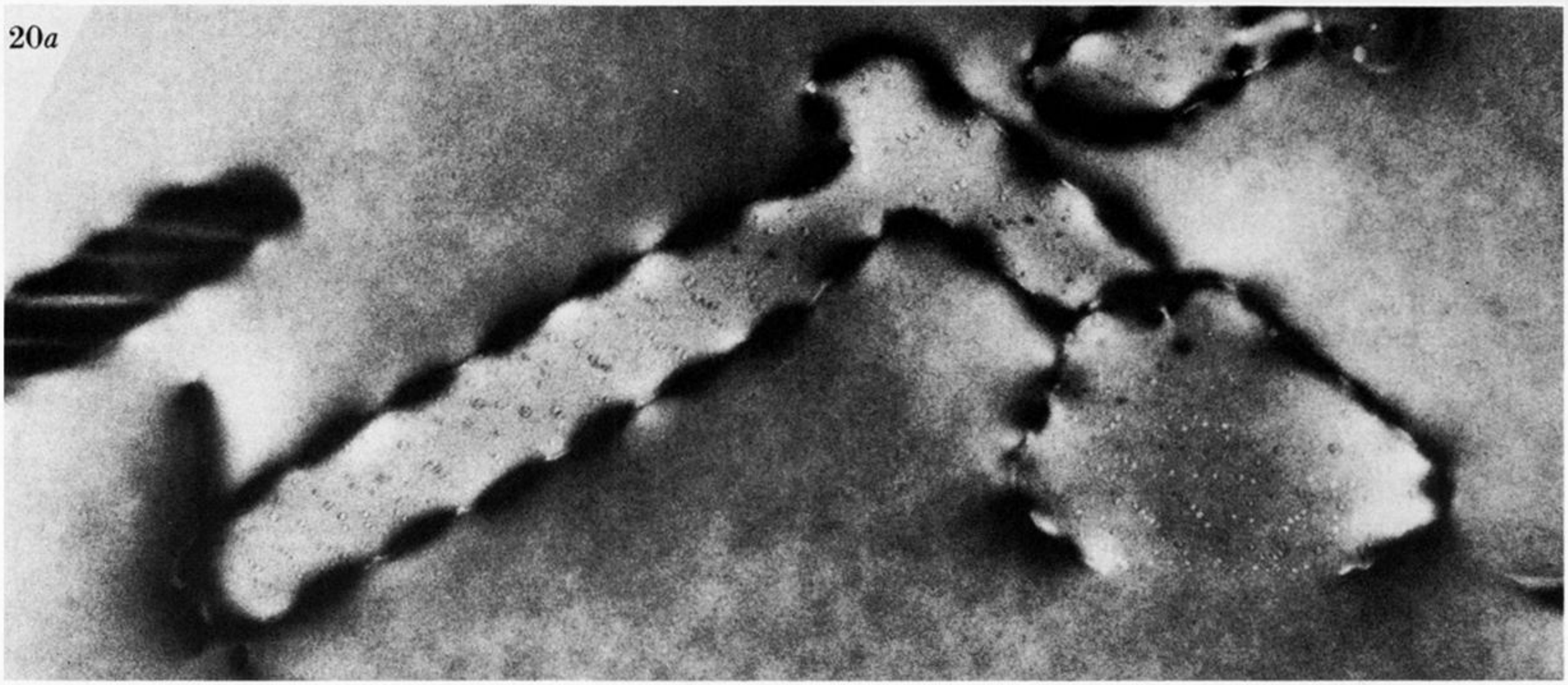

FIGURE 20. Voidite-containing dislocation loops. Direction [001] is horizontal, field width is 0.8 μm. Comparison of (*a*) bright-field (4706, original magnification $\times 6 \times 10^4$), and (*b*) dark-field image, 111-type reflection (4707).

FIGURE 21. Group of voidite-containing dislocation loops with some platelets. Direction [001] rotated 52° clockwise from horizontal. Field width is 0.5 μm (4723, original magnification $\times 1.5 \times 10^5$).

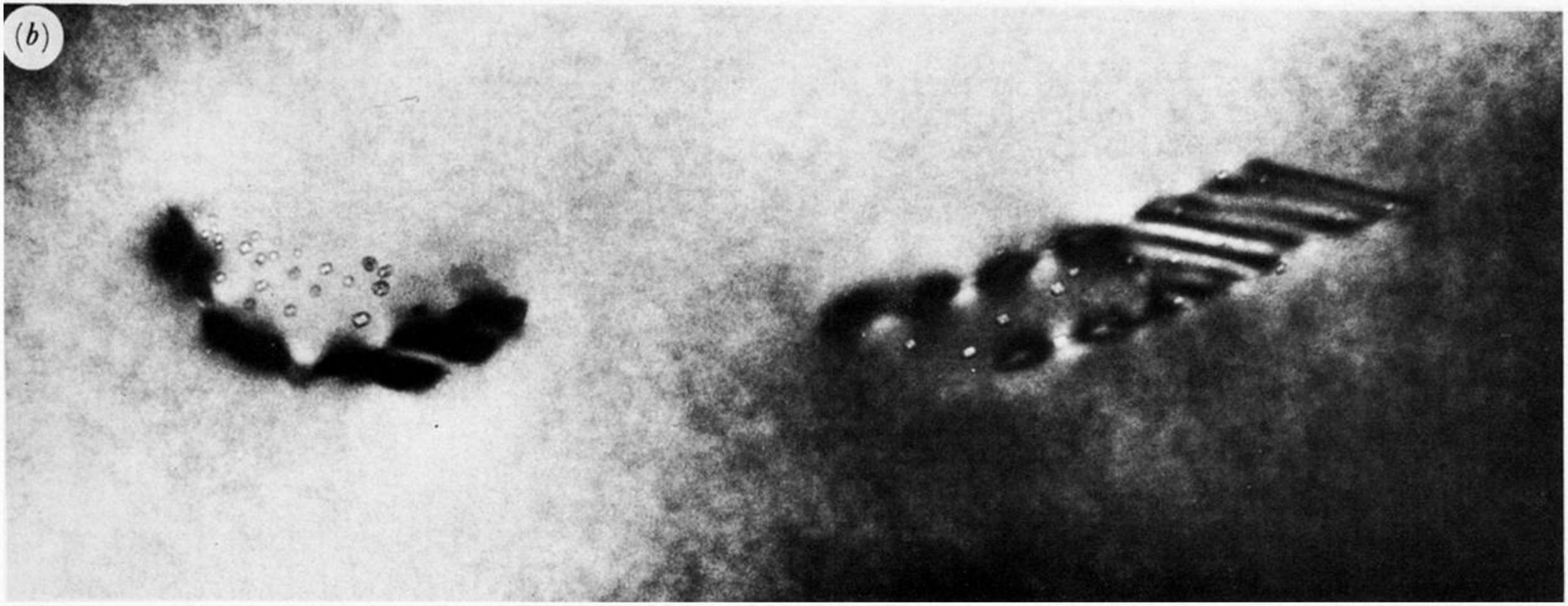

FIGURE 22. A pair of partial platelets; voidites lie on platelet area of right-hand partial platelet. Direction [001] rotated 10° clock-wise from horizontal. Field width is 1 μm, specimen thickness is 0.15 μm. (*a*) Near focus (E6952, original magnification $\times 5 \times 10^4$); (*b*) underfocused (E6957).

FIGURE 23. Partial platelet (left) with voidites on the platelet area, and a dislocation loop segment (upper right) containing many small voidites with diameters $< 1\ \mu m$. Direction [001] rotated 5° anticlockwise from horizontal. Field width is 1 μm and specimen thickness is 0.25 μm (G6949, original magnification $\times 4 \times 10^4$).

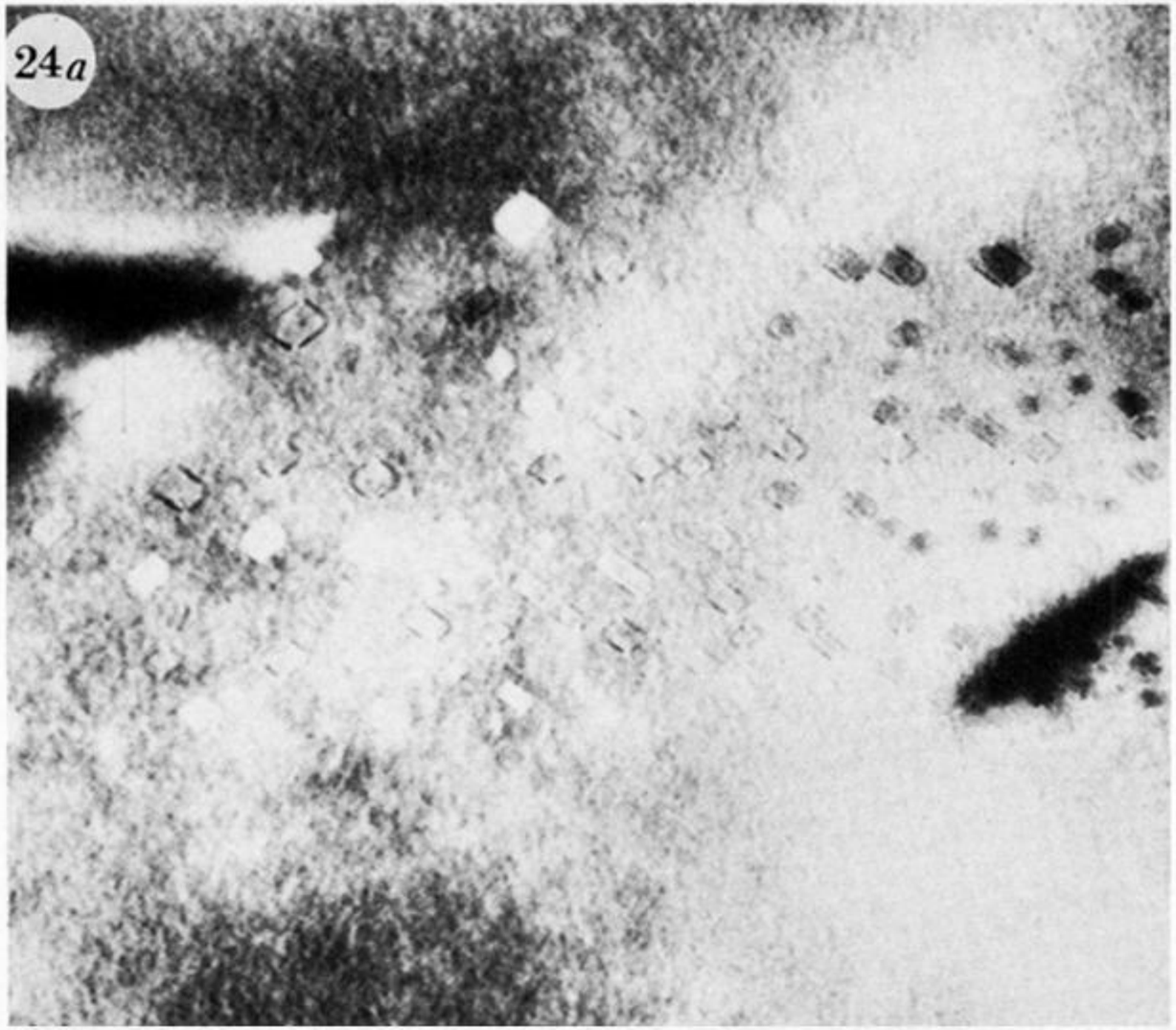

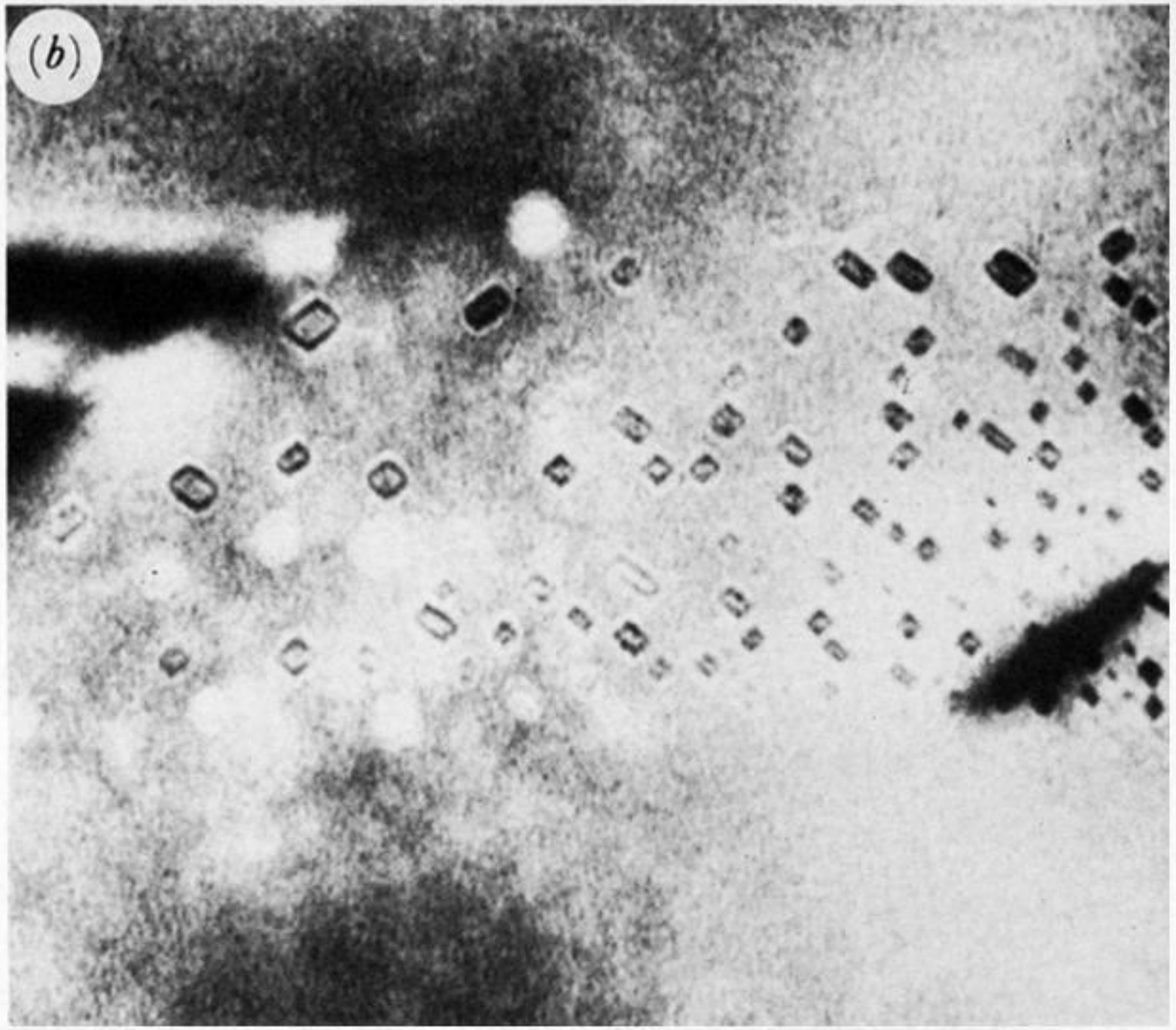

FIGURE 24. Voidite facet contrast in focused images of voidites. Direction [001] is horizontal, field width is 200 nm, specimen thickness is 80 nm. (*a*) Near focus, some voidites show only facet contrast (N6985, original magnification $\times 8 \times 10^4$); (*b*) overfocused relative to (*a*) (N6984).

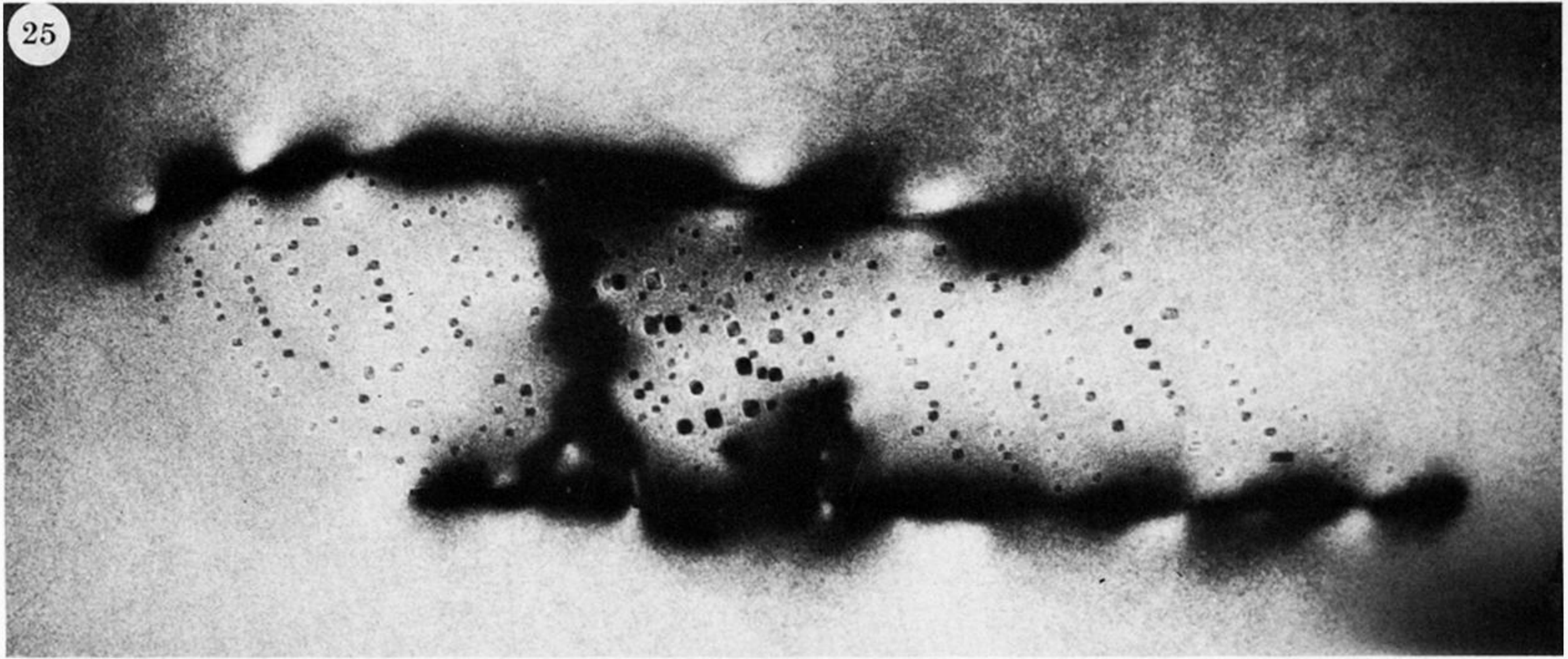

FIGURE 25. An H-feature exhibiting voidite chains. Direction [001] rotated about 40° clockwise from horizontal, field width 0.5 μm, specimen thickness 0.2 μm (4770, original magnification $\times 1.5 \times 10^5$).

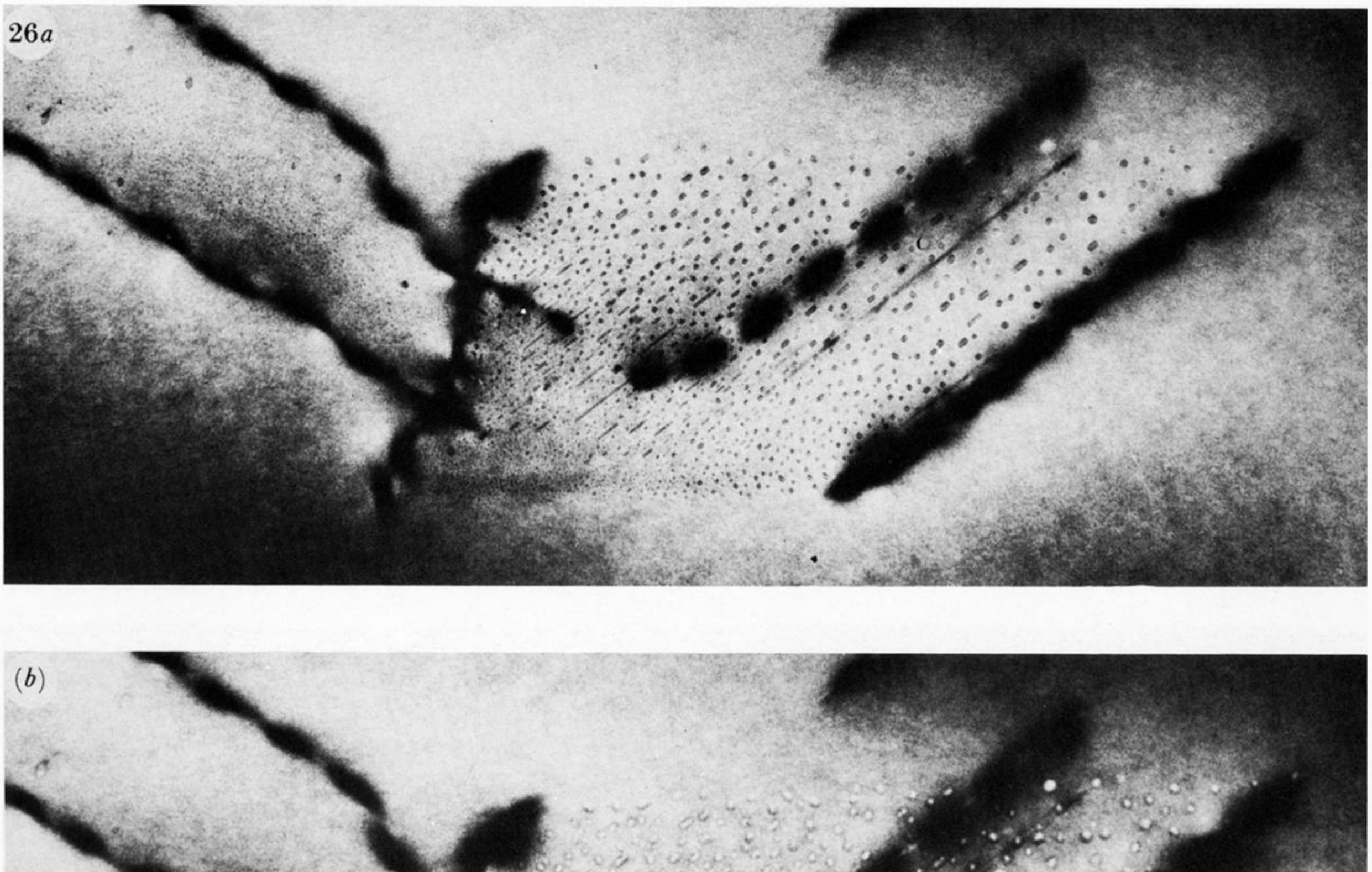

FIGURE 26. Voidite sheets lying between dislocations. The sheet in the field centre contains highly elongated voidites, linear features possibly exhibiting strain contrast, and evidence of residual fault-fringe contrast at its lower margin. The sheet in the upper left of the field contains many voidites with diameters below 1 nm. Direction [001] is horizontal. Field width is 1 μm, specimen thickness is 0.25 μm. The sequence (*a*), (*b*), (*c*) proceeds from near-optimum focus to increasing underfocus ((*a*), **I6966**; (*b*), **I6967**; (*c*), **I6968**, original magnification $\times 4 \times 10^4$).

FIGURE 27. Pair of voidite sheets. Evidence of residual fault surface contrast appears along the outcrop of the right-hand voidite sheet. Direction [001] is horizontal, field width is 0.9 μm (J6971, original magnification $\times 6 \times 10^4$).

FIGURE 28. Dislocation loops containing well-resolved voidites together with seas of small voidites of diameters < 1 μm. Some voidites appear outside loops. The loop in the lower central part of the field is not confined to a cube plane. Direction [001] is vertical, field width is $1\frac{1}{3}$ μm, specimen thickness about 0.19 μm (H6960, original magnification $\times 4 \times 10^4$).

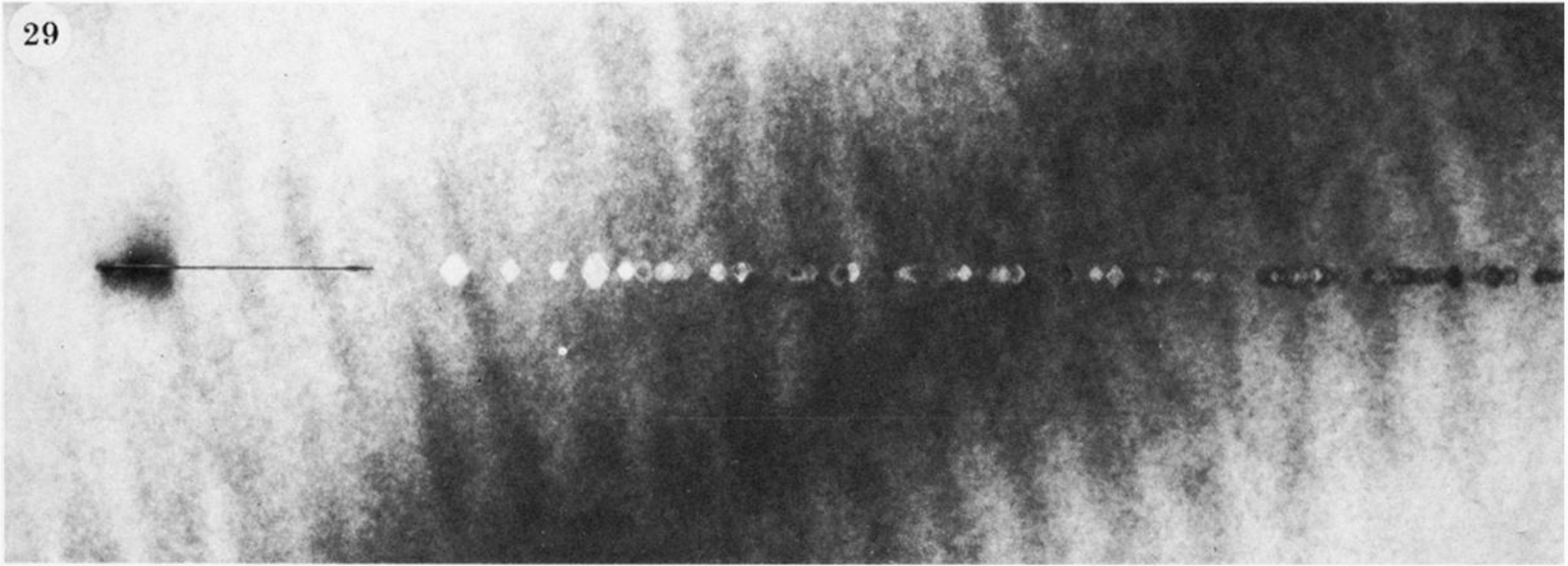

FIGURE 29. Edge-on view of partial platelet parallel to (001): platelet contrast on left, voidite sheet in centre and right of field, with largest voidites near platelet boundary. Specimen DL4/B. Direction [001] is vertical in this and the following figures. Field width 0.4 μm (12044, original magnification $\times 1.5 \times 10^5$).

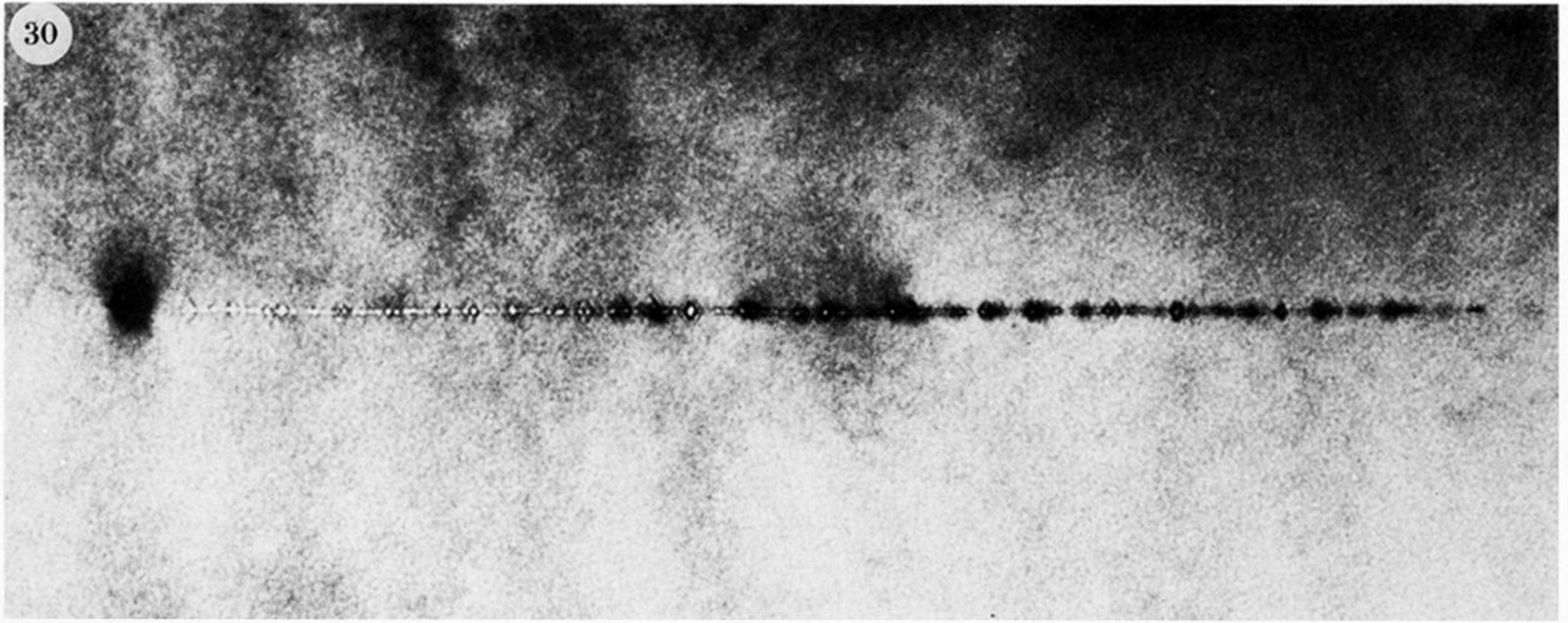

FIGURE 30. Edge-on view of voidite sheet parallel to (001), terminated on left by a strong dislocation image. Many voidite diameters are below 1 nm in this projection. Specimen DL4/B. Field width 0.2 μm (11482, original magnification $\times 2 \times 10^5$).

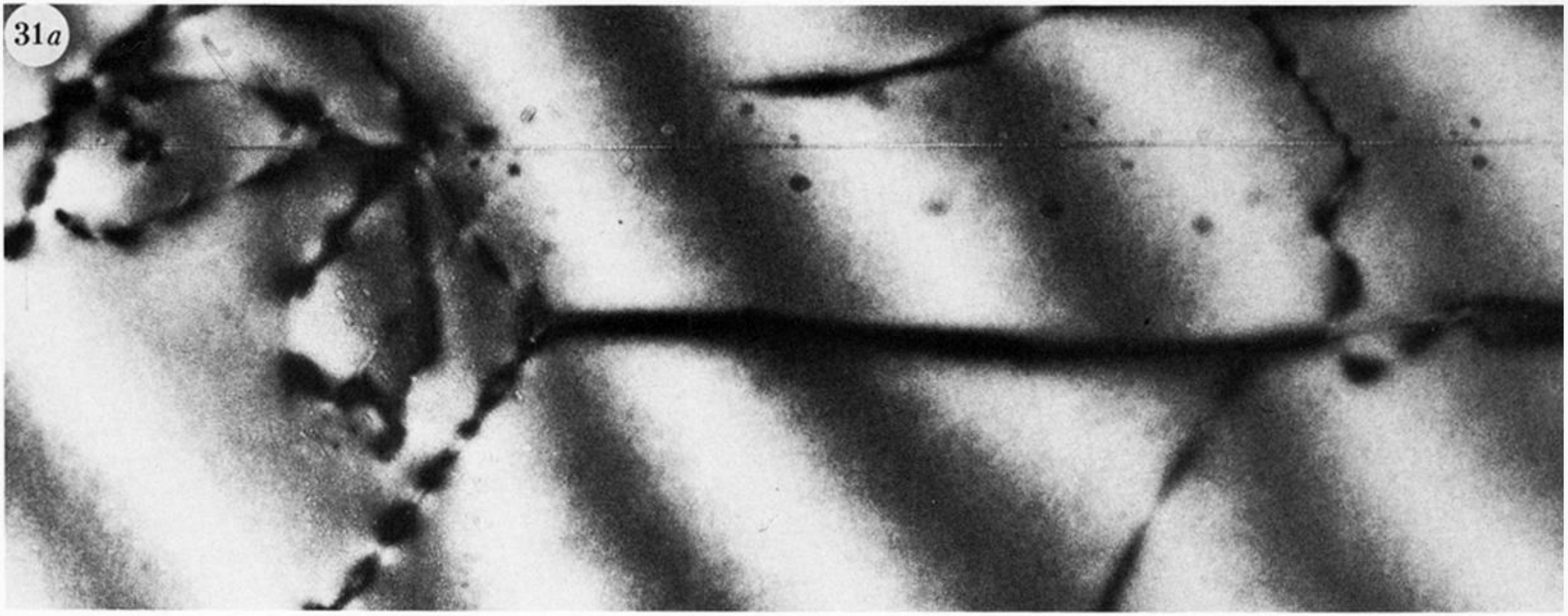

FIGURE 31. Field including the middle segment of a voidite sheet parallel to (001) whose total image length parallel to $[\bar{1}10]$ is greater than 1.7 μm. Dislocations and stray voidites also present. (*a*) Field width 1 μm (7526, original magnification $\times 4 \times 10^4$); (*b*) enlargement of top left of (*a*) to show highly elongated voidites apparently attached to dislocations; field width 0.4 μm.

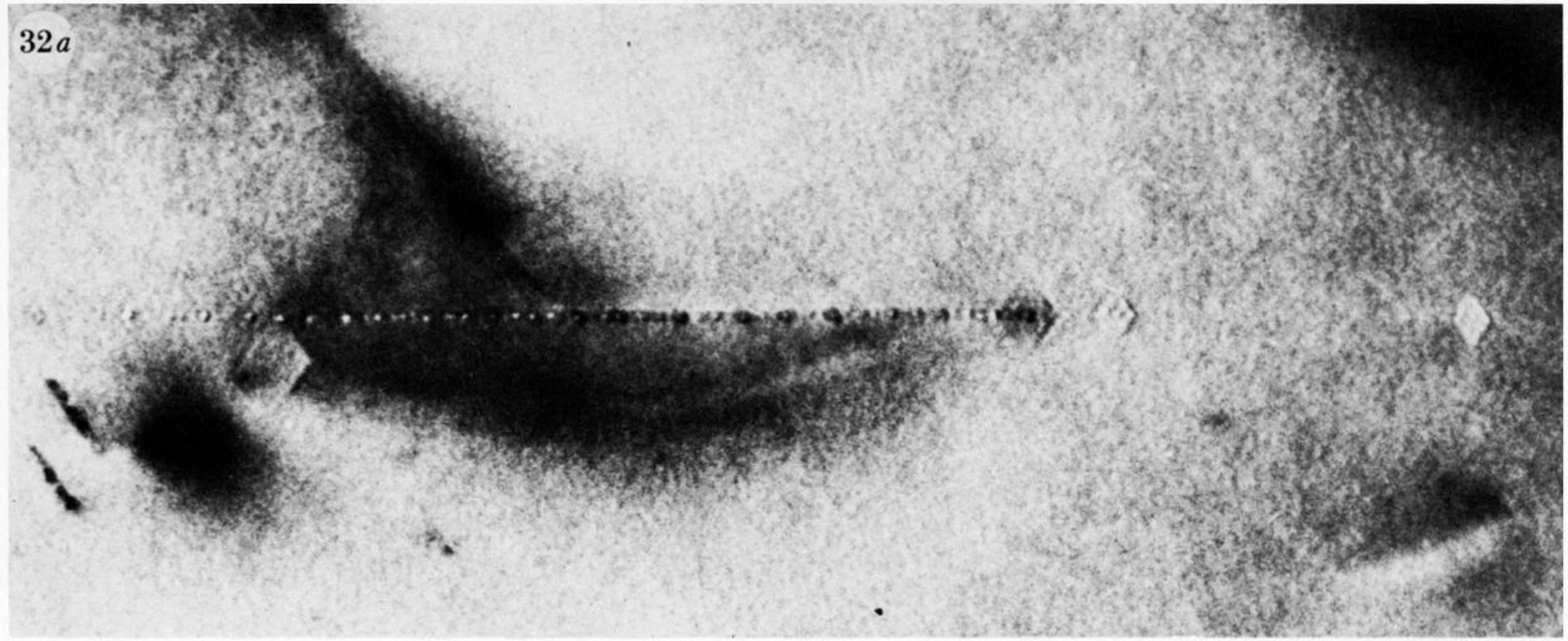

FIGURE 32. Voidite sheet parallel to (001) showing a large range in size and population density of voidites. Field width is 0.2 μm. Total length of voidite sheet image is 0.4 μm. (*a*) Focused to bring out contrast from a large voidite not centred on the sheet, at (0.17, 0.43) (D6947, original magnification $\times 8 \times 10^4$). (*b*) Focused for strong contrast from centre and left-hand segments of voidite sheet in the field (D6949, original magnification $\times 1 \times 10^5$).

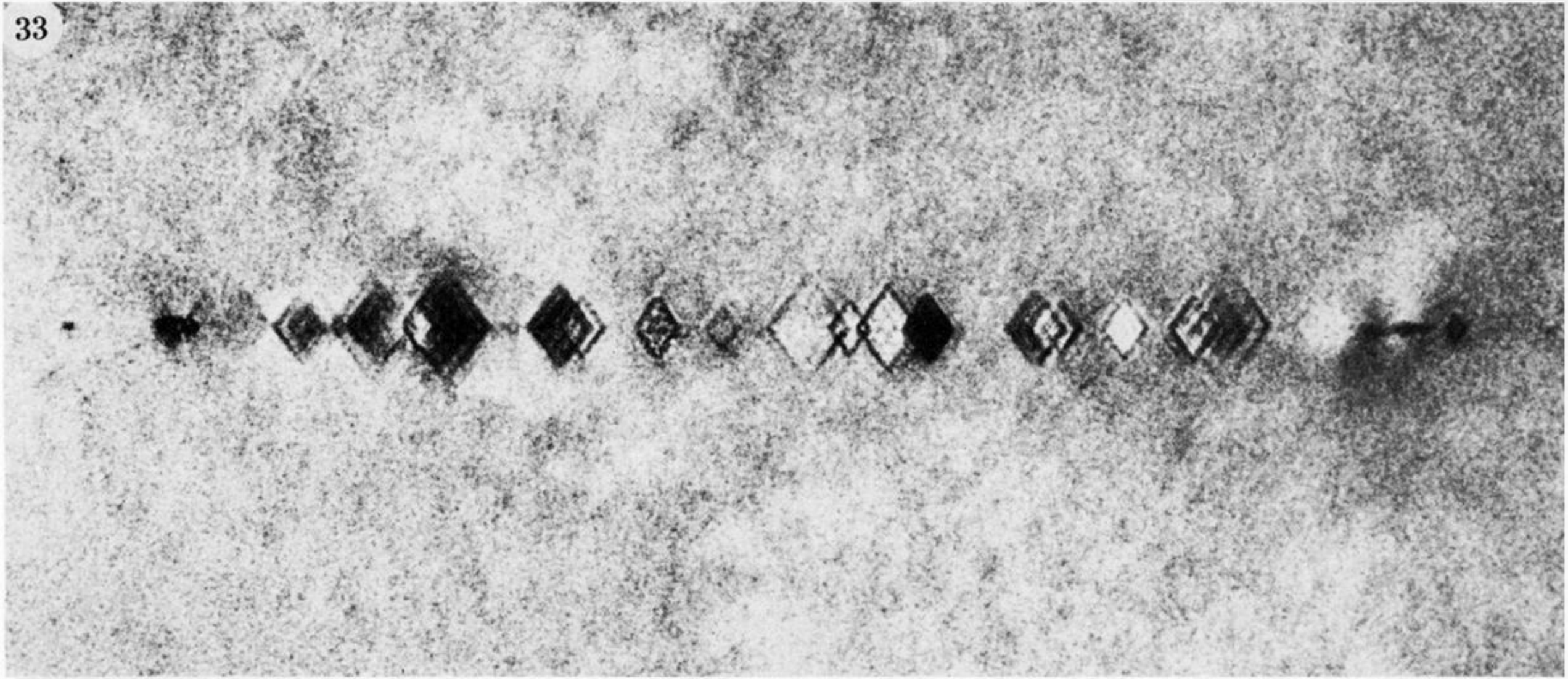

FIGURE 33. Voidite sheet parallel to (001) probably contained between a dislocation dipole elongated along [110]. Field width is 0.1 μm.